Electroweak Corrections to Three-Jet Production at Electron–Positron Colliders

Dissertation

zur
Erlangung der naturwissenschaftlichen Doktorwürde
(Dr. sc. nat.)
vorgelegt der
Mathematisch-naturwissenschaftlichen Fakultät
der
Universität Zürich
von

Christian Kurz

aus
Deutschland

Promotionskomitee
Prof. Dr. Thomas Gehrmann
PD Dr. Ansgar Denner
Prof. Dr. Daniel Wyler
Prof. Dr. Günther Dissertori

Zürich, 2009

Zusammenfassung

Viele QCD Präzisionsstudien an Elektron–Positron–Beschleunigern beruhen auf Messungen des Wirkungsquerschnittes der Produktion von drei Jets und verwandten Observablen, die von der spezifischen Geometrie eines Ereignisses abhängen (Event-Shape-Observable). Die Abweichung von einer Zwei-Jet-Konfiguration ist proportional zur starken Kopplungskonstanten α_s, so dass man durch den Vergleich der gemessenen mit der theoretisch vorhergesagten Produktionsrate von drei Jets α_s bestimmen kann.

Erst kürzlich sind die Korrekturen zu diesen Observablen in zweiter Ordnung QCD-Störungstheorie veröffentlicht worden. Da auf diesem Niveau der theoretischen Unsicherheit auch elektroschwache Effekte eine Rolle spielen, berechnen wir die elektroschwachen Korrekturen zur Produktion von drei Jets und verwandten Event-Shape-Observablen in der Ordnung $\alpha^3\alpha_s$. Wir benutzen das Komplexe-Masse-Schema auf Ein-Schleifen-Niveau und berücksichtigen Effekte, die durch Korrekturen höherer Ordnung im Eingangszustand entstehen, indem wir geeignete Strukturfunktionen verwenden.

Wir legen besonderen Wert auf die korrekte Behandlung der experimentellen Kriterien zur Photonisolierung, die einen Schnitt auf Ereignisse, in denen Photonen mehr als einen bestimmten Anteil an der Jetenergie tragen, beinhalten. Deshalb beziehen wir die Fragmentationsfunktion des Photons in unsere Rechnung mit ein, um so sicher zu stellen, dass alle von uns betrachteten Observablen infrarot sicher sind.

Die experimentell gemessenen Event-Shape-Observablen und Jet-Raten sind auf den totalen hadronischen Wirkungsquerschnitt σ_{had} normiert. Deshalb berechnen wir auch die Ein-Schleifen elektroschwachen Korrekturen zu σ_{had} und benutzen dabei die gleichen Kriterien zur Ereignisauswahl wie in der Berechnung der Jet-Raten und Event-Shape-Observablen.

Wir finden Korrekturen zu den Jet-Raten und Event-Shape-Observablen für Energien zwischen M_{Z} und 500 GeV auf dem Niveau von einem Prozent. Sie sind dominiert von Effekten, die durch Photonabstrahlung im Eingangszustand hervorgerufen werden, während die rein elektroschwachen Korrekturen sich im Bereich von einem Promille befinden. Die Form der differentiellen Verteilungen hängt sehr stark von den Parametern der Ereignisauswahl ab. Deshalb ist es unumgänglich in der perturbativen Rechnung und den experimentellen Analysen dieselben Kriterien der Ereignisauswahl zu benutzen.

Abstract

Many precision QCD studies at electron–positron colliders rely on the measurements of the three-jet production cross section and related event-shape observables. The deviation from simple two-jet configurations is proportional to the strong coupling constant α_s so that by comparing the measured three-jet rate and related event shapes with the theoretical predictions one can determine α_s.

Recently, results for the next-to-next-to-leading-order QCD corrections to these observables have become available. Since at this level of precision electroweak effects also become important, we compute the electroweak $\mathcal{O}(\alpha^3\alpha_s)$ corrections to three-jet production and related event-shape observables. We employ the complex-mass scheme at one-loop and consistently incorporate higher-order initial-state-radiation effects using a structure-function approach.

We put special emphasis on properly accounting for the experimental photon-isolation criteria which include a cut on events where photons carry more than a certain percentage of the jet energy. Therefore we have to incorporate the photon fragmentation function, to ensure that all considered observables are infrared safe.

Experimentally measured event-shape distributions and jet rates are normalised to the total hadronic cross section σ_{had}. Hence, we also compute the next-to-leading-order electroweak corrections to σ_{had} using the same event-selection cuts as in the calculation of event-shape distributions and jet rates.

Corrections to the three-jet rate and to normalised event-shape distributions turn out to be at the few-per-cent level for energies between M_Z and 500 GeV. They are dominated by the initial-state-radiation contribution, while the purely weak contribution is typically at the per-mille level. The shape of the differential distributions strongly depends on the values of the parameters used in the event selection. It is therefore mandatory to use the same event-selection criteria in the perturbative calculation and in experimental analyses when comparing theoretical predictions to data.

Contents

Introduction

The Standard Model of particle physics (SM) provides a very successful description of the nature of the fundamental interactions among elementary particles. Mathematically it can be represented by a local $\mathrm{SU(3)_C} \otimes \mathrm{SU(2)_L} \otimes \mathrm{U(1)}_Y$ gauge theory.

Quantum Chromodynamics (QCD) is a dynamical description of the strong interaction, which for example is responsible for the binding of quarks and gluons inside the proton and neutron. Its theoretical foundation is described in Refs. [1–4], using a local $\mathrm{SU(3)_C}$ gauge theory. The fundamental building blocks are spin-1/2 fermions called quarks, and spin-1 gauge bosons called gluons. First experimental evidence for the quarks has been found in deep-inelastic scattering experiments at SLAC, and the gluons have been identified in three-jet events at PETRA.

In the electroweak part of the SM the electromagnetic and weak interactions are unified in the framework of an $\mathrm{SU(2)_L} \otimes \mathrm{U(1)}_Y$ gauge theory. The matter fields, i.e. the quarks and leptons, are organised in families, where the left-handed fermions transform as doublets and the right-handed fermions as singlets under $\mathrm{SU(2)_L}$. The vector bosons $\mathrm{W}^{\pm}, \mathrm{Z}, \gamma$, which mediate the interactions, can be incorporated through the mechanism of minimal coupling to the matter fields [5–7]. It has been shown in [8–10] that gauge theories, where anomalies cancel among the matter fields, are renormalizable, leading to well-defined physical observables even at the quantum level.

Major triumphs of the SM were the discovery of the W and Z bosons at the SPS at CERN in 1983, the discovery of the top quark at the Tevatron at Fermilab in 1995, and the verification of the theory at the quantum level through experiments conducted at LEP during the past 20 years. Experimentally the masses of the Z and the W boson have been measured to be 91.2 GeV and 80.4 GeV respectively. From the pure gauge concept however, one expects massless vector bosons. The puzzle can be solved by employing the Higgs-Kibble mechanism [11–15]. One introduces a scalar $\mathrm{SU(2)_L}$ doublet field which couples via minimal coupling to the vector bosons. In this way one breaks the gauge symmetry spontaneously and generates the masses of the vector bosons in a gauge-invariant way, without destroying the unitarity or the renormalizability of the theory. The masses of the fermions are generated through Yukawa couplings to the Higgs field. The ground state of the theory is shifted away from the symmetric origin through the self-interaction of the Higgs field and chooses one of the infinitely

degenerate ground states after spontaneous symmetry breaking. The residual symmetry corresponds to the electromagnetic $U(1)_{EM}$, which is manifest in the masslessness of the photon. The original $SU(2)_L$ doublet has four degrees of freedom, three of which lead to the transverse polarisations of the massive gauge bosons. The fourth degree of freedom corresponds to a neutral scalar field, the Higgs boson, whose mass is a free parameter of the theory. The Higgs boson is the last particle in the SM which has not yet been experimentally observed. It has been intensively searched for in the past and its discovery is one of the main goals of the LHC.

Gravity, the fourth fundamental interaction, is described classically in the theory of General Relativity [16]. However, a formulation of gravity in a quantum theory is still an open question. In particle physics experiments up to present day energies of a few TeV, gravity can be neglected compared to the strength of the other three interactions.

The only free parameter of QCD is the strong coupling constant α_s. Therefore it is of utmost importance to determine this parameter as precisely as possible.

A very clean environment for precise measurements of α_s is provided by the LEP collider at centre-of-mass energies between 91 and 206 GeV. Many of those measurements are based on event-shape observables, which probe the structure of the hadronic final state. Only recently a theoretical prediction at next-to-next-to leading order (NNLO) QCD for event-shape observables has become available and has been used for a precise prediction of α_s.

In this thesis we calculate the next-to-leading order (NLO) electroweak corrections to jet rates and event-shape observables in e^+e^- annihilation, which could be of comparable size to the NNLO QCD corrections. We put special emphasis on the implementation of the experimental cuts used at LEP, where we have to incorporate the quark-to-photon fragmentation function to obtain infrared-safe observables.

In the first chapter of this work we give a brief overview of the theoretical foundations of QCD and discuss event-shape observables at e^+e^- colliders and their calculation using perturbation theory. In Chapter 2 we outline the strategy for the calculation of the NLO electroweak corrections, followed by a description of the implementation of these corrections into a Monte Carlo simulation in Chapter 3. Chapter 4 is devoted to the presentation of the numerical results for selected event-shape distributions. Analytical results for the tree-level and real radiation amplitudes can be found in Appendix A.

Chapter 1

Overview

In this chapter we give a brief theoretical overview of QCD, focusing on the properties of the strong coupling constant α_s. We also describe how e^+e^- colliders are used as a particularly clean experimental testing ground for QCD. Since we are interested in electroweak effects, the treatment of photons in the event selection is of particular importance. We consider this issue with the example of the event-selection procedure employed by the ALEPH collaboration at the LEP collider. Furthermore we review the concepts of jet algorithms and event-shape observables. For a more detailed account, see for example Refs. [17, 18] and references therein.

1.1 The theory of QCD

QCD can be described in the framework of a non-Abelian Yang–Mills theory, with SU(3) as the underlying symmetry group. The matter particles are called quarks and transform under the three-dimensional fundamental representation. The gauge bosons are called gluons and transform under the eight-dimensional adjoint representation. The masses of the quarks are denoted by m_q, whereas because of the gauge structure of the theory the gluons are massless. The corresponding Lagrangian density is given by (cf. Ref. [19])

$$\mathcal{L}_{\mathrm{QCD}} = -\frac{1}{4} G^A_{\mu\nu} G^{\mu\nu}_A + \sum_q \bar{q}_a \left(\mathrm{i}\gamma^\mu D_\mu - m_q\right)_{ab} q_b, \tag{1.1}$$

where Greek letters denote Lorentz indices, capital Roman letters indicate group indices corresponding to the adjoint representation, lower-case Roman letters characterise group indices corresponding to the fundamental representation, and we sum over repeated indices. The quark fields are denoted by q_a and the field strength tensor $G^A_{\mu\nu}$ is given by

$$G^A_{\mu\nu} = \partial_\mu G^A_\nu - \partial_\nu G^A_\mu - g_s f^{ABC} G^B_\mu G^C_\nu, \tag{1.2}$$

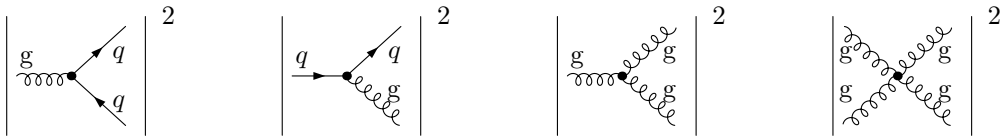

Figure 1.1: Particle splittings in QCD.

with G_μ^A being the gluon field, f^{ABC} the structure constants of SU(3), and g_s the coupling constant of QCD, which determines the strength of the interaction. One usually defines

$$\alpha_\mathrm{s} = \frac{g_\mathrm{s}^2}{4\pi}. \tag{1.3}$$

The last term of Eq. (1.2) leads to the self-interaction of gluons, which is due to the fact that gluons carry colour charge, in contrast to QED, where the photon is neutral. It is this term that gives rise to many interesting features of the strong interactions.

The covariant derivative can be written as

$$(D_\mu)_{ab} = \partial_\mu \delta_{ab} + \mathrm{i} g_\mathrm{s} (t^A G_\mu^A)_{ab}, \tag{1.4}$$

which depends on the coupling constant g_s and the generators t^A of the fundamental representation of $SU(3)$. In the following we neglect the quark masses and consider massless QCD only.

From Eq. (1.1) we can derive Feynman rules which enable us to perform perturbative calculations in QCD. If we look at the individual graphs, we can get a feeling for their relative strength. The first graph in Fig. 1.1 shows quark pair production, which occurs with relative strength $\alpha_\mathrm{s} T_\mathrm{F}\, n_\mathrm{f}$. The second graph represents gluon radiation off a quark, which occurs with relative strength $\alpha_\mathrm{s} C_\mathrm{F}$. In the third graph we can see the triple gluon vertex, whose relative strength is given by $\alpha_\mathrm{s} C_\mathrm{A}$. And finally the four gluon vertex in the fourth picture, which occurs with relative strength $\alpha_\mathrm{s}^2 C_\mathrm{A}^2$. The constants T_F, C_F, and C_A are related to the structure of the group under consideration. For SU(3) we find $T_\mathrm{F} = 1/2$, $C_\mathrm{F} = 4/3$, $C_\mathrm{A} = 3$, and n_f is given by the number of active quark flavors.

When calculating higher-order corrections to physical observables in a quantum field theory, one encounters divergencies which in principle would spoil the predictive power of the theory. However, in renormalizable theories these divergencies can be absorbed into the bare parameters of the Lagrangian which differ from the physical parameters. In Ref. [8] it has been shown that QCD is renormalizable. The renormalisation procedure introduces an arbitrary energy scale μ at which the renormalisation is performed, such that the parameters of the theory under consideration are μ-dependent. A physical observable R, however, must not depend on the scale μ, a condition that can be

expressed through

$$\mu^2 \frac{\mathrm{d}R}{\mathrm{d}\mu^2} = 0. \tag{1.5}$$

Using the dependence of the parameters on the scale μ, we can write

$$\begin{aligned} \mu^2 \frac{\mathrm{d}}{\mathrm{d}\mu^2} &= \mu^2 \frac{\partial}{\partial \mu^2} + \mu^2 \frac{\partial \alpha_\mathrm{s}}{\partial \mu^2} \frac{\partial}{\partial \alpha_\mathrm{s}} + \mu^2 \frac{\partial m}{\partial \mu^2} \frac{\partial}{\partial m} \\ &= \mu^2 \frac{\partial}{\partial \mu^2} + \beta\left(\mu^2\right) \frac{\partial}{\partial \alpha_\mathrm{s}} - \gamma_m\left(\mu^2\right) m \frac{\partial}{\partial m}, \end{aligned} \tag{1.6}$$

where m is the quark mass. The coefficients β and γ_m are the renormalisation group coefficients, usually called the β function and the anomalous mass dimension.

In the following we have a closer look at $\alpha_\mathrm{s}\left(\mu^2\right)$ and the β function. If we take the definition

$$\beta\left(\alpha_\mathrm{s}, \mu^2\right) = \mu^2 \frac{\partial \alpha_\mathrm{s}}{\partial \mu^2}, \tag{1.7}$$

and identify the renormalisation scale μ with the typical energy scale Q^2 of the considered process, we find

$$Q^2 \frac{\partial \alpha_\mathrm{s}}{\partial Q^2} = \beta\left(\alpha_\mathrm{s}, Q^2\right), \tag{1.8}$$

which shows that α_s changes its value, i.e. 'runs', with a change in the energy scale. The perturbative expansion of the β function is given by [19]

$$\beta\left(\alpha_\mathrm{s}, Q^2\right) = Q^2 \frac{\partial \alpha_\mathrm{s}}{\partial Q^2} = -\beta_0 \alpha_\mathrm{s}^2 - \beta_1 \alpha_\mathrm{s}^3 - \beta_2 \alpha_\mathrm{s}^4 + \mathcal{O}\left(\alpha_\mathrm{s}^5\right), \tag{1.9}$$

with

$$\begin{aligned} \beta_0 &= \frac{1}{12\pi}\left(33 - 2n_\mathrm{f}\right), \\ \beta_1 &= \frac{1}{24\pi^2}\left(153 - 19n_\mathrm{f}\right), \\ \beta_2 &= \frac{1}{\pi^3}\left(22.320 - 4.3689n_\mathrm{f} + 0.09404n_\mathrm{f}^2\right), \end{aligned} \tag{1.10}$$

where β_2 is given in the $\overline{\mathrm{MS}}$ scheme. One can integrate Eq. (1.8) to obtain

$$\alpha_\mathrm{s}\left(Q^2\right) = \frac{1}{\beta_0 L} - \frac{\beta_1 \ln L}{\beta_0^3 L^2} + \frac{1}{\beta_0^3 L^3}\left[\frac{\beta_1^2}{\beta_0^2}\left(\ln^2 L - \ln L - 1\right) + \frac{\beta_2}{\beta_0}\right] + \mathcal{O}\left(\frac{1}{L^4}\right), \tag{1.11}$$

where $L = \ln Q^2/\Lambda^2_{\overline{\mathrm{MS}}}$ and $\Lambda_{\overline{\mathrm{MS}}}$ is the constant of integration.

Considering the coefficient β_0, one can see that it is positive for $n_\mathrm{f} < 17$. Thus, the strong coupling constant decreases with increasing Q^2. It follows that quarks and gluons behave like weakly interacting particles at high energies and a perturbative expansion in α_s can be employed. This phenomenon is called asymptotic freedom. On the other hand, Eq. (1.11) exhibits a pole at $Q^2 = \Lambda^2_{\overline{MS}}$, which indicates that perturbation theory is no longer valid for small values of Q^2.

1.2 QCD at electron–positron colliders

After neglecting the quark masses, the only free parameter of the QCD Lagrangian given in Eq. (1.1) is g_s and, derived from it, α_s. Together with the choice of the gauge group it fully defines the properties of the theory. Over the last decades there has been a great number of experiments dedicated to the study of these properties, mostly at particle colliders. In the following we concentrate on measurements of α_s at $\mathrm{e^+e^-}$ colliders, where a wealth of data in the energy range from 12 GeV to 206 GeV has been collected at various experiments, allowing the detailed study of the energy dependence of QCD. These precision studies rely on the measurement of the three-jet production cross section and related event-shape observables. The deviation from simple two-jet configurations is proportional to the strong coupling constant α_s. Hence, comparing the measured three-jet rate and related event shapes (see Sections 1.2.1 and 1.2.2) with the theoretical predictions allows the determination of α_s. For further details on the determination of the structure constants and experiments at other colliders see for example Ref. [19].

In $\mathrm{e^+e^-}$ annihilation a virtual photon or Z boson is produced, which then decays into fermion–antifermion pairs. For the study of QCD the production of quark–antiquark pairs is particularly interesting. Since the electron and positron are not charged under the strong interaction, the initial state is well defined in terms of QCD and does not interact with the final state. Furthermore, apart from initial-state radiation of photons, the energy of the final state is fixed.

The total hadronic cross section σ_had is given by the cross section of the process $\mathrm{e^+e^-} \to$ hadrons to all orders in α_s, i.e. the production of an arbitrary number of jets in $\mathrm{e^+e^-}$ collisions. At leading order σ_had is given by σ_0, the Born level cross section of the process $\mathrm{e^+e^-} \to q\bar{q}$, which as a function of the centre-of-mass energy squared s reads

$$\sigma_0(s) = \frac{4\pi\alpha^2}{3s}\left[Q_q^2 - 2Q_qV_eV_q\chi_1(s) + \left(A_e^2+V_e^2\right)\left(A_q^2+V_q^2\right)\chi_2(s)\right], \tag{1.12}$$

where α is the fine structure constant, Q_q is the charge of the quark, and V_i and A_i are the vector and axial-vector couplings of particle i to the Z boson. The first term stems from the exchange of a photon, the third from the exchange of a Z boson, and the second from the photon-Z interference. The functions χ_i are given by

$$\chi_1(s) = \frac{\sqrt{2}G_\mathrm{F}M_\mathrm{Z}^2}{16\pi\alpha}\frac{s\left(s-M_\mathrm{Z}^2\right)}{\left(s-M_\mathrm{Z}^2\right)^2+\Gamma_\mathrm{Z}^2M_\mathrm{Z}^2}, \quad \chi_2(s) = \frac{2G_\mathrm{F}^2M_\mathrm{Z}^4}{256\pi^2\alpha^2}\frac{s^2}{\left(s-M_\mathrm{Z}^2\right)^2+\Gamma_\mathrm{Z}^2M_\mathrm{Z}^2}, \tag{1.13}$$

where G_F is the Fermi constant and Γ_Z is the width of the Z boson. The ratio of the total hadronic cross section to the total cross section for muon production $R_{\mathrm{e^+e^-}}$ can be used to study QCD while electroweak effects are suppressed. For $\sqrt{s}$ much below the Z resonance one finds

$$R_{\mathrm{e^+e^-}} = N_\mathrm{C}\sum_q Q_q^2, \tag{1.14}$$

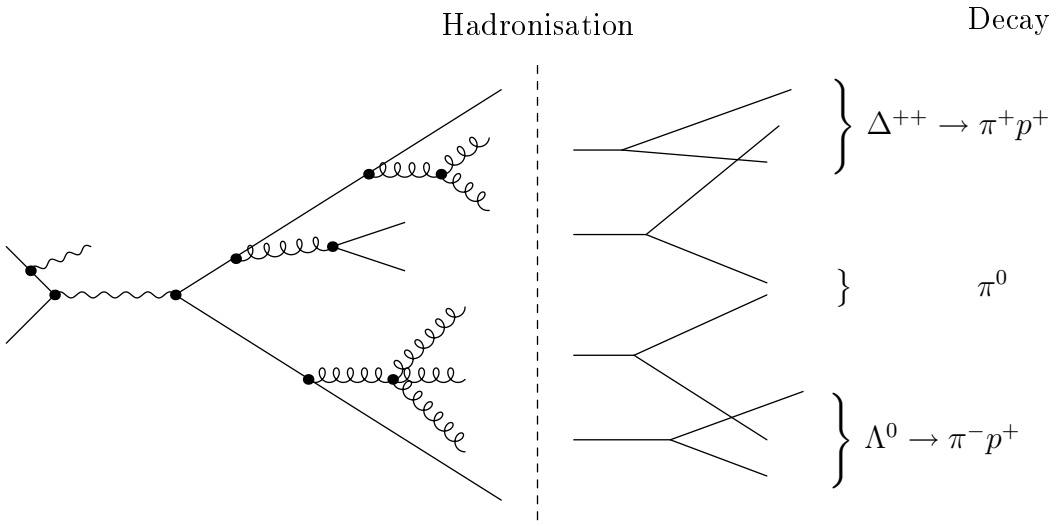

Figure 1.2: Schematic view of the hadronisation process.

and for $\sqrt{s} = M_{\mathrm{Z}}$

$$R_{\mathrm{e^+e^-}} = N_{\mathrm{C}} \sum_q \frac{\left(A_q^2 + V_q^2\right)}{\left(A_\mu^2 + V_\mu^2\right)}. \tag{1.15}$$

$R_{\mathrm{e^+e^-}}$ is a good example for a fully inclusive quantity, i.e. a quantity that makes use of all observed momenta and does not depend on the particular structure of the final state. It has been used to experimentally confirm that the number of colours is $N_{\mathrm{C}} = 3$.

In the leading-order picture, the quark–antiquark pair is produced back-to-back, resulting in a two-jet structure of the event. At the next order in α_{s}, a gluon can be emitted from the quark or antiquark, leading to a deviation from this two-jet structure due to the appearance of additional jets. In the next sections we explain how this behaviour can be exploited for the measurement of α_{s} using event-shape observables.

Due to QCD confinement, no asymptotically-free coloured objects can exist, and therefore there has to be a transition from coloured quarks and gluons in the final state to colourless hadrons. This process is called hadronisation and cannot be described perturbatively. A schematic picture of hadronisation can be found in Fig. 1.2. Based on parton shower algorithms, models to describe the hadronisation process have been developed and implemented into Monte Carlo programs, which are used to analyse the experimental data.

A particular feature of the multi-particle final state in $\mathrm{e^+e^-}$ annihilation is its jet structure, i.e. the final state hadrons are collimated in bundles in the direction of the initial parton. Based on this structure one can build observables which can be measured in experiments and calculated in QCD. They are usually divided into two groups: jet observables and event-shape observables. Both types have to obey the

Sterman-Weinberg criteria of infrared-safety. To illustrate this, consider an observable $O_n(p_1, \ldots, p_n)$ which is defined using an n-particle final state, where the momentum of each particle i is denoted by p_i. If the observable $O_n(p_1, \ldots, p_n)$ is infrared-safe, in the limit $p_i || p_j$ (collinear limit) or in the limit $p_i \to 0$ (soft limit) it behaves like

$$\begin{aligned} O_n(p_1, \ldots, p_n) &\xrightarrow{p_1 || p_2} O_{n-1}(p_1 + p_2, \ldots, p_n), \\ O_n(p_1, \ldots, p_n) &\xrightarrow{E_1 \to 0} O_{n-1}(p_2, \ldots, p_n). \end{aligned} \tag{1.16}$$

In the following we discuss further details of jet and event-shape observables.

1.2.1 Jet observables

A commonly used method for reconstructing jets was originally introduced by the JADE group [20]. The algorithm is based on successive combinations. In a first step, each observed particle is listed as a jet. In the next step, a resolution parameter y_{ij} is calculated and the particle pair leading to the smallest value of y_{ij} is combined into a single pseudo-particle. This yields a new list of jets, and the algorithm proceeds with step two. The procedure is repeated until there is no pair of particles left with $y_{ij} < y_{\text{cut}}$, where y_{cut} is a preset cutoff.

There exist different proposals in the literature in how to define y_{ij}. The original JADE definition is

$$y_{ij,\text{J}} = \frac{2E_iE_j\,(1 - \cos\theta_{ij})}{s}, \tag{1.17}$$

where E_i is the energy of the i-th particle, $\cos\theta_{ij}$ is the angle between the particles, and s is the centre-of-mass energy squared. It can be shown that hadronisation effects are small when calculating jet rates using the above algorithm. On the other hand, perturbative corrections are large, especially for small y_{cut}. Additionally, it has been shown in [21] that jet fractions defined in the above way do not follow the usual Sudakov exponentiation for multiple soft-gluon emission, which is an important ingredient for calculations using resummation techniques. Therefore different definitions of the jet resolution parameter have been proposed, for example the k_{T} or Durham algorithm [22], which defines

$$y_{ij,\text{D}} = \frac{2\min\left(E_i^2, E_j^2\right)(1 - \cos\theta_{ij})}{s}, \tag{1.18}$$

or the Geneva algorithm Ref. [23] proposing

$$y_{ij,\text{G}} = \frac{8}{9}\frac{E_iE_j\,(1 - \cos\theta_{ij})}{(E_i + E_j)^2}. \tag{1.19}$$

In addition to the choice of jet resolution parameter, there also exist different ways of combining the four-momenta of the two particles with the lowest y_{ij} to one four-momentum p_{ij}. In the so-called E-scheme one simply adds the two four-momenta,

leading to $p_{ij} = p_i + p_j$. In the P-scheme the invariant mass of the pseudo-particle is set to zero by rescaling the energy

$$\begin{aligned} \vec{p}_{ij} &= \vec{p}_i + \vec{p}_j, \\ E_{ij} &= |\vec{p}_i + \vec{p}_j|. \end{aligned} \tag{1.20}$$

In the P_0-scheme Eq. (1.20) is used to construct the resulting four-momentum. However, after each recombination the centre-of-mass energy s is recalculated. Finally, in the E_0-scheme the three-momentum rather than the energy is rescaled. The four schemes differ in the results for finite $y_{\rm cut}$, but yield comparable results for small $y_{\rm cut}$ and can therefore be used for resummed calculations. In Ref. [23] a numerical comparison of the different schemes can be found.

Since an event containing three jets is due to the emission of a gluon off an (anti-)quark at a large angle and with significant energy, the ratio of the number of observed three-jet to two-jet events is, in leading order, proportional to the strong coupling constant. In general, the n-jet rate $R_n(y)$, which depends on the choice of the jet resolution parameter $y = y_{\rm cut}$, is defined through the respective cross sections for $n \geq 2$ jets

$$R_n(y, \sqrt{s}) = \frac{\sigma_{n-\rm jet}}{\sigma_{\rm had}}, \tag{1.21}$$

such that

$$\sum_{n=1}^{\infty} R_n(y) = 1. \tag{1.22}$$

1.2.2 Event-shape observables

In order to characterise the topology of an event a large number of observables have been developed. Most of them require at least three momenta of final-state particles to be non-zero. In the following we introduce six variables which have been extensively used in experimental analyses: thrust T [24, 25], the normalised heavy-jet mass $M_{\rm H}^2/s$ [26], the wide and total jet broadenings $B_{\rm W}$ and $B_{\rm T}$ [27, 28], the C-parameter [29, 30], and the transition from three-jet to two-jet final-state using $y_{ij,\rm D}$ [21–23, 31, 32].

- Thrust is defined through

$$T = \max_{\vec{n}} \frac{\sum_i |\vec{p}_i \cdot \vec{n}|}{\sum_i |\vec{p}_i|}, \tag{1.23}$$

  where $\vec{p}_i$ is the three-momentum of the i-th particle, and $\vec{n}$ is varied to maximise the momentum flow in its direction. For a two-jet, back-to-back event, one finds $T = 1$, whereas for a three-jet event the minimum value is $T = 2/3$.

- Every event can be divided into two hemispheres H_1 and H_2 by a plane perpendicular to the thrust axis. In each hemisphere H_i one can calculate the invariant mass M_i^2, the larger of which yields the heavy-jet mass

$$M_H^2 = \max\left(M_1^2, M_2^2\right), \tag{1.24}$$

and the normalised heavy-jet mass

$$\rho = M_{\mathrm{H}}^2/s, \tag{1.25}$$

where s is the centre-of-mass energy squared. In the limit of a two-jet event one finds $\rho \to 0$, whereas for a three-jet event $\rho \leq 1/3$. The heavy-jet mass distribution is identical to the $1-T$ distribution for a three jet event at leading-order.

- Using the definition of the hemispheres from above, one can calculate the hemisphere broadening

$$B_i = \frac{\sum_{j \in H_i} |\vec{p}_j \times \vec{n}|}{2 \sum_j |\vec{p}_j|}. \tag{1.26}$$

The wide and total jet broadenings B_{W} and B_{T} are then obtained through

$$\begin{aligned} B_{\mathrm{W}} &= \max\left(B_1, B_2\right), \\ B_{\mathrm{T}} &= B_1 + B_2. \end{aligned} \tag{1.27}$$

In the limit of a two-jet event one finds $B_{\mathrm{W}} \to 0$ and $B_{\mathrm{T}} \to 0$, whereas for a three-jet event $B_{\mathrm{W}} = B_{\mathrm{T}} = 1/(2\sqrt{3})$.

- Starting from the linearised momentum tensor

$$\Theta^{\alpha\beta} = \frac{1}{\sum_j |\vec{p}_j|} \sum_j \frac{p_j^\alpha p_j^\beta}{|\vec{p}_j|}, \qquad \alpha, \beta = 1, 2, 3, \tag{1.28}$$

and its three eigenvalues $\lambda_1, \lambda_2, \lambda_3$, the C-parameter is defined through

$$C = 3\left(\lambda_1\lambda_2 + \lambda_2\lambda_3 + \lambda_3\lambda_1\right). \tag{1.29}$$

- The jet transition variable Y_3 is defined as the value of the jet resolution parameter for which an event changes from a three-jet-like to a two-jet-like configuration.

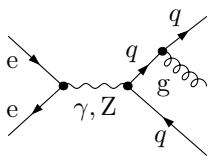

Figure 1.3: The process $e^+e^- \to q\bar{q}g$.

1.2.3 Event shapes and jet rates in perturbation theory

At $\mathcal{O}(\alpha_s)$, the first process that occurs at tree-level in e^+e^- annihilation is gluon radiation off a quark or antiquark, see Fig. 1.3. As mentioned above, by comparing the measured three-jet rate and event-shape observables with theoretical predictions, one can determine α_s.

In perturbation theory up to NNLO in QCD, the expansion of a distribution in the generic observable y at centre-of-mass energy $\sqrt{s}$ for renormalisation scale $\mu = \sqrt{s}$ and $\alpha_s = \alpha_s(s)$, normalised to $\sigma_0(s)$ from Eq. (1.12), is given by

$$\frac{1}{\sigma_0}\frac{\mathrm{d}\sigma}{\mathrm{d}y} = \left(\frac{\alpha_s}{2\pi}\right)\frac{\mathrm{d}A}{\mathrm{d}y} + \left(\frac{\alpha_s}{2\pi}\right)^2\frac{\mathrm{d}B}{\mathrm{d}y} + \left(\frac{\alpha_s}{2\pi}\right)^3\frac{\mathrm{d}C}{\mathrm{d}y} + \mathcal{O}\left(\alpha_s^4\right). \tag{1.30}$$

The experimentally measured event-shape distribution is normalised to the total hadronic cross section σ_{had}, which for massless quarks is given by

$$\sigma_{\mathrm{had}} = \sigma_0\left(1 + \left(\frac{\alpha_s}{2\pi}\right)K_1 + \left(\frac{\alpha_s}{2\pi}\right)^2 K_2 + \mathcal{O}\left(\alpha_s^3\right)\right), \tag{1.31}$$

such that

$$\frac{1}{\sigma_{\mathrm{had}}}\frac{\mathrm{d}\sigma}{\mathrm{d}y} = \left(\frac{\alpha_s}{2\pi}\right)\frac{\mathrm{d}\bar{A}}{\mathrm{d}y} + \left(\frac{\alpha_s}{2\pi}\right)^2\frac{\mathrm{d}\bar{B}}{\mathrm{d}y} + \left(\frac{\alpha_s}{2\pi}\right)^3\frac{\mathrm{d}\bar{C}}{\mathrm{d}y} + \mathcal{O}\left(\alpha_s^4\right), \tag{1.32}$$

where

$$\begin{aligned} \bar{A} &= A, \\ \bar{B} &= B - AK_1, \\ \bar{C} &= C - BK_1 + AK_1^2 - AK_2. \end{aligned} \tag{1.33}$$

The coefficients in Eq. (1.33) up to NLO have been calculated in Refs. [33–38]. Furthermore, kinematically-dominant leading and next-to-leading logarithms have been resummed [39, 40] and non-perturbative models of power-suppressed hadronisation effects have been included [41–44] to increase the theoretical accuracy. Recently the first NNLO calculation has been completed [45] and the matching of NLL and NNLL to the fixed-order NNLO calculation has been performed [46–48].

With regards to jet rates, fixed-order calculations are known up to next-to-next-to-next-to-leading order (N^3LO) in QCD for the two-jet rate [49–52], up to NNLO for the three-jet rate [33–38, 52, 53], and up to NLO for the four-jet rate [54–58].

NLO electroweak (EW) corrections could be of comparable magnitude as the NNLO QCD corrections and are therefore worth further consideration. The factorisable EW corrections have been calculated in Ref. [59] and a first attempt for the full NLO EW corrections has been made in Ref. [60].

In analogy to the QCD corrections, we write the total hadronic cross section including $\mathcal{O}(\alpha)$ corrections as

$$\sigma_{\text{had}} = \sigma_0 \left(1 + \left(\frac{\alpha}{2\pi}\right) \delta_{\sigma,1} + \mathcal{O}\left(\alpha^2\right)\right), \tag{1.34}$$

and the expansion of the observable y as

$$\frac{1}{\sigma_0}\frac{\mathrm{d}\sigma}{\mathrm{d}y} = \frac{\mathrm{d}A}{\mathrm{d}y} + \left(\frac{\alpha}{2\pi}\right)\frac{\mathrm{d}\delta_\gamma}{\mathrm{d}y} + \left(\frac{\alpha}{2\pi}\right)\frac{\mathrm{d}\delta_A}{\mathrm{d}y} + \mathcal{O}\left(\alpha^2\right), \tag{1.35}$$

where the LO purely electromagnetic contribution δ_γ arises from tree-level quark–antiquark–photon ($q\bar{q}\gamma$) final states without a gluon.

Normalising Eq. (1.35) to σ_{had} we find

$$\frac{1}{\sigma_{\text{had}}}\frac{\mathrm{d}\sigma}{\mathrm{d}y} = \frac{\mathrm{d}A}{\mathrm{d}y} + \left(\frac{\alpha}{2\pi}\right)\left(\frac{\mathrm{d}\delta_\gamma}{\mathrm{d}y} + \frac{\mathrm{d}\delta_A}{\mathrm{d}y} - \frac{\mathrm{d}A}{\mathrm{d}y}\delta_{\sigma,1}\right) + \mathcal{O}\left(\alpha^2\right). \tag{1.36}$$

Hence, the full $\mathcal{O}(\alpha)$ electroweak corrections are given by

$$\frac{\mathrm{d}\delta_{\text{EW}}}{\mathrm{d}y} = \left(\frac{\alpha}{2\pi}\right)\left(\frac{\mathrm{d}\delta_\gamma}{\mathrm{d}y} + \frac{\mathrm{d}\delta_A}{\mathrm{d}y} - \frac{\mathrm{d}A}{\mathrm{d}y}\delta_{\sigma,1}\right). \tag{1.37}$$

In order to obtain a meaningful ratio, all three contributions have to be evaluated using the same event-selection cuts.

The EW corrections to both σ_{had} and the distribution in y contain large corrections due to initial-state radiation. Since these are universal, they partially cancel in the second term in Eq. (1.36), leaving only a small remainder. If we want to include higher-order ISR effects in both σ_{had} and the distribution in y, this leads to

$$\sigma_{\text{had}} = \sigma_0 \left(1 + \left(\frac{\alpha}{2\pi}\right)\delta_{\sigma,1} + \left(\frac{\alpha}{2\pi}\right)^2 \delta_{\sigma,\geq 2,\text{LL}} + \mathcal{O}\left(\alpha^3\right)\right), \tag{1.38}$$

and

$$\frac{1}{\sigma_0}\frac{\mathrm{d}\sigma}{\mathrm{d}y} = \frac{\mathrm{d}A}{\mathrm{d}y} + \left(\frac{\alpha}{2\pi}\right)\frac{\mathrm{d}\delta_\gamma}{\mathrm{d}y} + \left(\frac{\alpha}{2\pi}\right)\frac{\mathrm{d}\delta_A}{\mathrm{d}y} + \left(\frac{\alpha}{2\pi}\right)^2 \frac{\mathrm{d}\delta_{A,\geq 2,\text{LL}}}{\mathrm{d}y} + \mathcal{O}\left(\alpha^3\right), \tag{1.39}$$

where $\delta_{\sigma,\geq 2,\mathrm{LL}}$ and $\delta_{A,\geq 2,\mathrm{LL}}$ contain leading-logarithmic terms proportional to $\alpha^n \ln^n\left(\frac{s}{m_\mathrm{e}^2}\right)$ with $n \geq 2$, as defined in Section 2.3.6. In the normalised distribution this yields

$$\begin{aligned}\frac{1}{\sigma_\mathrm{had}}\frac{\mathrm{d}\sigma}{\mathrm{d}y} &= \frac{\mathrm{d}A}{\mathrm{d}y} + \left(\frac{\alpha}{2\pi}\right)\left(\frac{\mathrm{d}\delta_\gamma}{\mathrm{d}y} + \frac{\mathrm{d}\delta_A}{\mathrm{d}y} - \frac{\mathrm{d}A}{\mathrm{d}y}\delta_{\sigma,1}\right) \\ &\quad + \left(\frac{\alpha}{2\pi}\right)^2\left[\left(\frac{\mathrm{d}\delta_{A,\geq 2,\mathrm{LL}}}{\mathrm{d}y} - \frac{\mathrm{d}A}{\mathrm{d}y}\delta_{\sigma,\geq 2,\mathrm{LL}}\right) - \frac{\mathrm{d}\delta_{A,1,\mathrm{LL}}}{\mathrm{d}y}\delta_{\sigma,1,\mathrm{LL}} + \frac{\mathrm{d}A}{\mathrm{d}y}\delta_{\sigma,1,\mathrm{LL}}^2\right] + \mathcal{O}\left(\alpha^3\right),\end{aligned} \tag{1.40}$$

where $\delta_{A,1,\mathrm{LL}}$ and $\delta_{\sigma,1,\mathrm{LL}}$ denote the leading-logarithmic contributions contained in the NLO results. Therefore, the higher-order leading-logarithmic corrections read

$$\frac{\mathrm{d}\delta_{\mathrm{EW,LL}}}{\mathrm{d}y} = \left(\frac{\mathrm{d}\delta_{A,\geq 2,\mathrm{LL}}}{\mathrm{d}y} - \frac{\mathrm{d}A}{\mathrm{d}y}\delta_{\sigma,\geq 2,\mathrm{LL}}\right) + \left(\frac{\mathrm{d}A}{\mathrm{d}y}\delta_{\sigma,1,\mathrm{LL}}^2 - \frac{\mathrm{d}\delta_{A,1,\mathrm{LL}}}{\mathrm{d}y}\delta_{\sigma,1,\mathrm{LL}}\right). \tag{1.41}$$

Due to the universality of ISR, the terms in the first and in the second bracket in Eq. (1.41) separately cancel each other numerically.

Note that a term of the order $\alpha_\mathrm{s}\alpha$, i.e. a mixed QCD–EW term, numerically leads to a contribution of the same size as the term $\alpha^2 \ln^2\left(s/m_\mathrm{e}^2\right)$. However, such a two-loop term is beyond the scope of this thesis.

In the above discussion we concentrated on event-shape distributions. However, the same procedure can be applied to the three- and four-jet rate, since both experimentally measured quantities are normalised to σ_had.

1.2.4 Particle identification

As already stated, one of the virtues of $\mathrm{e^+e^-}$ colliders is the precise knowledge of the energy of the final state. However, initial-state radiation (ISR) of photons can lead to difficulties in the determination of the total energy of the final state. Therefore event-selection cuts have been devised to suppress effects due to ISR. In the following we describe the procedure employed by the ALEPH collaboration at LEP [61].

First, particles are clustered into jets according to the Durham algorithm with $y_\mathrm{cut,D} = 0.002$. Jets where the fraction of energy carried by charged hadrons is less than 10% are identified as dominantly electromagnetic and are removed. In the next step the remaining particles are clustered into two jets and the visible invariant mass M_vis of the two-jet system is calculated. Using total momentum conservation the reduced centre-of-mass energy s' is calculated. The event is rejected if $s'/s < 0.81$. This two-step procedure is later referred to as hard-photon cut procedure (note that it is called anti-ISR cut procedure in Ref. [61]).

Removing events where the photonic energy in a jet is higher than a certain value as it is done in the hard-photon cuts causes potential problems when perturbatively

calculating electroweak corrections for processes at e^+e^- colliders. There one relies on the cancellation of infrared singularities between virtual and real corrections when calculating an infrared-safe observable. Removing events where a photon is close to a final-state charged fermion leads to non-infrared-safe observables and spoils this cancellation in the collinear region. A procedure to define an infrared-safe observable in the presence of hard-photon cuts is presented at a later stage.

1.3 Goal of this thesis

In the previous section we have seen the precision up to which event shapes and jet rates have been calculated, using perturbative QCD up to NNLO, resummation techniques, and estimates of non-perturbative effects. At this point, electroweak corrections also become important in reducing theoretical uncertainties and therefore deserve further investigation.

In this thesis we calculate corrections to the process $e^+e^- \to 3\,\text{jets}$ at $\mathcal{O}(\alpha^3\alpha_s)$. Therefore we compute the NLO electroweak corrections to the process $e^+e^- \to q\bar{q}g$ and the QCD corrections to the process $e^+e^- \to q\bar{q}\gamma$. Both contributions involve the calculation of the virtual corrections, as well as the real emission process $e^+e^- \to q\bar{q}g\gamma$. In the following we refer to the 'full $\mathcal{O}(\alpha)$' corrections when we include the NLO electroweak corrections to the process $e^+e^- \to q\bar{q}g$, the QCD corrections to the process $e^+e^- \to q\bar{q}\gamma$, and the real emission process $e^+e^- \to q\bar{q}g\gamma$.

The IR singularities related to soft or collinear photon or gluon emission in the Bremsstrahlung process are cancelled by the corresponding singularities in the virtual corrections, when calculating infrared-safe observables. The case where both the photon and the gluon become soft or collinear leads to a singularity which in principle would be cancelled by the two-loop mixed QCD and electroweak corrections, which we do not consider in this work. This singularity only contributes to the endpoint of the respective distribution, typically the first bin, and we avoid it by imposing a lower cut-off in all distributions which does not distort their shape outside the two-jet region.

In the calculation at hand, the photon is always treated like a parton, i.e. it enters the jet algorithm or the calculation of event shapes. Only the hard-photon cuts as described in Section 1.2.4 distinguish it from a strongly interacting particle. They also render all observables non-infrared-safe as described in Section 1.2. To restore the infrared safety of the observables, we use a fragmentation-function approach that fully recovers the cancellation of collinear divergencies.

The corrections discussed above are put into a Monte Carlo program, which can calculate simultaneously all the event shapes and jet rates described in Section 1.2.1 and Section 1.2.2 at arbitrary centre-of-mass energies. The program supports unpolarised, as well as polarised electron beams, and has the option to include higher-order ISR effects.

The event-shape distributions are usually normalised to the total hadronic cross section σ_{had}, which at the Born level is given by σ_0 in Eq. (1.12). Therefore we also calculate the NLO electroweak corrections to the process $\mathrm{e}^+\mathrm{e}^- \to q\bar{q}$, which are implemented into a Monte Carlo program, similar to the one described above.

Using the results mentioned above, we have all the ingredients to calculate the coefficients δ_{EW} and $\delta_{\mathrm{EW,LL}}$ as defined in Eq. (1.37) and Eq. (1.41). These coefficients can then be used for the analysis of the LEPI and LEPII data and the determination of the strong coupling constant α_{s} in the range of energies from M_{Z} to 206 GeV.

Chapter 2

Strategy of the Calculation

In this chapter we discuss the different ingredients needed for an NLO calculation of the process $e^+e^- \to 3$ jets. We also calculate the NLO electroweak corrections to the process $e^+e^- \to q\bar{q}$ to properly account for the normalisation of the distributions as defined in Eq. (1.37). The calculation of the NLO corrections to three-jet production is more involved than the calculation of the NLO corrections to σ_{had}. However, the strategies we need are in principle the same. In the following we therefore focus on the details of the calculation of the NLO corrections to the process $e^+e^- \to 3$ jets and point out possible differences when calculating the NLO corrections to the process $e^+e^- \to q\bar{q}$.

We decompose the total cross section for three-jet production according to

$$\begin{aligned}\int \mathrm{d}\sigma &= \int \mathrm{d}\sigma_{\text{Born}}^{e^+e^- \to q\bar{q}g} + \int \mathrm{d}\sigma_{\text{Born}}^{e^+e^- \to q\bar{q}\gamma} \\ &+ \int \mathrm{d}\sigma_{\text{virtual,EW}}^{e^+e^- \to q\bar{q}g} + \int \mathrm{d}\sigma_{\text{virtual,QCD}}^{e^+e^- \to q\bar{q}\gamma} + \int \mathrm{d}\sigma_{\text{real}}^{e^+e^- \to q\bar{q}g\gamma}, \end{aligned} \tag{2.1}$$

where the first and third terms are the Born and NLO electroweak contributions of the process $e^+e^- \to q\overline{q}g$, the second and fourth terms are the Born and NLO QCD contributions of the process $e^+e^- \to q\overline{q}\gamma$, and the fifth term is the contribution from the real radiation process $e^+e^- \to q\overline{q}g\gamma$. The virtual and real radiation corrections are of $\mathcal{O}(\alpha^3\alpha_s)$ and lead to the production of three or four jets, when treating photons and hadrons democratically.

In the following sections we describe in detail the calculation of the individual contributions, starting in the first section with introducing our notation using the Born cross section as an example.

In the second section we give a survey of the contributing one-loop diagrams, present an algorithm for the analytic simplification of the loop amplitude, describe how we calculate the loop integrals, motivate our choice of renormalisation scheme, and present a formula for the IR-singular part of the virtual corrections.

In the third section we describe how we approach the real emission process, focus-

ing on the treatment of soft and collinear divergencies, especially when dealing with non-collinear safe observables. According to the KLN theorem [62, 63], divergencies coming from soft and/or collinear emission of photons in the final state cancel each other when calculating an infrared-safe observable. Similarly, the Bloch-Nordsieck [64] theorem ensures the cancellation of soft singularities in the initial state. We regularise collinear initial-state singularities with the mass of the electron. However, in the presence of the hard-photon cuts, infrared-safety is no longer given. Thus we show how we can incorporate a fragmentation-function approach that allows us to define infrared-safe observables in the presence of these cuts and restores the cancellation of soft and collinear divergencies, which is then carried out analytically.

2.1 Conventions and lowest-order cross section

At the parton level we consider the processes

$$\begin{aligned} \mathrm{e}^+(k_1,\sigma_1) + \mathrm{e}^-(k_2,\sigma_2) &\to q(k_3,\sigma_3) + \bar{q}(k_4,\sigma_4), && (2.2)\\ \mathrm{e}^+(k_1,\sigma_1) + \mathrm{e}^-(k_2,\sigma_2) &\to q(k_3,\sigma_3) + \bar{q}(k_4,\sigma_4) + \mathrm{g}(k_5,\lambda), && (2.3)\\ \mathrm{e}^+(k_1,\sigma_1) + \mathrm{e}^-(k_2,\sigma_2) &\to q(k_3,\sigma_3) + \bar{q}(k_4,\sigma_4) + \gamma(k_5,\lambda), && (2.4) \end{aligned}$$

where q can be an up, down, charm, strange, or bottom quark. The momenta k_i of the corresponding particles as well as their helicities σ_i and λ are given in parentheses. The helicities of the fermions take the values $\sigma_i = 1/2$, and the helicity of the gluon or the photon assumes the values $\lambda = \pm 1$. The external momenta fulfil the mass-shell conditions $k_{1,2}^2 = m_\mathrm{e}^2$, $k_{3,4}^2 = m_q^2$, $k_5^2 = 0$. We neglect the masses of the external fermions wherever possible and keep them only as regulators of the mass-singular logarithms. Therefore all amplitudes vanish unless $\sigma_1 = -\sigma_2$ and $\sigma_3 = -\sigma_4$. Thus, we define $\sigma = \sigma_1 = -\sigma_2$ and $\sigma' = \sigma_3 = -\sigma_4$.

For later use, the following set of kinematical invariants is introduced:

$$s = (k_1 + k_2)^2\,, \quad s_{ij} = (k_i + k_j)^2\,, \quad t_{li} = (k_l - k_i)^2\,, \quad l = 1,2,\ i,j = 3,4,5. \qquad (2.5)$$

The Feynman diagrams contributing to the process Eq. (2.2) are shown in Fig. 2.1, those contributing to the process Eq. (2.3) in Fig. 2.2, and the ones contributing to the process Eq. (2.4) in Fig. 2.3.

The lowest-order partonic cross section for the processes given in Eqs. (2.3) and (2.4) reads

$$\int \mathrm{d}\sigma_\mathrm{Born} = \frac{1}{2s} \int \mathrm{d}\Phi_3 F_\mathrm{C} \sum_{\substack{\sigma,\sigma'=\pm\frac{1}{2}\\ \lambda=\pm 1}} \frac{1}{4}(1+2P_1\sigma)(1-2P_2\sigma)\,|\mathcal{M}_0^{\sigma\sigma'\lambda}|^2 \Theta_\mathrm{cut}\left(\Phi_3\right), \qquad (2.6)$$

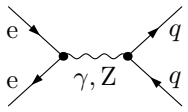

Figure 2.1: Lowest-order diagram for $e^+e^- \to q\bar{q}$.

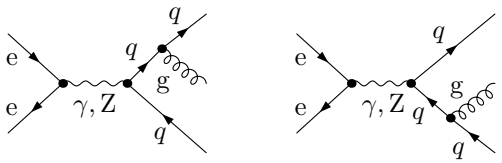

Figure 2.2: Lowest-order diagrams for $e^+e^- \to q\bar{q}g$.

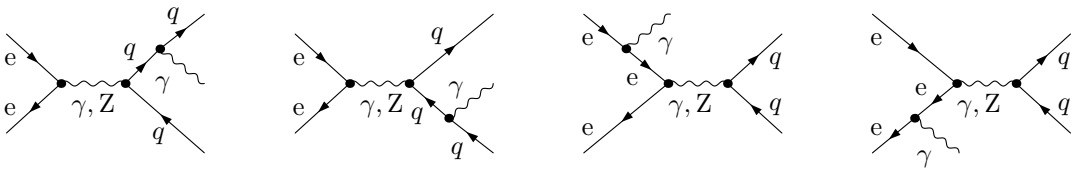

Figure 2.3: Lowest-order diagrams for $e^+e^- \to q\bar{q}\gamma$.

where F_{C} is a colour factor, $P_{1,2}$ are the degrees of the polarisation of the incoming e^+ and e^-, $\mathcal{M}_0^{\sigma\sigma'\lambda}$ is the Born matrix element of the respective process, and the integral over the three-particle phase space is defined by

$$\int \mathrm{d}\Phi_3 = \left(\prod_{i=3}^{5} \int \frac{\mathrm{d}^3\vec{k}_i}{(2\pi)^3 2k_i^0} \right) (2\pi)^4 \delta\left(k_1 + k_2 - \sum_{j=3}^{5} k_j \right). \tag{2.7}$$

For the process Eq. (2.4) we find $F_{\mathrm{C}} = 3$, and for the process Eq. (2.3) $F_{\mathrm{C}} = 4$. The dependence of the cross section on the event-selection cuts is reflected by $\Theta_{\mathrm{cut}}(\Phi_3)$. For the lowest-order cross section and the virtual corrections, Θ_{cut} depends on three-particle kinematics. It is equal to 1 if the event passes the cuts and equal to 0 otherwise.

The formula corresponding to the process Eq. (2.2) can be obtained from Eq. (2.6) by omitting the dependence on the polarisation of photon, using only the two-particle phase space, and setting $F_{\mathrm{C}} = 3$. The analytical form of the Born matrix elements for all processes considered in this work can be found in Section A.2.

2.2 Virtual corrections

We calculate the NLO EW corrections to the processes given in Eqs. (2.2) and (2.3), and the NLO QCD corrections to the process given in Eq. (2.4). To this end we write

$$\int \mathrm{d}\sigma_{\mathrm{virtual}} = \frac{1}{2s} \int \mathrm{d}\Phi_3 F_{\mathrm{C}} \sum_{\substack{\sigma,\sigma'=\pm\frac{1}{2} \\ \lambda=\pm 1}} \frac{1}{4}(1+2P_1\sigma)(1-2P_2\sigma)\, 2\mathrm{Re}\Big[\mathcal{M}_0^{\sigma\sigma'\lambda} \left(\mathcal{M}_1^{\sigma\sigma'\lambda}\right)^*\Big] \Theta_{\mathrm{cut}}(\Phi_3), \tag{2.8}$$

where the notation is the same as in the previous section and $\mathcal{M}_1^{\sigma\sigma'\lambda}$ denotes the matrix element of the virtual corrections.

The NLO EW virtual corrections receive contributions from self-energy, vertex, box, and in the case where we have a gluon in the final state, also pentagon diagrams. The structural diagrams for the process with gluon emission containing the generic contributions of all possible vertex functions are shown in Fig. 2.4. The structural diagrams for the process without gluon emission can be obtained by taking the first four and the sixth diagrams of Fig. 2.4 and neglecting the gluon. We do not show the specific one-loop contributions to the Z boson, photon, and quark self-energies (they can be found for example in Ref. [65]), while the specific three-point contributions are shown in Fig. 2.5, and the box and pentagon contributions in Fig. 2.6.
The symbol q stands for the quarks defined in Eq. (2.3), the symbols q' for their weak isospin partners. Since we neglect the masses of the external fermions wherever possible, there are obviously no contributions of the Higgs boson coupling to those particles. We do not depict diagrams which can be obtained by reversing the charge flow of the external quark lines in the first six diagrams of Fig. 2.4.

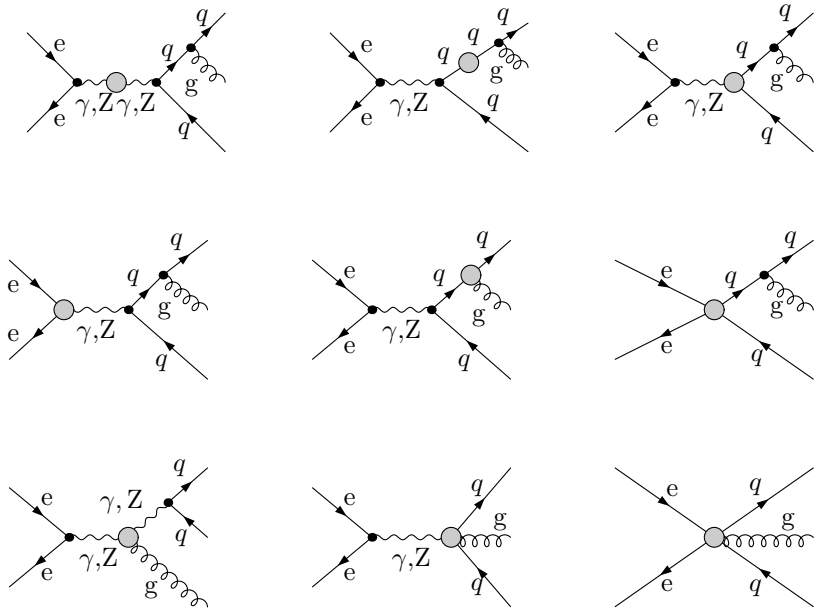

Figure 2.4: Contributions of all possible vertex functions to $e^+e^- \to q\bar{q}g$.

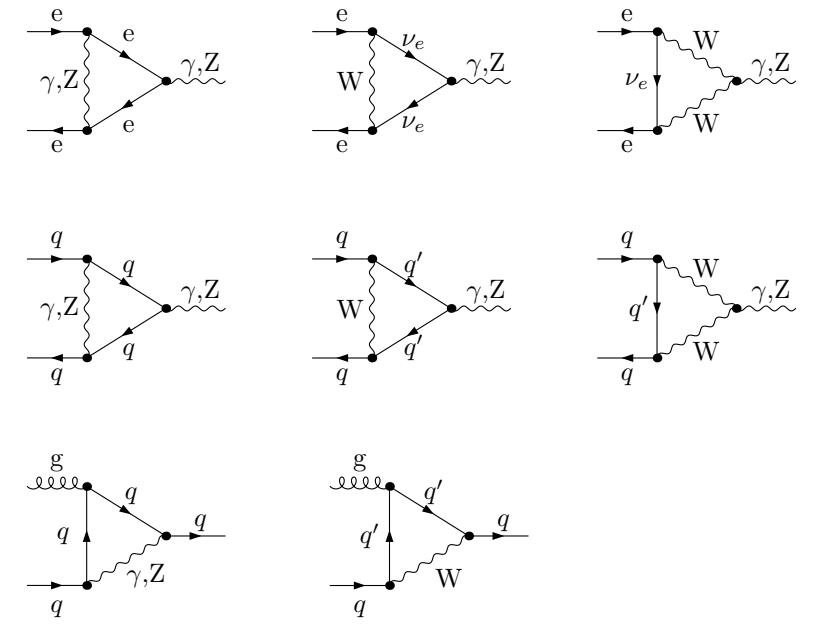

Figure 2.5: Diagrams for the $\gamma q\bar{q}$, $Zq\bar{q}$, γe^+e^-, Ze^+e^- and $gq\bar{q}$ vertex functions.

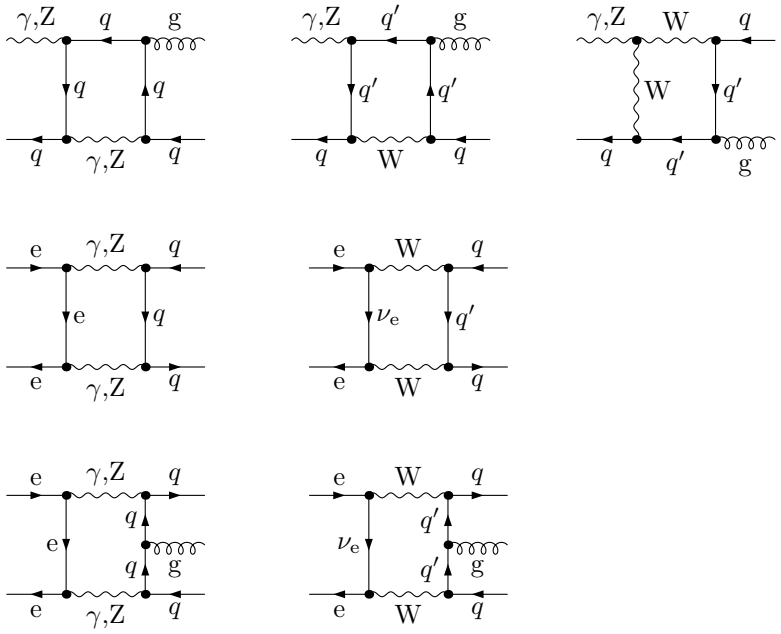

Figure 2.6: Diagrams for the $\gamma g q\bar{q}$, $\mathrm{Z}g q\bar{q}$, $\mathrm{ee}q\bar{q}$, and $\mathrm{ee}q\bar{q}\mathrm{g}$ vertex functions.

In total we have $\mathcal{O}(200)$ contributing diagrams in the 't Hooft–Feynman gauge for the process with gluon emission and $\mathcal{O}(80)$ for the process without gluon emission, counting closed fermion loop diagrams for each family only once.

The NLO QCD virtual corrections receive contributions from self-energy, vertex, and box diagrams. The corresponding Feynman diagrams are shown in Fig. 2.7, where we have omitted quark self-energy contributions. We do not depict diagrams which can be obtained by either reversing the charge flow of the external quark lines in the first two diagrams or the external lepton lines in the third diagram of Fig. 2.7. In total we have $\mathcal{O}(20)$ contributing diagrams in this case.

In the following we describe how we algebraically simplify the loop amplitudes.

2.2.1 Algebraic reduction of spinor chains

We generated the amplitudes using the program FeynArts version 3.2 [66] and employed the program FormCalc version 5 [67] to algebraically manipulate the amplitudes, which led to 150 different spinor structures. In order to reduce the number of spinor structures, we applied the algorithm described in Ref. [68] and extended it to the case with one external gauge boson. It is possible to reduce all occurring spinor chains to $\mathcal{O}(20)$ standard structures, the standard matrix elements (SMEs), without creating

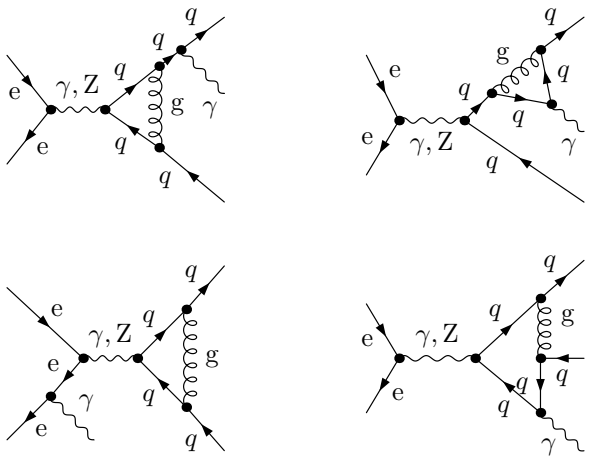

Figure 2.7: QCD corrections to the process $e^+e^- \to q\bar{q}\gamma$.

coefficients that lead to numerical problems.

After the reduction of the spinor structures, we separate the matrix elements into invariant coefficients F_n, which are functions of the one-loop integrals, scalar kinematical variables, particle masses, and coupling factors, and SMEs $\hat{\mathcal{M}}$, which contain all spinorial objects and the dependence on the helicities of the external particles (see Ref. [69]):

$$\mathcal{M}^{\sigma\sigma'\lambda} = \sum_n F_n^{\sigma\sigma'\lambda}\left(\{s, s_{ij}, t_{li}\}\right) \hat{\mathcal{M}}_n^{\sigma\sigma'\lambda}\left(k_1, k_2, k_3, k_4, k_5\right). \tag{2.9}$$

Throughout the calculation we encounter the product of two Dirac chains corresponding to the incoming leptonic and the outgoing hadronic current. An open Lorentz index inside one of the Dirac chains can be contracted with an open Lorentz index inside the other Dirac chain, or with an external momentum, or with the polarisation vector $\epsilon_\mu^*(k_5, \lambda)$ of the outgoing photon or gluon.

We use the short-hand notation

$$[A]_{ab}^{\pm\lambda} = \bar{v}_a(k_a)\, A^\lambda\, \omega_\pm\, u_b(k_b), \tag{2.10}$$

for a spinor chain, where $\bar{v}_a(k_a)$ and $u_b(k_b)$ are spinors for fermions and antifermions respectively, with the chirality projectors

$$\omega_\pm = \frac{1}{2}(1 \pm \gamma_5), \tag{2.11}$$

and the helicity λ of the external gluon or photon. In the following, we denote the external polarisation vector by ϵ^* when there is no ambiguity. Since we work with

massless external fermions, only odd numbers of Dirac matrices occur inside the spinor chains. Using this convention, the objects we want to simplify are of the form

$$\bar{v}_1(k_1)\, A^\lambda\, \omega_\rho\, u_2(k_2) \;\times\; \bar{v}_3(k_3)\, B^\kappa\, \omega_\sigma\, u_4(k_4) = [A]_{12}^{\rho\lambda}[B]_{34}^{\sigma\kappa}. \tag{2.12}$$

In this section we choose all momenta incoming. We make use of the Dirac algebra, the Dirac equation for the external fermions, momentum conservation, and the four-dimensionality of space-time, which can be exploited after the cancellation of UV-divergencies, which are dimensionally regularised in our work. Through the Chisholm identity, one can relate a product of three Dirac matrices to a sum where each summand only consists of a single Dirac matrix multiplied by the metric tensor $g^{\mu\nu}$, or γ_5 and the totally antisymmetric tensor $\epsilon^{\mu\nu\rho\sigma}$:

$$\gamma^\mu\gamma^\nu\gamma^\rho = g^{\mu\nu}\gamma^\rho - g^{\mu\rho}\gamma^\nu + g^{\nu\rho}\gamma^\mu + \mathrm{i}\epsilon^{\mu\nu\rho\sigma}\gamma^\sigma\gamma_5. \tag{2.13}$$

An additional consequence of the four-dimensionality of space-time is the fact that one can decompose the metric tensor $g^{\mu\nu}$ in terms of four linearly independent orthonormal basis vectors n_l (see Refs. [70, 71])

$$g^{\mu\nu} = n_0^\mu n_0^\nu - \sum_{l=1}^{3} n_l^\mu n_l^\nu, \tag{2.14}$$

with $n_k \cdot n_l = g_{kl}$. We choose the metric tensor $g^{\mu\nu}$ to be $g^{\mu\nu} = \mathrm{diag}(1,-1,-1,-1)$. A convenient choice of the four vectors n_l in terms of three linearly independent massless external momenta k_i, k_j, k_k is given by

$$\begin{aligned}
n_0^\mu(k_i,k_j,k_k) &= \frac{1}{\sqrt{2(k_ik_j)}}\left(k_i^\mu + k_j^\mu\right), \quad n_1^\mu(k_i,k_j,k_k) = \frac{1}{\sqrt{2(k_ik_j)}}\left(k_i^\mu - k_j^\mu\right), \\
n_2^\mu(k_i,k_j,k_k) &= -\frac{1}{\sqrt{2(k_ik_j)(k_ik_k)(k_jk_k)}}\Big[(k_jk_k)k_i^\mu + (k_ik_k)k_j^\mu - (k_ik_j)k_k^\mu\Big], \\
n_3^\mu(k_i,k_j,k_k) &= -\frac{1}{\sqrt{2(k_ik_j)(k_ik_k)(k_jk_k)}}\epsilon^{\mu\alpha\beta\gamma}k_{i,\alpha}k_{j,\beta}k_{k,\gamma}.
\end{aligned} \tag{2.15}$$

In particular the choice of the totally antisymmetric tensor $\epsilon^{\mu\alpha\beta\gamma}$ as a fourth independent object guarantees the absence of inverse Gram determinants.

In four space-time dimensions a totally antisymmetric tensor of rank five cannot exist, which leads to the Schouten identity

$$\epsilon_{[\alpha\beta\gamma\delta}g_{\mu]\nu} = 0, \tag{2.16}$$

where $[\ldots]$ means antisymmetrisation of $\alpha, \beta, \gamma, \delta, \mu$. The product of two totally antisymmetric tensors can be expressed in terms of a determinant of metric tensors,

$$\epsilon^{\alpha\beta\gamma\delta}\epsilon^{\mu\nu\rho\sigma} = \begin{vmatrix} g^{\alpha\mu} & g^{\alpha\nu} & g^{\alpha\rho} & g^{\alpha\sigma} \\ g^{\beta\mu} & g^{\beta\nu} & g^{\beta\rho} & g^{\beta\sigma} \\ g^{\gamma\mu} & g^{\gamma\nu} & g^{\gamma\rho} & g^{\gamma\sigma} \\ g^{\delta\mu} & g^{\delta\nu} & g^{\delta\rho} & g^{\delta\sigma} \end{vmatrix}. \tag{2.17}$$

Let us now turn to the description of how to reduce the spinor chains to a minimal set of basis structures. In the first step we disconnect two spinor chains which are contracted with each other using the decomposition Eq. (2.14),

$$\gamma_\mu \otimes \gamma^\mu = \not{n}_0 \otimes \not{n}_0 - \sum_{i=1}^{3} \not{n}_i \otimes \not{n}_i. \tag{2.18}$$

The choice of the external momenta in the above decomposition strongly depends on the position of the contracted Dirac matrices inside the spinor chain. It is advantageous to choose them in such a way that one can make use of the Dirac equation $\bar{v}(k_i)\not{k}_i = 0 = \not{k}_i u(k_i)$ and the mass-shell condition $k_i^2 = \not{k}_i^2 = 0$ in a very direct manner, avoiding unnecessary anticommutations. We follow the algorithm described in detail in Ref. [68]. After simplifying the expressions using the identities above, there are remaining contributions from the contraction of a basis vector n_3 with a Dirac matrix inside the spinor chains, which can be transformed by employing the Chisholm identity

$$\not{n}_3(k_i,k_j,k_k) = -\frac{\mathrm{i}\big[\ \not{k}_i\ \not{k}_j\ \not{k}_k - (k_ik_j)\ \not{k}_k + (k_ik_k)\ \not{k}_j - (k_jk_k)\ \not{k}_i\big]\gamma_5}{\sqrt{2(k_ik_j)(k_ik_k)(k_jk_k)}}. \tag{2.19}$$

In the calculation at hand, we have to deal with a maximum of three contractions between the two spinor chains. After disconnecting them, we are left with objects of the form $[\not{v}_j]^{\pm}_{ab}$, where the vector v_j can either be an external momentum k_j, $j \neq a,b$, or the polarisation vector ϵ^* of the external gluon or photon.

In the next step, we reduce the structures which do not depend on the polarisation vector of the gluon or photon using the relation

$$\not{k}_m \;=\; \gamma_\mu k_m^\mu = \gamma_\mu g^{\mu\nu} k_{m,\nu} \overset{(2.14)}{=} k_{m,\mu} n_0^\mu\ \not{n}_0 - \sum_{i=1}^{3} k_{m,\mu} n_i^\mu\ \not{n}_i, \quad m \neq a,b,n. \tag{2.20}$$

Consider for example

$$\begin{aligned}
\Big[\not{k}_m\Big]^{\pm}_{ab} &\overset{(2.20)}{=} k_{m,\mu} \sum_{i=0}^{3} g^{ii}\, n_i^\mu(k_a,k_b,k_n) \Big[\not{n}_i(k_a,k_b,k_n)\Big]^{\pm}_{ab} \\
&\overset{(2.19)}{=} \frac{(k_ak_n)\,(k_bk_m) - (k_ak_b)\,(k_nk_m) + (k_ak_m)\,(k_nk_b) \pm \mathrm{i}\,\epsilon_{a\,n\,b\,m}}{2\,(k_ak_n)\,(k_bk_n)} \Big[\not{k}_n\Big]^{\pm}_{ab} \\
&\overset{(2.22)}{=} \frac{1}{2\,(k_ak_n)\,(k_bk_n)}\, A^{+-+\mp}_{a\,n\,b\,m} \Big[\not{k}_n\Big]^{\pm}_{ab},
\end{aligned} \tag{2.21}$$

where we introduced the abbreviations

$$\begin{aligned}
A^{a\,b\,c\,d}_{v\,j\,k\,l} &= a\,(vk_j)\,(k_ak_l) + b\,(vk_k)\,(k_jk_l) + c\,(vk_l)\,(k_jk_k) - d\,\mathrm{i}\,\epsilon_{v\,j\,k\,l}, \\
\epsilon_{vjkl} &= \epsilon_{\alpha\beta\gamma\delta}\, v^\alpha k_j^\beta k_k^\gamma k_l^\delta,
\end{aligned} \tag{2.22}$$

and upper index combinations $(--++\pm)$, $(+-+\pm)$, and $(++-\pm)$ for $(a\,b\,c\,d)$. The component v can in our case be either an external momentum, i.e. $v = i$ for k_i, or the polarisation vector of the gluon or photon, i.e. $v = \epsilon^*$, which we include for later use.

We are now able to express all spinor chains in terms of a linear combination of 20 SMEs

$$[\epsilon^*]^{\sigma}_{12}\,[k_1]^{\tau}_{34}\,,\ [k_3]^{\sigma}_{12}\,[\epsilon^*]^{\tau}_{34}\,,\ (\epsilon^* k_1)\,[k_3]^{\sigma}_{12}\,[k_1]^{\tau}_{34}\,,\ (\epsilon^* k_2)\,[k_3]^{\sigma}_{12}\,[k_1]^{\tau}_{34}\,,\ (\epsilon^* k_3)\,[k_3]^{\sigma}_{12}\,[k_1]^{\tau}_{34}\,. \tag{2.23}$$

The reduction of all spinor chains to this basis introduces at most two summands per spinor chain and a total of six factors of the form Eq. (2.22). Inserting the SMEs Eq. (2.23) into the amplitude reduces its size by a factor of two.

A second option is to also reduce terms of the form $[\not{\epsilon}^*]^{\pm}_{ab}$ using

$$\not{\epsilon}^* = \gamma_\mu \epsilon^{*\mu} = \gamma_\mu g^{\mu\nu} \epsilon^*_\nu \overset{(2.14)}{=} \epsilon^*_\mu n_0^\mu \not{n}_0 - \sum_{i=1}^{3} \epsilon^*_\mu n_i^\mu \not{n}_i, \tag{2.24}$$

which leads for example to

$$\begin{aligned}[\epsilon^*]^{\pm}_{ab} \overset{(2.24)}{=} \frac{1}{2\,(k_a k_c)\,(k_b k_c)} \Big\{ &(k_b k_c)\,(\epsilon^* k_a) + (k_a k_c)\,(\epsilon^* k_b) \\ &- (k_a k_b)\,(\epsilon^* k_c) \pm \mathrm{i}\epsilon_{\epsilon^* abc} \Big\}\, [k_c]^{\pm}_{ab}\,,\end{aligned} \tag{2.25}$$

where we have used the momenta k_a, k_b, k_c in the decomposition Eq. (2.14). Instead of having the polarisation vector $\epsilon^*_\mu(k)$ inside a Dirac chain, we find a sum of fermionic standard structures multiplied by a factor which contains scalar products of an external momentum and the polarisation vector and the totally antisymmetric tensor contracted with three momenta and the polarisation vector. In this way we find the 28 SMEs

$$\begin{gathered}(\epsilon^* k_1)\,[k_3]^{\sigma}_{12}\,[k_1]^{\tau}_{34}\,,\ (\epsilon^* k_2)\,[k_3]^{\sigma}_{12}\,[k_1]^{\tau}_{34}\,,\ (\epsilon^* k_3)\,[k_3]^{\sigma}_{12}\,[k_1]^{\tau}_{34}\,, \\ \epsilon_{\epsilon^* 123}\,[k_3]^{\sigma}_{12}\,[k_1]^{\tau}_{34}\,,\ \epsilon_{\epsilon^* 124}\,[k_3]^{\sigma}_{12}\,[k_1]^{\tau}_{34}\,,\ \epsilon_{\epsilon^* 134}\,[k_3]^{\sigma}_{12}\,[k_1]^{\tau}_{34}\,,\ \epsilon_{\epsilon^* 234}\,[k_3]^{\sigma}_{12}\,[k_1]^{\tau}_{34}\,,\end{gathered} \tag{2.26}$$

and we can express each spinor chain in terms of a sum of four terms. Due to the increased number of terms involved in the reduction of the original spinor chains, the size of the amplitude is not reduced in this approach.

We could also write the sums described above in terms of Eq. (2.22), for example

$$[\epsilon^*]^{\pm}_{ab} \overset{(2.22)}{=} \frac{1}{2\,(k_a k_c)\,(k_b k_c)} A^{+\,+\,-\,\mp}_{\epsilon^* a\; b\; c}\,[k_c]^{\pm}_{ab}\,. \tag{2.27}$$

This would lead, however, to a total of 108 SMEs, almost the same number that we started from.

A third option is to use only three specific momenta in the decomposition Eq. (2.24), which leaves us only with one of the ϵ–terms above, e.g.

$$\begin{aligned}[\epsilon^*]^{\pm}_{ab} \overset{(2.22)}{=} & \left[\left(-\frac{(k_b k_c)}{(k_a k_c)\,(k_c k_d)} + \frac{A^{++-\mp}_{a\,b\,c\,d}}{2\,(k_a k_c)\,(k_c k_d)\,(k_a k_d)}\right)(\epsilon^* k_c)\right. \\ & + \left(\frac{1}{(k_c k_d)} - \frac{A^{++-\mp}_{a\,b\,c\,d}}{2\,(k_b k_c)\,(k_c k_d)\,(k_a k_d)}\right)(\epsilon^* k_d) \\ & + \left(\frac{1}{(k_a k_c)} - \frac{A^{++-\mp}_{a\,b\,c\,d}}{2\,(k_a k_c)\,(k_b k_c)\,(k_a k_d)}\right)(\epsilon^* k_a) \\ & \left. \pm \mathrm{i}\left(\frac{1}{2\,(k_a k_c)\,(k_c k_d)} - \frac{A^{++-\mp}_{a\,b\,c\,d}}{4\,(k_a k_c)\,(k_b k_c)\,(k_c k_d)\,(k_a k_d)}\right)\epsilon_{\epsilon^* acd}\right][k_c]^{\pm}_{ab}\,, \end{aligned} \tag{2.28}$$

where we chose to use only the momenta k_a, k_c, k_d in the decomposition Eq. (2.24). It turns out that we can express each spinor chain in terms of a sum of eight terms with the 20 SMEs

$$(\epsilon^* k_1)\,[k_3]^{\sigma}_{12}\,[k_1]^{\tau}_{34}\,,\ (\epsilon^* k_2)\,[k_3]^{\sigma}_{12}\,[k_1]^{\tau}_{34}\,,\ (\epsilon^* k_3)\,[k_3]^{\sigma}_{12}\,[k_1]^{\tau}_{34}\,,\ \epsilon_{\epsilon^* 123}\,[k_3]^{\sigma}_{12}\,[k_1]^{\tau}_{34}\,. \tag{2.29}$$

The size of the amplitude after inserting these SMEs is 13% larger than using the SMEs Eq. (2.26), since we need twice as many terms in the reduction of the spinor chains. Again we could write Eq. (2.28) in terms of Eq. (2.22), which results in

$$[\epsilon^*]^{\pm}_{ab} = \frac{1}{2\,(k_c k_d)\,(k_a k_c)}\left[A^{-++\mp}_{\epsilon\,a\,c\,d} + \frac{1}{2\,(k_b k_c)\,(k_a k_d)} A^{+-+\pm}_{\epsilon\,a\,c\,d} A^{++-\mp}_{a\,b\,c\,d}\right][k_c]^{\pm}_{ab}\,. \tag{2.30}$$

Applying this approach we find in general 36 polarisation dependent structures, which is almost twice the number we need in Eq. (2.23). Due to the results of the above analysis, we choose to use the SMEs given in Eq. (2.23) in our calculation.

In addition to the three procedures described above, we can express one of the scalar products between the polarisation vector of the gluon or photon and an external momentum in terms of scalar products between the polarisation vector of the gluon or photon and the other two external momenta, again using the decomposition of the metric tensor, e.g.

$$\begin{aligned}\epsilon^*_\mu k^\mu_a = \epsilon^*_\mu g^{\mu\nu} k_{a,\nu} \overset{(2.24)}{=} & \frac{1}{2}\left(\frac{(k_a k_c)}{(k_b k_c)} + \frac{(k_a k_5)}{(k_b k_5)} - \frac{(k_a k_b)\,(k_c k_5)}{(k_b k_c)\,(k_b k_5)}\right)(\epsilon^* k_b) \\ + & \frac{1}{2}\left(\frac{(k_a k_b)}{(k_b k_c)} + \frac{(k_a k_5)}{(k_c k_5)} - \frac{(k_a k_c)\,(k_b k_5)}{(k_b k_c)\,(k_c k_5)}\right)(\epsilon^* k_c)\,, \end{aligned} \tag{2.31}$$

where we used the momenta k_b, k_c, k_5 to span the metric tensor and the transversality condition of the polarisation vector

$$\epsilon^*_\mu(k) k^\mu = 0. \tag{2.32}$$

In all three approaches described above, using Eq. (2.31) increases the size of the amplitude by roughly 10%, which is the reason why we do not employ Eq. (2.31) in our calculation.

In the case of the virtual corrections to $\sigma_{\rm had}$, we use the four SMEs

$$[k_3]^{\sigma}_{12}\,[k_1]^{\tau}_{34}\,. \tag{2.33}$$

2.2.2 Evaluation of the loop integrals

The tensor integrals are evaluated as in the calculation of Refs. [68, 72], i.e. they are numerically reduced to master integrals. The scalar master integrals are computed using complex masses according to Refs. [73–75]. UV divergencies are regulated dimensionally, whereas IR singularities are regulated using an infinitesimal photon or gluon mass. Five-point integrals are reduced to four-point integrals according to Refs. [76, 77]. As long as no small Gram determinant appears in the reduction of three- and four-point functions, we use the usual Passarino-Veltman reduction [78]. If a small Gram determinant appears, we expand the tensor coefficient around this small determinant or other small kinematical quantities, as described in Ref. [77]. This procedure is implemented into the FORTRAN library COLI of A. Denner, which we use in our Monte Carlo program.

We treat the gauge-boson widths using the complex-mass scheme, which has been worked out at the Born level in Ref. [79] and at the one-loop level in Ref. [68]. In this framework the masses of the Z and the W boson are complex quantities, defined at the pole of the corresponding propagator in the complex plane. As a consequence, derived quantities like the weak mixing angle also become complex, and the renormalisation procedure has to be slightly modified. Introducing complex masses everywhere in the Feynman rules preserves all algebraic relations like Ward identities and therefore also gauge invariance. It can be shown that terms that break gauge invariance are of higher order in perturbation theory (see Ref. [68]).

2.3 The Bremsstrahlung process

In this section we describe how we evaluate the last term in Eq. (2.1). The process we consider is given by

$$\mathrm{e}^+(q_1,\sigma_1)+\mathrm{e}^-(q_2,\sigma_2)\to q(q_3,\sigma_3)+\bar{q}(q_4,\sigma_4)+\mathrm{g}(k_1,\lambda_1)+\gamma(k_2,\lambda_2),\quad q=\mathrm{u},\mathrm{d},\mathrm{c},\mathrm{s},\mathrm{b}, \tag{2.34}$$

and we have

$$\int \mathrm{d}\sigma_{\rm real}=\frac{1}{2s}\int \mathrm{d}\Phi_4 F_{\rm C}\sum_{\substack{\sigma,\sigma'=\pm\frac{1}{2}\\ \lambda_1,\lambda_2=\pm1}}\frac{1}{4}(1+2P_1\sigma)(1-2P_2\sigma)\,|\mathcal{M}^{\sigma\sigma'\lambda_1\lambda_2}_{\rm real}|^2\Theta_{\rm cut}\left(\Phi_4\right). \tag{2.35}$$

The corresponding matrix elements $\mathcal{M}_{\text{real}}^{\sigma\sigma'\lambda_1\lambda_2}$ are given in Section A.3, the four-particle phase space reads

$$\mathrm{d}\Phi_4 = \frac{1}{(2\pi)^{12}} \frac{\mathrm{d}^3 q_3}{2q_3^0} \frac{\mathrm{d}^3 q_4}{2q_4^0} \frac{\mathrm{d}^3 k_1}{2k_1^0} \frac{\mathrm{d}^3 k_2}{2k_2^0} (2\pi)^4 \delta^{(4)} (q_1 + q_2 - q_3 - q_4 - k_1 - k_2) , \tag{2.36}$$

and $F_{\text{C}} = 4$. As in Eq. (2.6), the theta function $\Theta_{\text{cut}}(\Phi_4)$ represents cuts used in the event selection. It is equal to 1 if the event passes the cuts and equal to 0 otherwise.

The integral over the four-particle phase space contains IR divergencies due to the emission of a soft or collinear photon or gluon. Since we want to use numerical techniques such as Monte Carlo integration to evaluate the integral, we have to isolate these divergencies and combine them with the corresponding contributions from the virtual corrections. In the following we introduce two different methods that address this issue. One is the phase-space-slicing method of Refs. [37,80–84], where the idea is to split the phase space into singular and non-singular regions, treat the singular regions analytically, and evaluate the finite remainder numerically. The other is the dipole subtraction method of Ref. [38,85,86], where a subtraction function that mimics the singular behaviour of the integrand is added and subtracted, leaving a finite four-particle phase space integration and a remainder, where the integration that leads to singularities is carried out analytically.

In both methods one relies on factorisation properties of the matrix elements and of the phase space in the soft and collinear limit. The singularities are treated analytically such that a numerical integration does not pose any problems.

Both methods described above are valid for NLO calculations. We employ them separately for the photon and the gluon in the calculation at hand. However, they are not sufficient in the region where both the photon and the gluon become soft or collinear. This region corresponds to two-jet production where the photon and the gluon are unresolved. The singularities in this region are cancelled by the mixed two-loop QCD and EW corrections to quark–antiquark pair production and are beyond the scope of this thesis. Effects due to doubly soft or collinear radiation are contained in the endpoint of the corresponding distribution only. Therefore, if we ignore the endpoint, typically the last bin of a distribution, in our analysis, our results are not jeopardised by these singularities.

To be able to compare the results of our calculation to experimental measurements and to improve the accuracy of the theoretical prediction of α_s, we have to incorporate the kinematical cuts used in the specific experiment. In this work, we implement the event selection and kinematical cuts used in the ALEPH collaboration, as already described in Section 1.2.4.

Therefore we remove electromagnetic jets in the phase-space integration by imposing an upper cut on the photon energy in the jet. However, the cut on the photon energy also removes events with a highly energetic photon collinear to a quark or antiquark in the final state that lead to a configuration where the photon and quark cannot

be distinguished. These are exactly the events needed when defining infrared-safe observables. To restore infrared-safety, we introduce the photon fragmentation function, a function that is experimentally determined and contains the singularities needed to ensure the cancellation of IR divergencies from real and virtual corrections, in analogy to the absorption of collinear singularities into PDFs at hadron colliders.

Collinear photon emission in the initial state is regulated by the mass of the electron and leads to large contributions of the form $\ln(m_e^2/s)$. The cut on the visible invariant mass M_{vis} removes hard photons collinear to the incoming beam particles and therefore suppresses large mass-singular logarithms.

In this section we first introduce the collinear-safe phase-space slicing and subtraction methods, before we present an algorithm to extend both methods to non-collinear-safe observables.

In Sections 2.3.1 and 2.3.2 we describe the phase-space slicing and the subtraction methods for photon radiation. Both methods are implemented for both photon and gluon radiation. The corresponding formulae for gluon radiation can simply be obtained through the replacement $\alpha \to 4/3\,\alpha_s$, since we do not encounter effects due to triple or quartic gluon couplings.

We illustrate both methods for the case of non-infrared-safe event-selection cuts in Sections 2.3.3 and 2.3.4. Furthermore, we describe how we remove the left-over singularities using the experimentally determined quark-to-photon fragmentation function in Section 2.3.5. Only photons are identified in jets, therefore the fragmentation function procedure is only needed in the case of real photon emission.

In Section 2.3.6 we show a method to also incorporate higher-order ISR terms using the structure-function approach.

2.3.1 Phase-space slicing

In this section we describe the phase-space slicing method according to Refs. [84, 87]. The splitting of the phase space into singular and non-singular parts is achieved by introducing a cut δ_s on the photon energy $E_\gamma < \delta_s\sqrt{s}/2 = \Delta E$ in the CM frame. The collinear region is defined by $E_\gamma > \Delta E$ and $1 > \cos\theta > 1 - \delta_c$, where θ is the angle between the photon and the fermion in the CMS. We can now decompose the cross section into a soft, a collinear, and a finite part:

$$\mathrm{d}\sigma_{\text{real}} = \mathrm{d}\sigma_{\text{soft}} + \mathrm{d}\sigma_{\text{coll.}} + \mathrm{d}\sigma_{\text{finite}}. \tag{2.37}$$

In the soft region the squared matrix element $|\mathcal{M}_{\text{real}}|^2$ and $\mathrm{d}\Phi_4$ factorise such that we can apply the soft photon approximation given in Refs. [69, 88] and write

$$\mathrm{d}\sigma_{\text{soft}} = \mathrm{d}\sigma_{\text{Born}} \frac{\alpha}{4\pi^2} \sum_{i=1}^{4} \sum_{j=i+1}^{4} (-1)^{i+j} Q_i Q_j \int_{\substack{E_\gamma < \Delta E \\ |\vec{k}|^2 = E_\gamma^2 - m_\gamma^2}} \frac{\mathrm{d}^3 k}{E_\gamma} \left(\frac{q_i^\mu}{k q_i} - \frac{q_j^\mu}{k q_j} \right)^2, \tag{2.38}$$

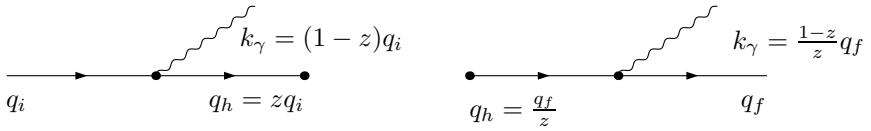

Figure 2.8: Kinematics of the initial- and final-state splitting.

where we denote the photon momentum by k and keep the photon mass m_γ as a regulator. The integrals in Eq. (2.38) can be solved analytically, see Refs. [69, 89], as

$$\begin{aligned} \mathrm{d}\sigma_{\mathrm{soft}} &= \mathrm{d}\sigma_{\mathrm{Born}} \frac{\alpha}{2\pi} \sum_{i=1}^{4} \sum_{j=i+1}^{4} (-1)^{i+j} Q_i Q_j \\ &\quad \times \left\{ 2 \ln\left(\frac{2\Delta E}{m_\lambda}\right) \left[2 - \ln\left(\frac{s_{ij}^2}{m_i^2 m_j^2}\right) \right] - 2 \ln\left(\frac{4E_i E_j}{m_i m_j}\right) \right. \\ &\quad \left. + \frac{1}{2} \ln^2\left(\frac{4E_i^2}{m_i^2}\right) + \frac{1}{2} \ln^2\left(\frac{4E_j^2}{m_j^2}\right) + \frac{2\pi^2}{3} + 2\mathrm{Li}_2\left(1 - \frac{4E_i E_j}{s_{ij}}\right) \right\}, \end{aligned} \tag{2.39}$$

where we keep the masses of the fermions as regulators for the collinear singularities ($E_i \gg m_i$).

We now turn to the initial- and final-state hard contributions, which contain mass-singular logarithms in the limit where the photon and the (anti-)quark become collinear.

In the case of initial-state radiation the phase space factorises according to (see Fig. 2.8 for notation)

$$\mathrm{d}\Phi_4\left(i + i' \to f + f' + g + \gamma\right) \to \mathrm{d}\Phi_3\left(h + i' \to f + f' + g\right) \frac{\mathrm{d}^3 k}{2(2\pi)^3 k^0} = -\mathrm{d}\Phi_3 \frac{\mathrm{d}z \mathrm{d}\delta_i}{16\pi^2}, \tag{2.40}$$

and in the case of final-state radiation according to

$$\mathrm{d}\Phi_4\left(i + i' \to f + f' + g + \gamma\right) \to \mathrm{d}\Phi_3\left(i + i' \to h + f' + g\right) \frac{z^2 \mathrm{d}^3 k}{2(2\pi)^3 k^0} = -\mathrm{d}\Phi_3 \frac{\mathrm{d}z \mathrm{d}\delta_f}{16\pi^2}, \tag{2.41}$$

where we have used

$$\mathrm{d}^3 k = 2\pi \left(k^0\right)^2 \mathrm{d}k^0 \mathrm{d}\cos\theta, \;\; \mathrm{d}\delta_{i,f} = 2k^0 q_{i,f}^0 \mathrm{d}\cos\theta, \;\; \mathrm{d}k^0 = -q_i^0 \mathrm{d}z = -\frac{1}{z^2} q_f^0 \mathrm{d}z. \tag{2.42}$$

In the same manner the matrix element for initial-state radiation factorises according to

$$\sum \left|\mathcal{M}_{\mathrm{real}}\left(i + i' \to f + f' + g + \gamma\right)\right|^2 \to \sum \left|\mathcal{M}_{\mathrm{Born}}\left(h + i' \to f + f' + g\right)\right|^2 c_{i \to h\gamma}, \tag{2.43}$$

and for final-state radiation according to

$$\sum |\mathcal{M}_{\text{real}}\left(i+i' \to f+f'+g+\gamma\right)|^2 \to \sum |\mathcal{M}_{\text{Born}}\left(i+i' \to h+f'+g\right)|^2 c_{f\gamma\to h}. \tag{2.44}$$

In the equations above we used

$$\begin{aligned} c_{i\to h\gamma} &= 8\pi^2 \frac{\alpha}{\pi} Q_i^2 \frac{1}{\delta_i}\left[\frac{1+z^2}{z(1-z)} - \frac{2m_i^2}{\delta_i}\right], \\ c_{f\gamma\to h} &= 8\pi^2 \frac{\alpha}{\pi} Q_f^2 \frac{1}{\delta_f}\left[\frac{1+z^2}{1-z} - \frac{2m_f^2}{\delta_f}\right], \end{aligned} \tag{2.45}$$

where m_i (m_f) is the mass of the initial- (final-) state fermion that emits the photon and

$$\begin{aligned} \delta_i &= |\left(q_i-k\right)^2 - m_i^2| = |2k^0 q_i^0 \left(1-\cos\theta\right)|, \\ \delta_f &= |\left(q_f+k\right)^2 - m_f^2| = |2k^0 q_f^0 \left(1-\cos\theta\right)|. \end{aligned} \tag{2.46}$$

Putting Eq. (2.41) [Eq. (2.42)] and Eq. (2.43) [Eq. (2.44)] together, we find with $E_i \gg m_i$ and up to $\mathcal{O}(m_i/E_i)$

$$\begin{aligned} \mathrm{d}\sigma_{\text{coll.}}^{\text{initial}} &= \sum_{i=1,2} \int_0^{1-\delta_s} \mathrm{d}z\, \mathrm{d}\sigma_{\text{Born}}\left(zq_i\right) \int_{(1-z)m_i^2}^{2(1-z)(q_i^0)^2\delta_c} \mathrm{d}\delta_i \frac{z}{16\pi^2} c_{i\to h\gamma} \\ &= \sum_{i=1,2} \sum_{\kappa_i} \frac{\alpha}{2\pi} Q_i^2 \int_0^{1-\delta_s} \mathrm{d}z \left\{ \mathrm{d}\sigma_{\text{Born}}\left(zq_i, +\kappa_i\right) \frac{1+z^2}{1-z}\left[\ln\left(\frac{\hat{s}}{m_i^2}\frac{\delta_c}{2}\frac{1}{z}\right) - 1\right] \right. \\ &\qquad \left. + \mathrm{d}\sigma_{\text{Born}}\left(zq_i, -\kappa_i\right)\left(1-z\right)\right\}, \end{aligned} \tag{2.47}$$

and

$$\begin{aligned} \mathrm{d}\sigma_{\text{coll.}}^{\text{final}} &= \sum_{i=3,4} \int_0^{1-\Delta E/E_i} \mathrm{d}z\, \mathrm{d}\sigma_{\text{Born}}\left(q_i\right) \int_{(1-z)m_i^2/z}^{2z(1-z)(q_h^0)^2\delta_c} \mathrm{d}\delta_f \frac{1}{16\pi^2} c_{f\gamma\to h} \\ &= \sum_{i=3,4} \sum_{\kappa_i} \frac{\alpha}{2\pi} Q_i^2 \left\{ \mathrm{d}\sigma_{\text{Born}}\left(q_i, +\kappa_i\right) \int_0^{1-\Delta E/E_i} \mathrm{d}z \frac{1+z^2}{1-z}\left[\ln\left(\frac{4E_i^2}{m_i^2}\frac{\delta_c}{2}z^2\right) - 1\right] \right. \\ &\qquad \left. + \mathrm{d}\sigma_{\text{Born}}\left(q_i, -\kappa_i\right)\frac{1}{2}\right\}. \end{aligned} \tag{2.48}$$

The limits in the inner integration in Eq. (2.47) and Eq. (2.48) are determined from Eq. (2.46). In the collinear region they are given by

$$\delta_i < 2(1-z)\left(q_i^0\right)^2 \delta_c, \qquad \delta_f < 2(1-z)z\left(q_h^0\right)^2 \delta_c. \tag{2.49}$$

In the above equations we introduced a spin-flip term, denoted by the fermion helicity κ_i, that gives rise to a finite contribution and is needed when we want to consider polarised incoming beams. The spin-flip term leads to a non-vanishing contribution if both the electron and positron have the same polarisation.

In the case of initial-state radiation $\hat{s} = zs$ is the CM energy of the hard scattering after the emission of the collinear photon, which leads to the extra factor z in the first line of Eq. (2.47). In the case of final-state radiation the integral over $\mathrm{d}z$ can be performed if the photon and the fermion off which it has been radiated cannot be observed separately, but only a pseudo-particle carrying the sum of their momenta. Consequently, the Born matrix element squared is also only dependent on the sum of the two momenta and we find

$$\begin{aligned}\mathrm{d}\sigma_{\text{coll.}}^{\text{final}} &= \sum_{i=3}^{4}\sum_{\kappa_i}\frac{\alpha}{2\pi}Q_i^2\Big\{\mathrm{d}\sigma_{\text{Born}}(q_i,\kappa_i)\\ &\quad\times\left(\left[\frac{3}{2}+2\ln\left(\frac{\Delta E}{E_i}\right)\right]\left[1-\ln\left(\frac{4E_i^2}{m_i^2}\frac{\delta_c}{2}\right)\right]+\frac{5}{2}-\frac{2\pi^2}{3}\right)\\ &\qquad+\mathrm{d}\sigma_{\text{Born}}(q_i,-\kappa_i)\frac{1}{2}\Big\}.\end{aligned} \tag{2.50}$$

The parameters δ_s and δ_c govern the splitting of the phase space in the different regions, but the final result does not depend on them. They have to be chosen to be small enough to guarantee that the applied approximations are valid. Therefore, varying these parameters in a certain range and showing invariance of the results can serve as an important check of the calculation.

2.3.2 Dipole subtraction method

The second method we want to describe is the dipole subtraction method, which was first introduced in Ref. [85] for massless QCD and later generalised to massive fermions in Ref. [90]. Since we regulate IR divergencies with particle masses, we follow the description from Refs. [87, 90].

The basic idea of the subtraction method is to subtract an auxiliary function from the integrand that features the same singular behaviour in the soft and collinear limit. The partially integrated auxiliary function will later be added again.

Suppressing flux and colour factors, polarisation projectors and the theta-function related to the phase-space cuts, we write

$$\int\mathrm{d}\sigma_{\text{real}}=\int\mathrm{d}\Phi_4\sum_\lambda|\mathcal{M}_{\text{real}}|^2=\int\mathrm{d}\Phi_4\sum_\lambda\left(|\mathcal{M}_{\text{real}}|^2-|\mathcal{M}_{\text{sub}}|^2\right)+\int\mathrm{d}\Phi_4|\mathcal{M}_{\text{sub}}|^2, \tag{2.51}$$

where we demand

$$|\mathcal{M}_{\text{sub}}|^2 \to \sum_{\lambda} |\mathcal{M}_{\text{real}}|^2 \quad \text{for} \quad k \to 0 \quad \text{or} \quad q_i k \to 0 \quad \text{or} \quad q_a k \to 0, \tag{2.52}$$

with q_a and q_i labelling all the momenta of outgoing and incoming fermions, respectively, and k representing the momentum of the photon.

The subtraction function $\mathcal{M}_{\text{sub}}$ is constructed from ordered pairs ij of charged fermions, where fermion i is called the emitter and fermion j the spectator. Only the kinematics of the emitter lead to singularities. The spectator fermion is used to balance energy-momentum conservation relations when combining the momentum of the photon with the momentum of the emitter. Making the dependence of the subtraction function on the emitter–spectator pair explicit, we can write

$$|\mathcal{M}_{ij,\text{sub}}\left(\Phi_4\right)|^2 = -(-1)^{i+j} Q_i Q_j e^2 \sum_{\tau=\pm} g_{ij,\tau}^{(\text{sub})}\left(q_i, q_j, k\right) |\mathcal{M}_{\text{Born}}(\tilde{\Phi}_{3,ij}, \tau\kappa_i)|^2, \tag{2.53}$$

where κ_i is the helicity of the emitter and, if not stated otherwise, the indices i, j run from $1, \ldots, 4$. The subtraction function $\mathcal{M}_{ij,\text{sub}}$ depends on the whole four-particle phase space, whereas the Born matrix element depends only on the three-particle phase space. Therefore we are required to find a mapping of the four-particle on the three-particle phase space, which is different for each emitter–spectator pair ij. The factorisation theorem for mass singularities governs the behaviour of these mappings, ensuring that the three- and four-particle phase space approach each other in the soft and collinear limit, i.e. the momenta have to fulfil the following conditions:

$$q_i^\mu \overset{k\to 0}{\sim} \tilde{q}_i^\mu, \quad q_j^\mu \overset{k\to 0}{\sim} \tilde{q}_j^\mu, \tag{2.54}$$

and

$$q_i^\mu - k^\mu \overset{kq_i\to 0}{\sim} \tilde{q}_i^\mu, \quad q_j^\mu \overset{kq_i\to 0}{\sim} \tilde{q}_j^\mu, \quad i = 1, 2, \tag{2.55}$$

$$q_i^\mu + k^\mu \overset{kq_i\to 0}{\sim} \tilde{q}_i^\mu, \quad q_j^\mu \overset{kq_i\to 0}{\sim} \tilde{q}_j^\mu, \quad i = 3, 4, \tag{2.56}$$

where we denote the emitter and spectator with the subscripts i and j, respectively. Furthermore, the mapped momenta $\tilde{q}_i$ have to fulfil the mass-shell condition and energy-momentum conservation. In the case of final-state emitter and final-state spectator we use the mapping

$$\tilde{q}_i^\mu = q_i^\mu + k^\mu - \frac{y_{ij}}{1 - y_{ij}} q_j^\mu, \quad \tilde{q}_j^\mu = \frac{1}{1 - y_{ij}} q_j^\mu, \quad \tilde{k}^\mu = k^\mu, \tag{2.57}$$

for an initial-state emitter and final-state spectator we have

$$\tilde{q}_i^\mu = x_{ji} q_i^\mu, \quad \tilde{q}_j^\mu = q_j^\mu + k^\mu - (1 - x_{ji}) q_i^\mu, \quad \tilde{k}^\mu = k^\mu, \tag{2.58}$$

and the case final-state emitter and initial-state spectator can be obtained from Eq. (2.58) by the replacement $i \leftrightarrow j$. In the above cases, all momenta that are not a part of the emitter–spectator pair are unchanged. Finally, for an initial-state emitter and an initial-state spectator one finds

$$\tilde{q}_i^\mu = v_{ij} q_i^\mu, \quad \tilde{q}_j^\mu = q_j^\mu, \quad \tilde{q}_l^\mu = \Lambda_\nu^\mu q_l^\nu, \quad \tilde{k}^\mu = \Lambda_\nu^\mu k^\nu, \quad l = 3,4. \tag{2.59}$$

In the above equations and in the following we use the relations

$$\begin{aligned} x_{ij} &= \frac{q_i q_j + q_j k - q_i k}{q_i q_j + q_j k}, \quad & y_{ij} &= \frac{q_i k}{q_i q_j + q_i k + q_j k}, \\ z_{ij} &= \frac{q_i q_j}{q_i q_j + q_j k}, & v_{ij} &= \frac{q_i q_j - q_j k - q_i k}{q_i q_j}, \end{aligned} \tag{2.60}$$

and the boost matrix Λ_ν^μ is given by

$$\Lambda_\nu^\mu = g_\nu^\mu - \frac{\left(P_{ij} + \tilde{P}_{ij}\right)^\mu \left(P_{ij} + \tilde{P}_{ij}\right)_\nu}{P_{ij}^2 + P_{ij}\tilde{P}_{ij}} + 2\frac{\tilde{P}_{ij}^\mu P_{ij,\nu}}{P_{ij}^2}, \tag{2.61}$$

where

$$\tilde{P}_{ij}^\mu = \tilde{q}_i^\mu + \tilde{q}_j^\mu, \quad P_{ij} = q_i + q_j - k. \tag{2.62}$$

The process-independent radiator functions $g_{ij,\pm}^{(\mathrm{sub})}$ have to mimic the singular behaviour of the real corrections. Therefore, in the soft limit they have to fulfil

$$g_{ij,+}^{(\mathrm{sub})}(q_i, q_j, k) \overset{k\to 0}{\sim} \frac{2(q_i q_j)}{q_i k (q_i k + q_j k)} - \frac{m_i^2}{(q_i k)^2}, \quad g_{ij,-}^{(\mathrm{sub})}(q_i, q_j, k) \overset{k\to 0}{\sim} \mathcal{O}(1), \tag{2.63}$$

and in the collinear limits

$$\begin{aligned} g_{ij,+}^{(\mathrm{sub})}(q_i, q_j, k) &\overset{q_i k\to 0}{\sim} \frac{1}{q_i k}\left[\frac{1}{x_i} P_{ff}(x_i) - \frac{1+x_i^2}{x_i}\frac{m_i^2}{2q_i k}\right], \\ g_{ij,-}^{(\mathrm{sub})}(q_i, q_j, k) &\overset{q_i k\to 0}{\sim} \frac{(1-x_i)^2}{x_i}\frac{m_i^2}{2(q_i k)^2}, \quad x_i = 1 - \frac{k^0}{q_i^0}, \quad i = 1,2, \\ g_{ij,+}^{(\mathrm{sub})}(q_i, q_j, k) &\overset{q_i k\to 0}{\sim} \frac{1}{q_i k}\left[P_{ff}(z_i) - \frac{1+z_i^2}{z_i}\frac{m_i^2}{2q_i k}\right], \\ g_{ij,-}^{(\mathrm{sub})}(q_i, q_j, k) &\overset{q_i k\to 0}{\sim} \frac{(1-z_i)^2}{z_i}\frac{m_i^2}{2(q_i k)^2}, \quad z_i = \frac{q_i^0}{q_i^0 + k^0}, \quad i = 3,4, \end{aligned} \tag{2.64}$$

where $P_{ff}(y)$ is the splitting function defined through

$$P_{ff}(y) = \frac{1+y^2}{1-y}. \tag{2.65}$$

In the massless case, they are explicitly given by

$$\begin{aligned}
g^{(\mathrm{sub})}_{ij,+}(q_i,q_j,k) &= \frac{1}{q_i k\,(1-y_{ij})}\left[\frac{2}{1-z_{ij}\,(1-y_{ij})}-1-z_{ij}\right],\\
g^{(\mathrm{sub})}_{ia,+}(q_i,q_a,k) &= \frac{1}{(q_i k)x_{ia}}\left[\frac{2}{2-x_{ia}-z_{ia}}-1-z_{ia}\right],\\
g^{(\mathrm{sub})}_{ai,+}(q_a,q_i,k) &= \frac{1}{(q_i k)x_{ai}}\left[\frac{2}{2-x_{ai}-z_{ai}}-1-x_{ai}\right],\\
g^{(\mathrm{sub})}_{ab,+}(q_a,q_b,k) &= \frac{1}{(q_b k)v_{ab}}\left[\frac{2}{1-v_{ab}}-1-v_{ab}\right], \qquad (2.66)\\
g^{(\mathrm{sub})}_{ij,-}(q_i,q_j,k) &= g^{(\mathrm{sub})}_{ia,-}(q_i,q_a,k)=g^{(\mathrm{sub})}_{ai,-}(q_a,q_i,k)=g^{(\mathrm{sub})}_{ab,-}(q_a,q_b,k)=0,
\end{aligned}$$

where we denote final-state particles with the letters i,j and initial-state particles with the letters a,b.

The finite part of the real corrections is now obtained through

$$\int \mathrm{d}\sigma^{\mathrm{finite}}_{\mathrm{real}} = \frac{1}{2s}\int \mathrm{d}\Phi_4 \left[\sum_{\lambda}|\mathcal{M}_{\mathrm{real}}|^2\Theta_{\mathrm{cut}}(\Phi_4) - \sum_{\substack{i,j=1\\ i\neq j}}^{4}|\mathcal{M}_{ij,\mathrm{sub}}|^2\Theta_{\mathrm{cut}}(\tilde{\Phi}_{3,ij})\right]. \qquad (2.67)$$

When applying cuts on the final-state particles, we have to make sure that we apply a four-particle cut routine to the real corrections, and the corresponding three-particle cut routine to the subtraction function, which we denote here with $\Theta_{\mathrm{cut}}(\Phi_4)$ and $\Theta_{\mathrm{cut}}(\tilde{\Phi}_{3,ij})$ respectively.

We turn now to the treatment of the singular contributions. Splitting the four-particle phase space into a three-particle phase space and the photonic part

$$\int \mathrm{d}\Phi_4 = \int_0^1 \mathrm{d}x \int \mathrm{d}\tilde{\Phi}_{3,ij}(x)\int \mathrm{d}\Phi_{\gamma,ij}, \qquad (2.68)$$

where the photonic part of the phase space $\mathrm{d}\Phi_{\gamma,ij}$ depends on the mass regulators m_i and m_γ of the fermions and of the photon, we have to compensate for the reduction of the CM energy in the case of ISR radiation, which is indicated by the x-dependence of the three-particle phase space. We can then write the singular part of the real corrections as

$$\begin{aligned}
\int \mathrm{d}\sigma^{\mathrm{sing}}_{\mathrm{real}} &= -\frac{\alpha}{2\pi}\sum_{\substack{i,j=1\\ i\neq j}}^{4}\sum_{\tau=\pm}(-1)^{i+j}Q_iQ_j\\
&\quad\times\int_0^1 \mathrm{d}x\int \mathrm{d}\tilde{\Phi}_{3,ij}(x)\mathcal{G}^{\mathrm{sub}}_{ij,\tau}(\tilde{s}_{ij},x)\frac{1}{2xs}|\mathcal{M}_{\mathrm{Born}}(\tilde{\Phi}_{3,ij},\tau\kappa_i)|^2\Theta_{\mathrm{cut}}(\tilde{\Phi}_{3,ij}), \qquad (2.69)
\end{aligned}$$

where the functions $\mathcal{G}^{\rm sub}_{ij,\tau}(\tilde{s}_{ij},x)$ are given by the analytic integration over the photonic part of the phase space of the radiator functions

$$\mathcal{G}^{\rm sub}_{ij,\tau}(\tilde{s}_{ij},x) = 8\pi^2 \int {\rm d}\Phi_{\gamma,ij} x g^{\rm (sub)}_{ij,\tau}\left(q_i,q_j,k\right), \tag{2.70}$$

and $\tilde{s}_{ij} = 2\tilde{q}_i\tilde{q}_j$. They read

$$\begin{aligned}
\mathcal{G}^{\rm sub}_{ij,+}(\tilde{s}_{ij},x) &= \delta(1-x)\left[\mathcal{L}\left(\tilde{s}_{ij},m_i^2\right) - \frac{\pi^2}{3} + 1\right], \\
\mathcal{G}^{\rm sub}_{ij,-}(\tilde{s}_{ij},x) &= \frac{\delta(1-x)}{2}, \\
\mathcal{G}^{\rm sub}_{ia,+}(\tilde{s}_{ia},x) &= \frac{1}{1-x}\left[2\ln\left(\frac{2-x}{1-x}\right) - \frac{3}{2}\right], \\
\mathcal{G}^{\rm sub}_{ia,-}(\tilde{s}_{ia},x) &= 0, \\
\mathcal{G}^{\rm sub}_{ai,+}(\tilde{s}_{ai},x) &= P_{ff}(x)\left[\ln\left(\frac{|\tilde{s}_{ai}|}{m_a^2 x}\right) - 1\right] - \frac{2}{1-x}\ln(2-x) + (1+x)\ln(1-x), \\
\mathcal{G}^{\rm sub}_{ai,-}(\tilde{s}_{ai},x) &= 1-x, \\
\mathcal{G}^{\rm sub}_{ab,+}(\tilde{s}_{ab},x) &= P_{ff}(x)\left[\ln\left(\frac{s}{m_a^2}\right) - 1\right], \\
\mathcal{G}^{\rm sub}_{ab,-}(\tilde{s}_{ab},x) &= 1-x,
\end{aligned} \tag{2.71}$$

where

$$\mathcal{L}\left(\tilde{s}_{ij},m_i^2\right) = \ln\left(\frac{m_\gamma^2}{\tilde{s}_{ij}}\right)\left[1 + \ln\left(\frac{m_i^2}{\tilde{s}_{ij}}\right) - \frac{1}{2}\ln^2\left(\frac{m_i^2}{\tilde{s}_{ij}}\right) + \frac{1}{2}\ln\left(\frac{m_i^2}{\tilde{s}_{ij}}\right)\right], \tag{2.72}$$

and $\tilde{s}_{ia} = 2\tilde{q}_i\tilde{q}_a$, $\tilde{s}_{ai} = 2\tilde{q}_a\tilde{q}_i$, and $\tilde{s}_{ab} = 2\tilde{q}_a\tilde{q}_b$. The distributions defined in Eq. (2.71) become singular in the limit $x \to 1$, and the corresponding integrals are therefore not suited for numerical integration yet. In the next step, we isolate the singularities, using the usual $[\ldots]_+$ prescription

$$\int_0^1 {\rm d}x \left[f(x)\right]_+ g(x) = \int_0^1 {\rm d}x f(x)\left[g(x) - g(1)\right]. \tag{2.73}$$

This leads us to

$$\begin{aligned}
\int {\rm d}\sigma^{\rm sing}_{\rm real} &= -\frac{\alpha}{4\pi s}\sum_{\substack{i,j=1\\ i\neq j}}^{4}\sum_{\tau=\pm}(-1)^{i+j}Q_iQ_j\Big\{ \\
&\quad \int_0^1 \frac{{\rm d}x}{x}\int {\rm d}\tilde{\Phi}_{3,ij}(x)\left[\mathcal{G}^{\rm sub}_{ij,\tau}(\tilde{s}_{ij},x)\right]_+ |\mathcal{M}_{\rm Born}(\tilde{\Phi}_{3,ij},\tau\kappa_i)|^2\Theta_{\rm cut}(\tilde{\Phi}_{3,ij}) \\
&+ \int {\rm d}\Phi_3 G^{\rm sub}_{ij,\tau}(\tilde{s}_{ij})|\mathcal{M}_{\rm Born}(\Phi_3,\tau\kappa_i)|^2\Big\}\Theta_{\rm cut}(\Phi_3),
\end{aligned} \tag{2.74}$$

where

$$
\begin{aligned}
G^{\text{sub}}_{ij,+}(\tilde{s}_{ij}) &= \mathcal{L}\left(\tilde{s}_{ij}, m_i^2\right) - \frac{\pi^2}{3} + 1, & G^{\text{sub}}_{ij,-}(\tilde{s}_{ij}) &= \frac{1}{2},\\
G^{\text{sub}}_{ia,+}(\tilde{s}_{ia}) &= \mathcal{L}\left(|\tilde{s}_{ia}|, m_i^2\right) - \frac{\pi^2}{2} + 1, & G^{\text{sub}}_{ia,-}(\tilde{s}_{ia}) &= \frac{1}{2},\\
G^{\text{sub}}_{ai,+}(\tilde{s}_{ai}) &= \mathcal{L}\left(|\tilde{s}_{ai}|, m_i^2\right) + \frac{\pi^2}{6} - \frac{3}{2}, & G^{\text{sub}}_{ai,-}(\tilde{s}_{ai}) &= \frac{1}{2},\\
G^{\text{sub}}_{ab,+}(\tilde{s}_{ab}) &= \mathcal{L}\left(s, m_i^2\right) - \frac{\pi^2}{3} + \frac{3}{2}, & G^{\text{sub}}_{ab,-}(\tilde{s}_{ab}) &= \frac{1}{2}.
\end{aligned}
\tag{2.75}
$$

We have now isolated the singular contribution of the real corrections, which is controlled analytically and can be combined with the corresponding singular contribution from the virtual corrections.

2.3.3 Non-collinear-safe phase-space slicing

In this section we discuss how the cut on the photon energy affects the slicing procedure. As we see from Eq. (2.37), imposing an upper cut on the photon energy does not affect the singularity structure of the first and third term since the finite part does not contain any divergencies and the cut acts outside the soft region. The hard-photon cut affects only hadronic final states, i.e. photons inside jets. Since we consider electron–positron collisions, we only have to consider collinear final-state radiation. In Section 2.3.1 we parametrised the collinear region in terms of the energy fraction z carried by the (anti-)quark that resulted from the splitting. The experimental cut however is a cut on the energy fraction of the photon after the splitting. We therefore need the complementary cut on the quark energy fraction $z_q > z'_{\text{cut}} = 1 - z_{\text{cut}}$. In this notation the limits $z_q \to 1$ and $z_q \to 0$ describe a soft and a hard photon respectively. Eq. (2.48) is then given by

$$
\begin{aligned}
\mathrm{d}\sigma^{\text{final}}_{\text{coll.}}(z'_{\text{cut}}) = &\sum_{i=3}^{4}\sum_{\kappa_i}\frac{\alpha}{2\pi}Q_i^2\mathrm{d}\sigma_{\text{Born}}(q_i,\kappa_i)\Bigg\{\int_{z'_{\text{cut}}}^{1-\Delta E/E_i}\mathrm{d}z_i P_{qq}(z_i)\left[\ln\left(\frac{4E_i^2\delta_c}{2m_i^2}z_i^2\right)-1\right]\\
&+\mathrm{d}\sigma_{\text{Born}}(q_i,-\kappa_i)\int_{z'_{\text{cut}}}^{1}(1-z_i)\Bigg\}\\
=&\sum_{i=3}^{4}\frac{\alpha}{2\pi}Q_i^2\Bigg\{\mathrm{d}\sigma_{\text{Born}}(q_i)\left[\frac{9}{2}-4z'_{\text{cut}}-\frac{z'^2_{\text{cut}}}{2}+\left(2z'_{\text{cut}}+z'^2_{\text{cut}}\right)\ln\left(z'_{\text{cut}}\right)\right.\\
&+\left(-\frac{3}{2}+z'_{\text{cut}}+\frac{1}{2}z'^2_{\text{cut}}-2\ln\left(\frac{\Delta E/E_i}{1-z'_{\text{cut}}}\right)\right)\ln\left(\frac{4E_i^2\delta_c}{2m_i^2}\right)-\frac{2\pi^2}{3}\\
&\left.+2\ln\left(\frac{\Delta E/E_i}{1-z'_{\text{cut}}}\right)+4\ln\left(1-z'_{\text{cut}}\right)\ln\left(z'_{\text{cut}}\right)+4\mathrm{Li}_2\left(z'_{\text{cut}}\right)\right].
\end{aligned}
\tag{2.76}
$$

In Eq. (2.76) we performed the polarisation sum, since the polarisation of final-state hadrons in jets cannot be measured. In terms of the cut on the photon energy, i.e. performing the replacement $z'_{\text{cut}} \to 1 - z_{\text{cut}}$ in Eq. (2.76), we find

$$\begin{aligned}\mathrm{d}\sigma^{\text{final}}_{\text{coll.}}(z_{\text{cut}}) = \sum_{i=3}^{4} \frac{\alpha}{2\pi} Q_i^2 \Bigg\{ \mathrm{d}\sigma_{\text{Born}}(q_i) \Bigg[&-\frac{2\pi^2}{3} + 5z_{\text{cut}} - \frac{z_{\text{cut}}^2}{2} + 2\ln\left(\frac{\Delta E/E_i}{z_{\text{cut}}}\right) \\ &+ \left(-2z_{\text{cut}} + \frac{z_{\text{cut}}^2}{2} - 2\ln\left(\frac{\Delta E/E_i}{z_{\text{cut}}}\right)\right) \ln\left(\frac{4E_i^2\delta_c}{2m_i^2}\right) + 4\mathrm{Li}_2\left(1 - z_{\text{cut}}\right) \\ &+ 2\left(\frac{3}{2} - 2z_{\text{cut}} + \frac{1}{2}z_{\text{cut}}^2 + 2\ln\left(z_{\text{cut}}\right)\right) \ln\left(1 - z_{\text{cut}}\right)) \Bigg] . \end{aligned} \tag{2.77}$$

In Eq. (2.77) we have the original dependence on the slicing parameters and the mass regulators, already present in Eq. (2.50), plus an additional term that depends on the slicing parameters, the mass regulators, and the cut on the photon energy. It is exactly this term which gives rise to left-over singularities.

2.3.4 Non-collinear-safe subtraction method

Recently there has been a proposal of how to deal with non-collinear safe observables using the subtraction method [91]. The difference to the subtraction method described in Section 2.3.2 lies in the derivation of the integrated radiator functions. Here one can no longer rely on the fact that for each photon radiation cone around a charged particle, the fraction of the charged particle's energy is fully integrated over, but that the cut procedure affects the range of integration in the collinear cones. The affected variables are the z_{ij} defined in Eq. (2.60), and the variables z_{ia} defined analogously.

In the following we describe the approach given in Ref. [91] and how we use it in our calculation. In particular we describe the procedure for final-state emitter final-state spectator and final-state-emitter initial-state spectator pairs. Again, we can disregard the contributions from initial-state emitters since we consider leptonic initial states that are not affected by the hard-photon cut.

Final-state emitter and final-state spectator

The integration of the radiator functions for a final-state emitter i and a final-state spectator j is of the form

$$G^{\text{sub}}_{ij,\tau}(\tilde{s}_{ij}) \sim \int_{y_1}^{y_2} \mathrm{d}y_{ij}(1 - y_{ij}) \int_{z_1(y_{ij})}^{z_2(y_{ij})} \mathrm{d}z_{ij} g^{(\text{sub})}_{ij,\tau}(q_i, q_j, k), \tag{2.78}$$

where y_{ij} and z_{ij} are given in Eq. (2.60), and the limits of integration depend on invariants built from emitter, spectator, and photon momenta and masses. The explicit

integration leads to the results given in Eq. (2.75). If we now want to use information on the photon momentum in the collinear cone, we have to interchange the integrations in Eq. (2.78) and leave the integration over z_{ij} open. Alas, we consider

$$\bar{\mathcal{G}}^{\rm sub}_{ij,\tau}(\tilde{s}_{ij},z_{ij}) \sim \int_{y_1(z_{ij})}^{y_2(z_{ij})} {\rm d}y_{ij}(1-y_{ij}) g^{\rm (sub)}_{ij,\tau}(q_i,q_j,k). \tag{2.79}$$

We split off the soft singularity contained in Eq. (2.79) by employing the well-known $[\ldots]_+$ distribution

$$\bar{\mathcal{G}}^{\rm sub}_{ij,\tau}(\tilde{s}_{ij},z) = G^{\rm sub}_{ij,\tau}(\tilde{s}_{ij})\delta(1-z) + \left[\bar{\mathcal{G}}^{\rm sub}_{ij,\tau}(\tilde{s}_{ij},z)\right]_+, \tag{2.80}$$

where the quantity $G^{\rm sub}_{ij,\tau}(\tilde{s}_{ij})$ contains the soft singularity [see Eq. (2.75)]. For vanishing fermion masses, the integral in Eq. (2.79) can be carried out explicitly (for details of the derivation see Ref. [91]), resulting in

$$\begin{aligned}
\bar{\mathcal{G}}^{\rm sub}_{ij,+}(\tilde{s}_{ij},z) &= P_{ff}(z)\left[\ln\left(\frac{\tilde{s}_{ij}z}{m_i^2}\right)-1\right] + (1+z)\ln(1-z), \\
\bar{\mathcal{G}}^{\rm sub}_{ij,-}(\tilde{s}_{ij},z) &= 1-z.
\end{aligned} \tag{2.81}$$

We can now give the explicit form of the ij contribution $|\mathcal{M}_{{\rm sub},ij}(\Phi_1)|^2$, which is

$$\begin{aligned}
\int {\rm d}\Phi_1 |\mathcal{M}_{{\rm sub},ij}(\Phi_1;\kappa_i)|^2 &= -\frac{\alpha}{2\pi} Q_i\sigma_i Q_j\sigma_j \int {\rm d}\tilde{\Phi}_{0,ij} \int_0^1 {\rm d}z \\
&\quad \times \left\{ G^{\rm sub}_{ij,\tau}(\tilde{s}_{ij})\,\delta(1-z) + \left[\bar{\mathcal{G}}^{\rm sub}_{ij,\tau}(\tilde{s}_{ij},z)\right]_+ \right\} \\
&\quad \times |\mathcal{M}_0(\tilde{q}_i,\tilde{q}_j;\tau\kappa_i)|^2 \Theta_{\rm cut}(q_i = z\tilde{q}_i, k=(1-z)\tilde{q}_i,\tilde{q}_j,\{k_n\}).
\end{aligned} \tag{2.82}$$

The term in curly brackets in Eq. (2.82) consists of a term proportional to a delta-function in z, which is the usual endpoint contribution, and a $[\ldots]_+$ prescription, acting only on $\Theta_{\rm cut}$. In our case $\Theta_{\rm cut}$ just provides a lower cut-off on the z-integration, and we find

$$\begin{aligned}
\int {\rm d}\Phi_1 |\mathcal{M}_{{\rm sub},ij}(\Phi_1;\kappa_i)|^2 &= -\frac{\alpha}{2\pi} Q_i\sigma_i Q_j\sigma_j \int {\rm d}\tilde{\Phi}_{0,ij} |\mathcal{M}_0(\tilde{q}_i,\tilde{q}_j;\tau\kappa_i)|^2 \Big\{ G^{\rm sub}_{ij,\tau}(\tilde{s}_{ij}) \\
&\quad + \int_0^1 {\rm d}z\; \bar{\mathcal{G}}^{\rm sub}_{ij,\tau}(\tilde{s}_{ij},z)\left[\Theta(z-z'_{\rm cut}) - \Theta(1-z'_{\rm cut})\right] \Big\} \\
&= -\frac{\alpha}{2\pi} Q_i\sigma_i Q_j\sigma_j \int {\rm d}\tilde{\Phi}_{0,ij} |\mathcal{M}_0(\tilde{q}_i,\tilde{q}_j;\tau\kappa_i)|^2 \Big\{ G^{\rm sub}_{ij,\tau}(\tilde{s}_{ij}) \\
&\quad - \int_0^{z'_{\rm cut}} {\rm d}z\; \bar{\mathcal{G}}^{\rm sub}_{ij,\tau}(\tilde{s}_{ij},z) \Big\}.
\end{aligned} \tag{2.83}$$

The z-integration in the second term of Eq. (2.83) as well as the polarisation sum can be performed, yielding

$$\begin{aligned}\sum_{\tau=\pm}\int_0^{z'_{\rm cut}} \mathrm{d}z\ \bar{\mathcal{G}}^{\rm sub}_{ij,\tau}(\tilde{s}_{ij},z) &= \int_0^{z'_{\rm cut}} \mathrm{d}z\ \left[\frac{1+z^2}{1-z}\ln\left(\frac{\tilde{s}_{ij}z}{m_i^2}\right) - \frac{2z}{1-z} + (1+z)\ln(1-z)\right] \\ &= -\frac{\pi^2}{3} + \left[\frac{1}{2} - 2\ln\left(\frac{\tilde{s}_{ij}}{m_i^2}\right)\right]\ln(1-z'_{\rm cut}) \\ &\quad + z'_{\rm cut}\left[\frac{3}{2} - \ln\left(\frac{\tilde{s}_{ij}}{m_i^2}\frac{z'_{\rm cut}}{1-z'_{\rm cut}}\right)\right] \\ &\quad - \frac{z'^2_{\rm cut}}{2}\ln\left(\frac{\tilde{s}_{ij}}{m_i^2}\frac{z'_{\rm cut}}{1-z'_{\rm cut}}\right) + 2\,\mathrm{Li}_2(1-z'_{\rm cut})\,. \end{aligned} \tag{2.84}$$

Final-state emitter and initial-state spectator

In the case of a final-state emitter i and an initial-state spectator j, the integration of $|\mathcal{M}_{(\rm sub),ia}|^2$ over $x = x_{ia}$ is performed using a $[\ldots]_+$ prescription

$$\begin{aligned}&\frac{-\bar{P}^2_{ia}}{2}\int_0^{x_1}\mathrm{d}x_{ia}\int_{z_1(x_{ia})}^{z_2(x_{ia})}\mathrm{d}z_{ia}\, g^{(\rm sub)}_{ia,\tau}(q_i,q_a,k)\ldots \\ &= \int_0^1 \mathrm{d}x\left\{G^{\rm sub}_{ia,\tau}(\tilde{s}_{ia})\delta(1-x) + \left[\mathcal{G}^{\rm sub}_{ia,\tau}(\tilde{s}_{ia},x)\right]_+\right\}\ldots, \end{aligned} \tag{2.85}$$

where $\bar{P}^2_{ia} = (q_i+k-q_j)^2 - m_a^2 - m_i^2 - m_\gamma^2$ and the ellipses stand for x-dependent functions like the Born matrix element squared or flux factors. The integration over x is usually done numerically. The upper limit of the integration x_1 could be replaced by 1, since all the soft and collinear singular terms are contained in $G^{\rm sub}_{ia,\tau}(\tilde{s}_{ia})$.

In a non-collinear-safe set-up, the ellipses also represent terms like the cut routine, which are specifically z_{ia} dependent. Therefore the whole integration has to be done numerically. To this end, a procedure has to be found, that can isolate the occurring singularities in the endpoint. To begin with, we generalise the $[\ldots]_+$ prescription to multiple variables. We denote the usual $[\ldots]_+$ prescription in an n-dimensional integral over the variables r_i, $i = 1,\cdots,n$, by

$$\int \mathrm{d}^n\mathbf{r}\,[g(\mathbf{r})]^{(r_i)}_{+,(a)}\,f(\mathbf{r}) \equiv \int \mathrm{d}^n\mathbf{r} g(\mathbf{r})\left(f(\mathbf{r}) - f(\mathbf{r})|_{r_i=a}\right). \tag{2.86}$$

Iterating this procedure, we define

$$\begin{aligned}\int \mathrm{d}^n\mathbf{r}\,[g(\mathbf{r})]^{(r_i,r_j)}_{+,(a,b)}\,f(\mathbf{r}) &\equiv \int \mathrm{d}^n\mathbf{r}\left[[g(\mathbf{r})]^{(r_i)}_{+,(a)}\right]^{(r_j)}_{+,(b)} f(\mathbf{r}) \\ &= \int \mathrm{d}^n\mathbf{r} g(\mathbf{r})\left(f(\mathbf{r}) - f(\mathbf{r})|_{r_i=a} - f(\mathbf{r})|_{r_j=b} + f(\mathbf{r})|^{r_i=a}_{r_j=b}\right). \end{aligned} \tag{2.87}$$

To recover the usual notation, we drop the subscripts a and/or b if they are equal to one. Defining the auxiliary integral

$$I[f] \equiv \frac{-\bar{P}_{ia}^2}{2} \int_0^{x_1} \mathrm{d}x_{ia} \int_{z_1(x_{ia})}^{z_2(x_{ia})} \mathrm{d}z_{ia} g_{ia,\tau}^{(\mathrm{sub})}(x,z) f(x,z), \tag{2.88}$$

one finds for infinitesimal mass parameters m_a^2, m_i^2, and m_γ^2 ($x_1, z_1 \to 1, z_2 \to 0$),

$$\begin{aligned} I[f] &= \frac{-\bar{P}_{ia}^2}{2} \left\{ \int_0^1 \mathrm{d}x \int_0^1 \mathrm{d}z \left[\bar{g}_{ia,\tau}^{(\mathrm{sub})}(x,z) \right]_+^{(x,z)} f(x,z) + \int_0^1 \mathrm{d}x f(x,1) \left[\mathcal{G}_{ia,\tau}^{(\mathrm{sub})}(\tilde{s}_{ia},x) \right]_+ \right. \\ &+ \left. \int_0^1 \mathrm{d}z f(1,z) \left[\bar{\mathcal{G}}_{ia,\tau}^{(\mathrm{sub})}(\tilde{s}_{ia},z) \right]_+ + f(1,1) G_{ia,\tau}^{(\mathrm{sub})}(\tilde{s}_{ia}) \right\}, \end{aligned} \tag{2.89}$$

where

$$\begin{aligned} \bar{g}_{ia,+}^{(\mathrm{sub})}(x,z) &= \frac{1}{1-x} \left(\frac{2}{2-x-z} - 1 - z \right), \quad \bar{g}_{ia,-}^{(\mathrm{sub})}(x,z) = 0, \\ \bar{\mathcal{G}}_{ia,+}^{(\mathrm{sub})}(\tilde{s}_{ia},z) &= P_{ff}(z) \left[\ln\left(\frac{|\tilde{s}_{ia}|z}{m_i^2} \right) - 1 \right] - \frac{2\ln(2-z)}{1-z} + (1+z)\ln(1-z), \\ \bar{\mathcal{G}}_{ia,-}^{(\mathrm{sub})}(\tilde{s}_{ia},z) &= 1 - z. \end{aligned} \tag{2.90}$$

Now, the explicit form of the ia contribution $|\mathcal{M}_{\mathrm{sub},ia}(\Phi_1)|^2$ reads

$$\begin{aligned} &\int \mathrm{d}\Phi_1 |\mathcal{M}_{\mathrm{sub},ia}(\Phi_1;\kappa_i)|^2 = -\frac{\alpha}{2\pi} Q_a \sigma_a Q_i \sigma_i \int_0^1 \mathrm{d}x \int \mathrm{d}\tilde{\Phi}_{0,ia}(\tilde{s}_{ia},x) \int_0^1 \mathrm{d}z \\ &\times \Theta_{\mathrm{cut}}(q_i = z\tilde{q}_i(x), k = (1-z)\tilde{q}_i(x), \{k_n(x)\}) \\ &\times \frac{1}{x} \left\{ G_{ia,\tau}^{\mathrm{sub}}(\tilde{s}_{ia}) \delta(1-x)\delta(1-z) + \left[\mathcal{G}_{ia,\tau}^{\mathrm{sub}}(\tilde{s}_{ia},x) \right]_+ \delta(1-z) \right. \\ &\quad \left. + \left[\bar{\mathcal{G}}_{ia,\tau}^{\mathrm{sub}}(\tilde{s}_{ia},z) \right]_+ \delta(1-x) + \left[\bar{g}_{ia,\tau}^{\mathrm{sub}}(x,z) \right]_+^{x,z} \right\} |\mathcal{M}_0(\tilde{q}_i(x), \tilde{q}_a(x); \tau\kappa_i)|^2. \end{aligned} \tag{2.91}$$

We exploit again the simplicity of the Θ_{cut}-function in our case and find

$$\int \mathrm{d}\Phi_1 |\mathcal{M}_{\mathrm{sub},ia}(\Phi_1;\kappa_i)|^2 = -\frac{\alpha}{2\pi} Q_a \sigma_a Q_i \sigma_i \Big\{$$

$$
\begin{aligned}
&\int \mathrm{d}\tilde{\Phi}_{0,ia}\left(\tilde{s}_{ia},1\right) G^{\mathrm{sub}}_{ia,\tau}\left(\tilde{s}_{ia}\right) \left|\mathcal{M}_0\left(\tilde{q}_i(1),\tilde{q}_a(1);\tau\kappa_i\right)\right|^2 \\
&+\int_0^1 \mathrm{d}x \int \mathrm{d}\tilde{\Phi}_{0,ia}\left(\tilde{s}_{ia},x\right) \frac{1}{x}\left[\mathcal{G}^{\mathrm{sub}}_{ia,\tau}\left(\tilde{s}_{ia},x\right)\right]_+ \left|\mathcal{M}_0\left(\tilde{q}_i(x),\tilde{q}_a(x);\tau\kappa_i\right)\right|^2 \\
&+\int \mathrm{d}\tilde{\Phi}_{0,ia}\left(\tilde{s}_{ia},1\right) \int_0^1 \mathrm{d}z \left[\bar{\mathcal{G}}^{\mathrm{sub}}_{ia,\tau}\left(\tilde{s}_{ia},z\right)\right]_+ \Theta\left(z-z'_{\mathrm{cut}}\right) \left|\mathcal{M}_0\left(\tilde{q}_i(1),\tilde{q}_a(1);\tau\kappa_i\right)\right|^2 \\
&+\int_0^1 \mathrm{d}x \int \mathrm{d}\tilde{\Phi}_{0,ia}\left(\tilde{s}_{ia},x\right) \int_0^1 \mathrm{d}z \frac{1}{x}\left[\bar{g}^{\mathrm{sub}}_{ia,\tau}\left(x,z\right)\right]^x_+ \left|\mathcal{M}_0\left(\tilde{q}_i(x),\tilde{q}_a(x);\tau\kappa_i\right)\right|^2 \\
&\qquad\qquad \times\left(\Theta_{\mathrm{cut}}\left(z-z'_{\mathrm{cut}}\right)-\Theta_{\mathrm{cut}}\left(1-z'_{\mathrm{cut}}\right)\right)\Big\} \\
= \quad & -\frac{\alpha}{2\pi} Q_a\sigma_a Q_i\sigma_i \Big\{ \int \mathrm{d}\tilde{\Phi}_{0,ia}\left(\tilde{s}_{ia},1\right) G^{\mathrm{sub}}_{ia,\tau}\left(\tilde{s}_{ia}\right) \left|\mathcal{M}_0\left(\tilde{q}_i(1),\tilde{q}_a(1);\tau\kappa_i\right)\right|^2 \\
&+\int_0^1 \mathrm{d}x \int \mathrm{d}\tilde{\Phi}_{0,ia}\left(\tilde{s}_{ia},x\right) \frac{1}{x}\left[\mathcal{G}^{\mathrm{sub}}_{ia,\tau}\left(\tilde{s}_{ia},x\right)\right]_+ \left|\mathcal{M}_0\left(\tilde{q}_i(x),\tilde{q}_a(x);\tau\kappa_i\right)\right|^2 \\
&-\int \mathrm{d}\tilde{\Phi}_{0,ia}\left(\tilde{s}_{ia},1\right) \int_0^{z'_{\mathrm{cut}}} \mathrm{d}z \bar{\mathcal{G}}^{\mathrm{sub}}_{ia,\tau}\left(\tilde{s}_{ia},z\right) \left|\mathcal{M}_0\left(\tilde{q}_i(1),\tilde{q}_a(1);\tau\kappa_i\right)\right|^2 \\
&-\int_0^1 \mathrm{d}x \int \mathrm{d}\tilde{\Phi}_{0,ia}\left(\tilde{s}_{ia},x\right) \int_0^{z'_{\mathrm{cut}}} \mathrm{d}z \frac{1}{x}\left[\bar{g}^{\mathrm{sub}}_{ia,\tau}\left(x,z\right)\right]^x_+ \left|\mathcal{M}_0\left(\tilde{q}_i(x),\tilde{q}_a(x);\tau\kappa_i\right)\right|^2 \Big\} \\
= \quad & -\frac{\alpha}{2\pi} Q_a\sigma_a Q_i\sigma_i \Big\{ \\
&\int \mathrm{d}\tilde{\Phi}_{0,ia}\left(\tilde{s}_{ia}\right) \left(G^{\mathrm{sub}}_{ia,\tau}\left(\tilde{s}_{ia}\right) - \int_0^{z'_{\mathrm{cut}}} \mathrm{d}z \bar{\mathcal{G}}^{\mathrm{sub}}_{ia,\tau}\left(\tilde{s}_{ia},z\right)\right) \left|\mathcal{M}_0\left(\tilde{q}_i,\tilde{q}_a;\tau\kappa_i\right)\right|^2 \\
&+\int_0^1 \mathrm{d}x \int \mathrm{d}\tilde{\Phi}_{0,ia}\left(\tilde{s}_{ia},x\right) \frac{1}{x}\left[\mathcal{G}^{\mathrm{sub}}_{ia,\tau}\left(\tilde{s}_{ia},x\right) - \int_0^{z'_{\mathrm{cut}}} \mathrm{d}z \bar{g}^{\mathrm{sub}}_{ia,\tau}\left(x,z\right)\right]_+ \\
&\qquad\qquad \times \left|\mathcal{M}_0\left(\tilde{q}_i(x),\tilde{q}_a(x);\tau\kappa_i\right)\right|^2 \Big\}. \qquad (2.92)
\end{aligned}
$$

The z-integrations and the polarisation sum can again be performed, resulting in

$$
\begin{aligned}
\sum_\tau \int_0^{z'_{\mathrm{cut}}} \mathrm{d}z\ \bar{\mathcal{G}}^{\mathrm{sub}}_{ia,\tau}\left(\tilde{s}_{ia},z\right) &= \int_0^{z'_{\mathrm{cut}}} \mathrm{d}z \left\{ \frac{1+z^2}{1-z} \ln\left(\frac{|\tilde{s}_{ia}|z}{m_i^2}\right) - \frac{2z}{1-z} \right. \\
&\qquad \left. - \frac{2\ln\left(2-z\right)}{1-z} + \left(1+z\right)\ln\left(1-z\right) \right\} \\
&= -\frac{\pi^2}{2} + \left[\frac{1}{2} - 2\ln\left(\frac{|\tilde{s}_{ia}|}{m_i^2}\right)\right] \ln\left(1-z'_{\mathrm{cut}}\right) \\
&\quad + z'_{\mathrm{cut}} \left[\frac{3}{2} - \ln\left(\frac{|\tilde{s}_{ia}|}{m_i^2}\frac{z'_{\mathrm{cut}}}{1-z'_{\mathrm{cut}}}\right)\right] - 2\,\mathrm{Li}_2\left(-1+z'_{\mathrm{cut}}\right)
\end{aligned}
$$

$$- \frac{z_{\rm cut}'^2}{2} \ln\left(\frac{|\tilde{s}_{ia}|}{m_i^2}\frac{z'_{\rm cut}}{1-z'_{\rm cut}}\right) + 2\,{\rm Li}_2\,(1-z'_{\rm cut})\,, \qquad (2.93)$$

and

$$\begin{aligned}\sum_\tau \int_0^{z'_{\rm cut}} {\rm d}z\ \bar{g}^{\rm sub}_{ia,\tau}\,(x,z) &= \int_0^{z'_{\rm cut}} {\rm d}z \frac{1}{1-x}\left(\frac{2}{2-x-z} - 1 - z\right) \\ &= \frac{1}{1-x}\left(-z'_{\rm cut} - \frac{z_{\rm cut}'^2}{2} + \ln\left(\frac{2-x}{2-x-z'_{\rm cut}}\right)\right). \qquad (2.94)\end{aligned}$$

2.3.5 The quark-to-photon fragmentation function

In the previous sections we described how we can deal with identified particles in the final state that lead to non-infrared-safe observables using phase-space slicing and the subtraction method. To restore infrared safety it is common practise to factorise the resulting left-over singularities into an experimentally determined fragmentation function, in our case the quark-to-photon fragmentation function.

In this section we discuss how the quark-to-photon fragmentation function can theoretically be defined using dimensional regularisation and one-cutoff slicing, and can experimentally be measured following the approach given in Ref. [92]. To be able to use the results obtained in this way in the calculation at hand, we repeat the analysis in mass regularisation and two-cutoff slicing that are used throughout the previous sections.

In Ref. [92] a method has been proposed in how to measure the quark-to-photon fragmentation function, i.e. the probability of a quark splitting into a quark and a photon, using the $\mathrm{e^+e^-} \to n\,\mathrm{jet} + \mathrm{photon}$ cross section. The key feature of the proposed method is the democratic clustering of both hadrons and photons into jets, where one keeps track of the fraction z of photonic energy in the jet. This treatment of the photon in the jet enhances the non-perturbative part of the quark-to-photon fragmentation function [92, 93], which in turn can be measured using $\mathrm{e^+e^-}$ annihilations.

To set the stage, we write the lowest-order $\mathrm{e^+e^-} \to n\,\mathrm{jet} + \mathrm{photon}$ cross section as

$$\mathrm{d}\sigma^{\rm LO}(n\,\mathrm{jets} + \gamma) = \Theta\,\mathrm{d}\hat{\sigma}_0(np + \gamma), \qquad (2.95)$$

where $\mathrm{d}\hat{\sigma}_0(np+\gamma)$ is the n parton plus photon cross section in leading order, and Θ represents the cut and photon isolation procedure. Going to next-to-leading order and including both virtual and real corrections we have

$$\begin{aligned}\mathrm{d}\sigma^{\rm NLO}(n\,\mathrm{jets} + \gamma) &= \Theta\left\{\mathrm{d}\hat{\sigma}_1(np+\gamma) + \int \mathrm{d}\hat{\sigma}_0((n+1)p+\gamma)\right. \\ &+ \left.\sum_q \mathrm{d}\hat{\sigma}_0((n+1)p)\mathrm{d}z\,\mathrm{d}E_\gamma\,\delta(E_\gamma - zE_q)D_{q\to\gamma}(z)\right\}, \qquad (2.96)\end{aligned}$$

where the first term represents the one-loop virtual corrections to the n parton plus photon cross section and the second term describes the tree-level emission of an additional parton. The third term comes from the lowest-order $(n+1)$ parton process, where one of the partons fragments into a photon, transferring a fraction z of the parent momentum to the quark (note the change $z \to 1-z$ with respect to Ref. [92]). The sum runs over all partons and each quark contributes according to the quark-to-photon fragmentation function $D_{q\to\gamma}$. The integration over the phase space in the second term in Eq. (2.96) leads to IR singularities related to soft and collinear gluon emission, which cancel the corresponding singularities in the first term, as well as singularities related to collinear photon emission, which cancel the corresponding singularities in the quark-to-photon fragmentation function $D_{q\to\gamma}$. These cancellations ensure that $\mathrm{d}\sigma^{\mathrm{NLO}}(n\,\mathrm{jets}+\gamma)$ is infrared-safe and therefore a well-defined physical quantity.

Since fragmentation is a long-distance process, it cannot be calculated entirely in perturbation theory. Theoretically $D_{q\to\gamma}$ can be split up into a perturbative part $D^{\mathrm{p}}_{q\to\gamma}(z)$ and a non-perturbative part $D^{\mathrm{np}}_{q\to\gamma}(z)$ such that

$$D_{q\to\gamma}(z) = D^{\mathrm{p}}_{q\to\gamma}(z) + D^{\mathrm{np}}_{q\to\gamma}(z). \tag{2.97}$$

To calculate $D^{\mathrm{p}}_{q\to\gamma}(z)$ in perturbation theory, one uses one-cutoff phase-space slicing with slicing parameter $s_{\min}$. In analogy to the treatment in Section 2.3.1, one splits the integration over $\hat{\sigma}_0((n+1)p+\gamma)$ into a part where all $n+2$ particles are resolved, i.e. $s_{q\gamma} > s_{\min}$ for all q, and into a part where only $n+1$ partons are resolved and the photon is degenerate with one of the partons, i.e. $s_{q\gamma} < s_{\min}$, leading to the decomposition

$$\int \mathrm{d}\hat{\sigma}_0((n+1)p+\gamma) = \int \mathrm{d}\hat{\sigma}_0^{n+2} + \int \mathrm{d}\hat{\sigma}_0^{n+1}. \tag{2.98}$$

Using

$$\mathrm{d}\hat{\sigma}_0^{n+1} = -\mathrm{d}\hat{\sigma}_0((n+1)p)\mathrm{d}z D^{\mathrm{p}}_{q\to\gamma}(z), \tag{2.99}$$

and factorisation properties of the matrix element and phase space, we find in dimensional regularisation (for more details of the derivation see Ref. [94])

$$\begin{aligned} D^{\mathrm{p,DR}}_{q\to\gamma}(z) &= -\frac{\alpha Q_q^2}{2\pi}\frac{(4\pi\mu^2)^\epsilon}{\Gamma(1-\epsilon)} P^{(\epsilon)}_{q\to\gamma}(z)\left[z(1-z)\right]^{-\epsilon}\int_0^{s_{\min}} \mathrm{d}s_{q\gamma}\frac{1}{s_{q\gamma}^{1+\epsilon}} \\ &= \frac{1}{\epsilon}\left(\frac{4\pi\mu^2}{s_{\min}}\right)^\epsilon \frac{1}{\Gamma(1-\epsilon)}\left(\frac{\alpha Q_q^2}{2\pi}\right)\frac{P^{(\epsilon)}_{q\to\gamma}(z)}{\left[z(1-z)\right]^\epsilon}, \end{aligned} \tag{2.100}$$

where the ϵ-dependent splitting function $P^{(\epsilon)}_{q\to\gamma}$ is given by

$$P^{(\epsilon)}_{q\to\gamma}(z) = \frac{1+z^2-\epsilon\,(1-z)^2}{1-z}. \tag{2.101}$$

We now go to the $\overline{\text{MS}}$ scheme and factorise the $1/\epsilon$-divergence into the fragmentation function at the scale μ_{F}

$$\begin{aligned} D^{\text{DR}}_{q\to\gamma}(z) &= D_{q\to\gamma}(z,\mu_{\text{F}}) + \frac{1}{\epsilon}\left(\frac{4\pi\mu^2}{\mu_F^2}\right)^{\epsilon}\frac{1}{\Gamma(1-\epsilon)}\left(\frac{\alpha Q_q^2}{2\pi}\right)P_{ff}(z) \\ &= D_{q\to\gamma}(z,\mu_F) + D^{\text{p,DR}}_{q\to\gamma}(z) + P_{ff}(z)\ln\left(\frac{s_{\min}}{\mu_{\text{F}}^2}(1-z)z\right) + (1-z). \end{aligned} \tag{2.102}$$

The function $D_{q\to\gamma}(z,\mu_F)$ can be experimentally determined. For example it has been measured at the ALEPH experiment using the ansatz

$$D^{\text{ALEPH}}_{q\to\gamma}(z,\mu_F) = \left(\frac{\alpha Q_q^2}{2\pi}\right)\left[P_{ff}(z)\ln\left(\frac{\mu_F^2}{\mu_0^2}\frac{1}{z^2}\right) + C\right], \tag{2.103}$$

with fitting parameters C and μ_0.

We can now proceed in a similar fashion to the parton-distribution-function approach used in hadron–hadron collisions, where a singular piece is factorised into the experimentally determined parton distributions. To this end, we use the experimentally determined contribution from the quark-to-photon fragmentation function and add it to the real corrections, with the hard-photon cut procedure included, and the virtual corrections, resulting in the infrared-safe cross section

$$\int \mathrm{d}\sigma^{\text{IR-safe}} = \int \mathrm{d}\sigma_{\text{virt}} + \int \mathrm{d}\sigma_{\text{real}}(z'_{\text{cut}}) + \int \mathrm{d}\sigma_{\text{frag}}(z'_{\text{cut}}), \tag{2.104}$$

where

$$\mathrm{d}\sigma_{\text{frag}}(z'_{\text{cut}}) = -\sum_{i=3}^{4}\frac{\alpha}{2\pi}Q_i^2\mathrm{d}\sigma_{\text{Born}}(q_i)\int_0^{z'_{\text{cut}}}\mathrm{d}z D_{q\to\gamma}(z). \tag{2.105}$$

Physically we can motivate this approach as follows. The virtual QED-type corrections include all quarks, even if these fragment into a quark-photon pair and should be rejected by the hard-photon cut. By adding $\mathrm{d}\sigma_{\text{frag}}$ to the $\mathcal{O}(\alpha)$ corrections, we correct for the effect of the hard-photon cut and compensate for excess terms related to collinear photon emission. In this way we can define an infrared-safe quantity even in the presence of the hard-photon cuts.

The result in Eq. (2.100) has been derived using dimensional regularisation and one-cutoff slicing. In the following we repeat the analysis, using particle masses as regulators, such that we can use the results in the calculation at hand. We begin with the perturbative part of the fragmentation function. In Eq. (2.37) of Section 2.3.1 we have seen how we can divide the phase space into a finite and a singular piece using the two parameters δ_s and δ_c. This procedure can be seen in full analogy to Eq. (2.98),

where we used the parameter $s_{\min}$ to define the singular region. The fragmentation process only takes place in the collinear region, i.e. the region defined by δ_c. Observing that Eq. (2.46) can be written as

$$\delta_q = |\,(q_q + k)^2 - m_q^2| = |s_{q\gamma} - m_q^2|, \tag{2.106}$$

together with Eq. (2.99), we find that the mass-regularised counterpart of Eq. (2.100) using two-cutoff slicing is given by [see Eqs. (2.45) and (2.48)]

$$\mathrm{D}_{q\to\gamma}^{\mathrm{p,MR}}(z,\delta_c) = -\left(\frac{\alpha Q_q^2}{2\pi}\right)\int_{(1-z)m_q^2/z}^{2z(1-z)(q_h^0)^2\delta_c}\frac{\mathrm{d}\delta_f}{\delta_f}\left[P_{ff}(z) - \frac{2m_q^2}{\delta_f}\right]. \tag{2.107}$$

Using Eq. (2.106), we can make the transition from two-cutoff to one-cutoff slicing as employed in Eq. (2.98), such that

$$\begin{aligned}\mathrm{D}_{q\to\gamma}^{\mathrm{p,MR}}(z,s_{\min}) &= -\left(\frac{\alpha Q_q^2}{2\pi}\right)\int_{m_q^2/z}^{s_{\min}}\frac{\mathrm{d}s}{s}\left[P_{ff}(z) - \frac{2m_q^2}{s}\right] \\ &= -\left(\frac{\alpha Q_q^2}{2\pi}\right)\left[P_{ff}(z)\ln\left(\frac{s_{\min}}{m_q^2}\frac{z}{1-z}\right) - \frac{2z}{1-z}\right].\end{aligned} \tag{2.108}$$

We now employ Eq. (2.102) in mass regularisation and find

$$D_{q\to\gamma}^{\mathrm{MR}}(z) = D_{q\to\gamma}(z,\mu_F) + \mathrm{D}_{q\to\gamma}^{\mathrm{p,MR}}(z,s_{\min}) + \left(\frac{\alpha Q_q^2}{2\pi}\right)\left[P_{ff}(z)\ln\left(\frac{s_{\min}z(1-z)}{\mu_F^2}\right) + 1 - z\right], \tag{2.109}$$

which allows us to write the bare fragmentation function using mass regularisation

$$D_{q\to\gamma}^{\mathrm{MR}}(z) = D_{q\to\gamma}(z,\mu_F) + \left(\frac{\alpha Q_q^2}{2\pi}\right)\left[P_{ff}(z)\ln\left(\frac{m_q^2}{\mu_F^2}(1-z)^2\right) + P_{ff}(z)\right]. \tag{2.110}$$

Inserting Eq. (2.103) into Eq. (2.110) we find

$$D_{q\to\gamma}^{\mathrm{ALEPH,MR}}(z) = \left(\frac{\alpha Q_q^2}{2\pi}\right)\left[P_{ff}(z)\ln\left(\frac{m_q^2}{\mu_0^2}\frac{(1-z)^2}{z^2}\right) + P_{ff}(z) + C\right]. \tag{2.111}$$

We can integrate Eq. (2.111) over z and find

$$\begin{aligned}\int_0^{z'_{\mathrm{cut}}}\mathrm{d}z D_{q\to\gamma}^{\mathrm{ALEPH,MR}}(z) &= Cz'_{\mathrm{cut}} - \frac{z'^2_{\mathrm{cut}}}{2} + \ln(1-z'_{\mathrm{cut}}) + 4\mathrm{Li}_2(z'_{\mathrm{cut}}) \\ &\quad - 2\ln(1-z'_{\mathrm{cut}})\ln\left(\frac{m_q^2}{\mu_0^2}\frac{(1-z'_{\mathrm{cut}})^2}{z'^2_{\mathrm{cut}}}\right) + 2\ln^2(1-z'_{\mathrm{cut}}) \\ &\quad - \left(z'_{\mathrm{cut}} + \frac{1}{2}z'^2_{\mathrm{cut}}\right)\ln\left(\frac{m_q^2}{\mu_0^2}\frac{(1-z'_{\mathrm{cut}})^2}{z'^2_{\mathrm{cut}}}\right).\end{aligned} \tag{2.112}$$

In the case of the phase-space-slicing method, we can add $\mathrm{d}\sigma_{\mathrm{frag}}(z'_{\mathrm{cut}})$ to $\mathrm{d}\sigma^{\mathrm{final}}_{\mathrm{coll.}}(z'_{\mathrm{cut}})$, which leads to

$$\begin{aligned}
\mathrm{d}\sigma_{\mathrm{frag}}(z'_{\mathrm{cut}}) + \mathrm{d}\sigma^{\mathrm{final}}_{\mathrm{coll.}}(z'_{\mathrm{cut}}) = &\sum_{i=3}^{4} \frac{\alpha}{2\pi} Q_i^2 \mathrm{d}\sigma_{\mathrm{Born}}(q_i) \left[\frac{9}{2} - \frac{2\pi^2}{3} - 4z'_{\mathrm{cut}} - Cz'_{\mathrm{cut}}\right. \\
&- \left(\frac{3}{2} + 2\ln\left(\Delta E/E_i\right)\right) \ln\left(\frac{4E_i^2\delta_c}{2m_i^2}\right) + 2\ln\left(\Delta E/E_i\right) \\
&- \frac{3}{2}\ln\left(1 - z'_{\mathrm{cut}}\right)^2 + \ln\left(\frac{4E_i^2\delta_c}{2\mu_0^2}\left(1 - z'_{\mathrm{cut}}\right)\right) \ln\left(1 - z'_{\mathrm{cut}}\right)^2 \\
&\left. + \left(z'_{\mathrm{cut}} + \frac{1}{2}z'^2_{\mathrm{cut}}\right) \ln\left(\frac{4E_i^2\delta_c}{2\mu_0^2}\left(1 - z'_{\mathrm{cut}}\right)^2\right)\right] \\
= \mathrm{d}\sigma^{\mathrm{final}}_{\mathrm{coll.}} - &\sum_{i=3}^{4} \left\{(4 + C)z'_{\mathrm{cut}}\right. \\
&+ \left(z'_{\mathrm{cut}} + \frac{1}{2}z'^2_{\mathrm{cut}}\right) \ln\left(\frac{4E_i^2\delta_c}{2\mu_0^2}(1 - z'_{\mathrm{cut}})^2\right) \\
&\left. + \left[-\frac{3}{2} + \ln\left(\frac{4E_i^2\delta_c}{2\mu_0^2}(1 - z'_{\mathrm{cut}})\right)\right] \ln\left((1 - z'_{\mathrm{cut}})^2\right) \right\}.
\end{aligned} \tag{2.113}$$

Eq. (2.113) consists of the original collinear contribution that cancels against the virtual corrections, and an additional, finite contribution, depending on the cut on the quark energy z'_{cut}.

In the case of the subtraction method, we can use charge conservation

$$\sum_i Q_i^2 = -\sum_{\substack{i,j \\ i \neq j}} (-1)^{(i+j)} Q_i Q_j, \tag{2.114}$$

to split $\mathrm{d}\sigma_{\mathrm{frag}}(z_{\mathrm{cut}})$ into a final-state emitter and final-state spectator, and a final-state emitter and initial-state spectator contribution, yielding

$$\mathrm{d}\sigma_{\mathrm{frag}}(z_{\mathrm{cut}}) = \sum_{i=3}^{4} \sum_{\substack{j=1 \\ j \neq i}}^{4} \frac{\alpha}{2\pi} (-1)^{i+j} Q_i Q_j \, \mathrm{d}\sigma_{\mathrm{Born}}(q_i) \int_{z_{\mathrm{cut}}}^{1} \mathrm{d}z D_{q\to\gamma}(z). \tag{2.115}$$

In the case of a final-state emitter and final-state spectator, we can add Eq. (2.115) to

Eq. (2.84), and find

$$\frac{\alpha}{4\pi s}\sum_{i=3}^{4}\sum_{\substack{j=3\\j\neq i}}^{4}\int\tilde{\Phi}_{0,ij}|\mathcal{M}_0\left(\tilde{q}_i,\tilde{q}_j\right)|^2\int_0^{z'_{\text{cut}}}\mathrm{d}z\left\{\bar{\mathcal{G}}^{\text{sub}}_{ij,\tau}\left(\tilde{s}_{ij},z\right)+D^{\text{ALEPH,MR}}_{q\to\gamma}(z)\right\}=$$

$$\frac{\alpha}{4\pi s}\sum_{i=3}^{4}\sum_{\substack{j=3\\j\neq i}}^{4}\int\tilde{\Phi}_{0,ij}|\mathcal{M}_0\left(\tilde{q}_i,\tilde{q}_j\right)|^2\left\{\left(\frac{3}{2}+C-\frac{z'_{\text{cut}}}{2}\right)z'_{\text{cut}}+\frac{3}{2}\ln\left(1-z'_{\text{cut}}\right)-\right.$$

$$\left[z'_{\text{cut}}+\frac{z'^2_{\text{cut}}}{2}+2\ln\left(1-z'_{\text{cut}}\right)\right]\ln\left(\frac{\tilde{s}_{ij}}{\mu_0^2}\frac{1-z'_{\text{cut}}}{z'_{\text{cut}}}\right)$$

$$\left.+2\text{Li}_2\left(z'_{\text{cut}}\right)\right\}. \tag{2.116}$$

Analogously, in the case of a final-state emitter and initial-state spectator using Eq. (2.93), we are left with

$$\frac{\alpha}{4\pi s}\sum_{i=3}^{4}\sum_{a=1,2}\int\tilde{\Phi}_{0,ia}|\mathcal{M}_0\left(\tilde{q}_i,\tilde{q}_a\right)|^2\int_0^{z'_{\text{cut}}}\mathrm{d}z\left\{\bar{\mathcal{G}}^{\text{sub}}_{ia,\tau}\left(\tilde{s}_{ia},z\right)+D^{\text{ALEPH,MR}}_{q\to\gamma}(z)\right\}=$$

$$\frac{\alpha}{4\pi s}\sum_{i=3}^{4}\sum_{a=1,2}\int\tilde{\Phi}_{0,ia}|\mathcal{M}_0\left(\tilde{q}_i,\tilde{q}_a\right)|^2\left\{\frac{\pi^2}{6}+\left(\frac{3}{2}+C-\frac{z'_{\text{cut}}}{2}\right)z'_{\text{cut}}+\frac{3}{2}\ln\left(1-z'_{\text{cut}}\right)-\right.$$

$$\left[z'_{\text{cut}}+\frac{z'^2_{\text{cut}}}{2}+2\ln\left(1-z'_{\text{cut}}\right)\right]\ln\left(\frac{\tilde{s}_{ia}}{\mu_0^2}\frac{1-z'_{\text{cut}}}{z'_{\text{cut}}}\right)$$

$$\left.+2\text{Li}_2\left(z'_{\text{cut}}\right)-2\text{Li}_2\left(z'_{\text{cut}}-1\right)\right\}. \tag{2.117}$$

Both Eq. (2.116) and Eq. (2.117) are now finite and only depend on the value of z'_{cut}, but not on the mass regulators.

2.3.6 Higher-order initial-state radiation

In order to achieve an accuracy at the per-mille level, we also include effects stemming from higher-order initial-state radiation using the structure-function approach as described in Refs. [87, 95]. The mass factorisation theorem states that the leading-logarithmic (LL) initial-state QED correction can be written as a convolution of the lowest-order cross section with structure functions according to

$$\int\mathrm{d}\sigma^{\text{LL}}=\int_0^1\mathrm{d}x_1\int_0^1\mathrm{d}x_2\Gamma^{\text{LL}}_{\text{ee}}(x_1,Q^2)\Gamma^{\text{LL}}_{\text{ee}}(x_2,Q^2)\int\mathrm{d}\sigma_{\text{Born}}(x_1q_1,x_2q_2), \tag{2.118}$$

where x_1 and x_2 denote the fractions of the incoming momenta just before the hard scattering, Q^2 is the typical scale at which the scattering occurs, and the structure

functions up to $\mathcal{O}(\alpha^3)$ are given by [87,95]

$$\begin{aligned}
\Gamma_{\rm ee}^{\rm LL} &= \frac{\exp\left(-\frac{1}{2}\beta_{\rm e}\gamma_{\rm E}+\frac{3}{8}\beta_{\rm e}\right)}{\Gamma\left(1+\frac{1}{2}\beta_{\rm e}\right)}\frac{\beta_{\rm e}}{2}(1-x)^{\frac{\beta_{\rm e}}{2}-1}-\frac{\beta_{\rm e}}{4}(1+x) \\
&\quad -\frac{\beta_{\rm e}^2}{32}\left\{\frac{1+3x^2}{1-x}\ln(x)+4(1+x)\ln(1-x)+5+x\right\} \\
&\quad -\frac{\beta_{\rm e}^3}{384}\Big\{(1+x)\left[6{\rm Li}_2(x)+12\ln^2(1-x)-3\pi^2\right] \\
&\quad +\frac{1}{1-x}\left[\frac{3}{2}(1+8x+3x^2)\ln(x)+6(x+5)(1-x)\ln(1-x)\right. \\
&\quad +12(1+x^2)\ln(x)\ln(1-x)-\frac{1}{2}(1+7x^2)\ln^2(x) \\
&\quad \left.+\frac{1}{4}(39-24x-15x^2)\right]\Big\}, \qquad (2.119)
\end{aligned}$$

where

$$\beta_{\rm e}=\frac{2\alpha}{\pi}(L-1), \qquad (2.120)$$

with leading logarithm

$$L=\ln\left(\frac{Q^2}{m_{\rm e}^2}\right), \qquad (2.121)$$

Γ is the Gamma function, and $\gamma_{\rm E}$ is the Euler–Mascheroni constant. In the calculation at hand we use $Q^2=s$.

When we add Eq. (2.118) to the one-loop result, we have to subtract the lowest-order and one-loop contributions $\mathrm{d}\sigma^{\rm LL,1}$ already contained in Eq. (2.119) to avoid double counting. They read

$$\begin{aligned}
\int \mathrm{d}\sigma^{\rm LL,1} &= \int_0^1 \mathrm{d}x_1 \int_0^1 \mathrm{d}x_2 \left[\delta(1-x_1)\delta(1-x_2)+\Gamma_{\rm ee}^{\rm LL,1}(x_1,Q^2)\delta(1-x_2)\right. \\
&\quad \left.+\Gamma_{\rm ee}^{\rm LL,1}(x_2,Q^2)\delta(1-x_1)\right]\int \mathrm{d}\sigma_{\rm Born}(x_1q_1,x_2q_2), \qquad (2.122)
\end{aligned}$$

where the one-loop structure functions are given by

$$\Gamma_{\rm ee}^{\rm LL,1}=\frac{\beta_{\rm e}}{4}\left[\frac{1+x^2}{1-x}\right]_+. \qquad (2.123)$$

Chapter 3

Implementation

In the previous chapter we presented strategies for the calculation of physical observables at the one-loop level. We showed how to isolate and analytically control IR divergencies, making the numerical integration over the three- and four-particle phase space feasible. The implementation of these techniques builds on the FORTRAN program POLE by C. Meier [96]. POLE has been developed to calculate one-loop electroweak corrections to infrared-safe observables with identified particles in the final state, both for lepton and hadron colliders, using Monte Carlo integration techniques. In the calculation at hand we want to calculate event-shape distributions with jets, i.e. unidentified particles in the final state, using the non-infrared-safe hard-photon cut procedure and the fragmentation-function approach to restore infrared safety as described in the previous chapter. Therefore the functionality of POLE had to be extended. While the implementation of the non-collinear-safe phase-space-slicing and subtraction method, as well as the fragmentation-function approach are straightforward in the framework of POLE, the implementation of the event selection is more involved.

We briefly outline the principles of Monte Carlo integration in Section 3.1, following the discussion in Ref. [97]. We then describe the details of the implementation of the event selection procedure in Section 3.2. Finally, we give an overview of the functionality of the resulting program EW3J in Section 3.3. For more details of the other features of the program the reader is referred to Ref. [96].

3.1 Monte Carlo integration

Monte Carlo integration techniques are commonly used when dealing with complicated integrals over a multi-dimensional space. Consider the integral of a function $f(u_1, \ldots, u_d)$ of d variables $u_1, \ldots, u_d$ over the unit hypercube $[0,1]^d$, and denote a point in the unit hypercube by $x = (u_1, \ldots, u_d)$. If f is square-integrable then the

Monte Carlo estimate of the integral

$$I = \int \mathrm{d}x f(x), \tag{3.1}$$

is given by

$$E = \frac{1}{N} \sum_{n=1}^{N} f(x_n), \tag{3.2}$$

where the number of points inside the hypercube N have to be uniformly distributed. Because of the law of large numbers, the Monte Carlo estimate converges to the true value of the integral, such that

$$\lim_{N\to\infty} \frac{1}{N} \sum_{n=1}^{N} f(x_n) = I. \tag{3.3}$$

One can show that

$$\int \mathrm{d}x_1 \ldots \int \mathrm{d}x_N \left(\frac{1}{N} \sum_{n=1}^{N} f(x_n) - I \right)^2 = \frac{\sigma^2(f)}{N}, \tag{3.4}$$

where the variance $\sigma^2(f)$ of $f(x)$ is given by

$$\sigma^2(f) = \int \mathrm{d}x \left(f(x) - I \right)^2. \tag{3.5}$$

Therefore it can be argued that the error of the Monte Carlo estimate is on average $\sigma(f)/\sqrt{N}$, where $\sigma(f)$ is the standard deviation of f. According to the central-limit theorem, the probability that

$$I - a\frac{\sigma(f)}{\sqrt{N}} \leq E \leq I + b\frac{\sigma(f)}{\sqrt{N}}, \tag{3.6}$$

is given by

$$\lim_{N\to\infty} \mathrm{Prob}\left(-a\frac{\sigma(f)}{\sqrt{N}} \leq \sum_{n=1}^{N} f(x_n) - I \leq b\frac{\sigma(f)}{\sqrt{N}} \right) = \frac{1}{\sqrt{2\pi}} \int_{-a}^{b} \mathrm{d}t \exp\left(-\frac{t^2}{2} \right). \tag{3.7}$$

In practise it is not feasible to compute the variance $\sigma^2(f)$ directly, and one uses the Monte Carlo estimate

$$S^2 = \frac{1}{N-1} \sum_{n=1}^{N} \left(f(x_n) - E \right)^2 = \frac{1}{N-1} \sum_{n=1}^{N} \left[\left(f(x_n) \right)^2 - E^2 \right], \tag{3.8}$$

instead. From the above results we can deduce that the error using Monte Carlo integration scales like $1/\sqrt{N}$ and is independent of the dimension d of the integral.

If one wants to integrate a function g over a complicated region W one can proceed as follows. Find a region V that contains W and that can be easily sampled by random numbers. Then define a function f that is equal to g in W and zero outside of W, and proceed as described in the previous paragraph. The problem with this approach is that the points chosen outside of W do not contain any information and therefore effectively reduce the number of points used in the calculation.

Consider the phase-space integrations in Eq. (2.6) and Eq. (2.35). The matrix elements in the integrand show a rich peaking behaviour in different regions of the phase space. In order to improve the rate of convergence and to reduce the number of events needed in the integration, POLE uses the multi-channel Monte Carlo method [98–102]. Suppose the integrand only exhibits a single peak. A change of variables leads to

$$\int \mathrm{d}x f(x) = \int \frac{f(x)}{p(x)} p(x)\mathrm{d}x = \int \frac{f(x)}{p(x)} \mathrm{d}P(x), \tag{3.9}$$

with

$$p(x) = \frac{\partial^d}{\partial x_1 \dots \partial x_d} P(x). \tag{3.10}$$

If

$$p(x) \geq 0, \quad \text{and} \quad \int p(x)\mathrm{d}x = 1, \tag{3.11}$$

then $p(x)$ can be interpreted as a probability density function. Generating random numbers according to the distribution $P(x)$ leads to the Monte Carlo estimate of the integral

$$E = \frac{1}{N} \sum_{n=1}^{N} \frac{f(x_n)}{p(x_n)}. \tag{3.12}$$

Hence, we find for the Monte Carlo estimate of the variance

$$S^2\left(\frac{f}{p}\right) = \frac{1}{N} \sum_{n=1}^{N} \left(\frac{f(x_n)}{p(x_n)}\right)^2 - E^2. \tag{3.13}$$

Therefore choosing the function $p(x)$ such that it approximates the function $f(x)$ leads to a reduction of the Monte Carlo error.

In the case where $f(x)$ shows various peaks in different regions it can be hard to find a single function that approximates $f(x)$ for all the peaks. If one knows the behaviour for the single peaks, however, one can use the multi-channel Monte Carlo technique where each peak is referred to as a single channel. Let $p_i(x)$ be the probability density

of channel i and $P_i^{-1}(y)$ a mapping of random numbers y distributed according to $p_i(x)$. Furthermore, let $\alpha_i \geq 0$, $i = 1, \ldots, m$, where m is the number of channels, such that

$$\sum_{i=1}^{m} \alpha_i = 1. \tag{3.14}$$

Selecting a single channel i with probability α_i leads to

$$I = \int \mathrm{d}x f(x) = \sum_{i=1}^{m} \alpha_i \int \frac{f(x)}{p(x)} \mathrm{d}P_i(x), \tag{3.15}$$

where

$$p(x) = \sum_i \alpha_i p_i(x). \tag{3.16}$$

The Monte Carlo average of the integral is then given by

$$E = \frac{1}{N} \sum_{i=1}^{m} \sum_{n_i=1}^{N_i} \frac{f(x_{n_i})}{p(x_{n_i})}, \tag{3.17}$$

where each channel is approximately evaluated $\alpha_i N$ times. The Monte Carlo estimate of the integration error is given by

$$\sqrt{\frac{W(\alpha) - I^2}{N}}, \tag{3.18}$$

with

$$W(\alpha) = \sum_{i=1}^{m} \alpha_i \int \left(\frac{f(x)}{p(x)} \right)^2 \mathrm{d}P_i(x). \tag{3.19}$$

One can try to minimise $W(\alpha)$ through a clever choice of the α_i. The details of the implementation of the multi-channel algorithm in POLE can be found in Refs. [96, 103].

3.2 Event selection

In this section we describe in detail the implementation of the event selection as presented in Section 1.2.4. Since the hard-photon isolation cut directly influences the cancellation of soft and collinear singularities it is crucial to implement it consistently. The main ingredient hereby is the jet algorithm. We included a subroutine that calculates the parameters $y_{ij,\mathrm{J}}$, $y_{ij,\mathrm{D}}$, and $y_{ij,\mathrm{G}}$ of the Jade, Durham, and Geneva jet algorithms, respectively. Consider for example a four-parton event and the Durham jet algorithm. First, we calculate the value $y_{34,\mathrm{D}}$ which is the maximum value of $y_{\mathrm{cut,D}}$ where one of

the final-state momenta is clustered together with another final-state momentum. The quantity $y_{34,\mathrm{D}}$ is a measure for the transition of a four-jet to a three-jet event in the Durham scheme. In the second step, we calculate the value $y_{23,\mathrm{D}}$ which is the maximum value of $y_{\mathrm{cut,D}}$ where two of the final-state momenta are clustered together with either one other final-state momentum or two different final-state momenta. The quantity $y_{23,\mathrm{D}}$ is a measure for the transition of a four-jet to a two-jet event in the Durham scheme. In the case of a three-parton event, $y_{34,\mathrm{D}}$ is always zero and we only calculate $y_{23,\mathrm{D}}$ which is the maximum value of $y_{\mathrm{cut,D}}$ where one of the final-state momenta is clustered together with another final-state momentum. Here, $y_{23,\mathrm{D}}$ is a measure for the transition of a three-jet to a two-jet event.

In our calculation we choose a fixed value for y_{cut}, and thus consider an event four-jet like if

$$y_{\mathrm{cut}} < y_{34,\mathrm{D}},$$

three-jet like if

$$y_{34,\mathrm{D}} < y_{\mathrm{cut}} < y_{23,\mathrm{D}},$$

and two-jet like if

$$y_{23,\mathrm{D}} < y_{\mathrm{cut}}.$$

We have implemented the E-, E_0-, P-, and P_0-schemes for the recombination procedure, and use the P_0-scheme by default. For technical reasons, the jet algorithm requires the final-state momenta to be in their centre-of-mass system. Furthermore, the subroutine returns the photonic energy fraction in a jet z if one of the particles in the final state is a photon.

Throughout the calculation we encounter three types of final-state momenta. First, three-particle final-state momenta in their centre-of-mass system in the calculation of the Born, virtual, and non-ISR parts of the slicing or subtraction matrix elements. Here, the centre-of-mass system is equivalent to the laboratory system. Second, three-particle final state momenta after the emission of an ISR photon for the calculation of the ISR parts of the slicing or subtraction matrix elements. These momenta are given in the laboratory system that is not equivalent to their centre-of-mass system. And third, four-particle momenta in the calculation of the real-radiation matrix elements. Here, the centre-of-mass system is again equivalent to the laboratory system.

In addition to the cut on the energy fraction of the photon in the jet, we also implemented a cut on the production angle with respect to the beam pipe, taking into account the restricted opening angle of the detector. Here it is important to calculate the production angle with respect to the beam axis in the laboratory frame, before boosting the final-state momenta into their centre-of-mass system, as required by the jet algorithm.

We now turn to the evolution of the event selection, starting with three-particle final states. First, we calculate the production angle of all particle momenta with the beam.

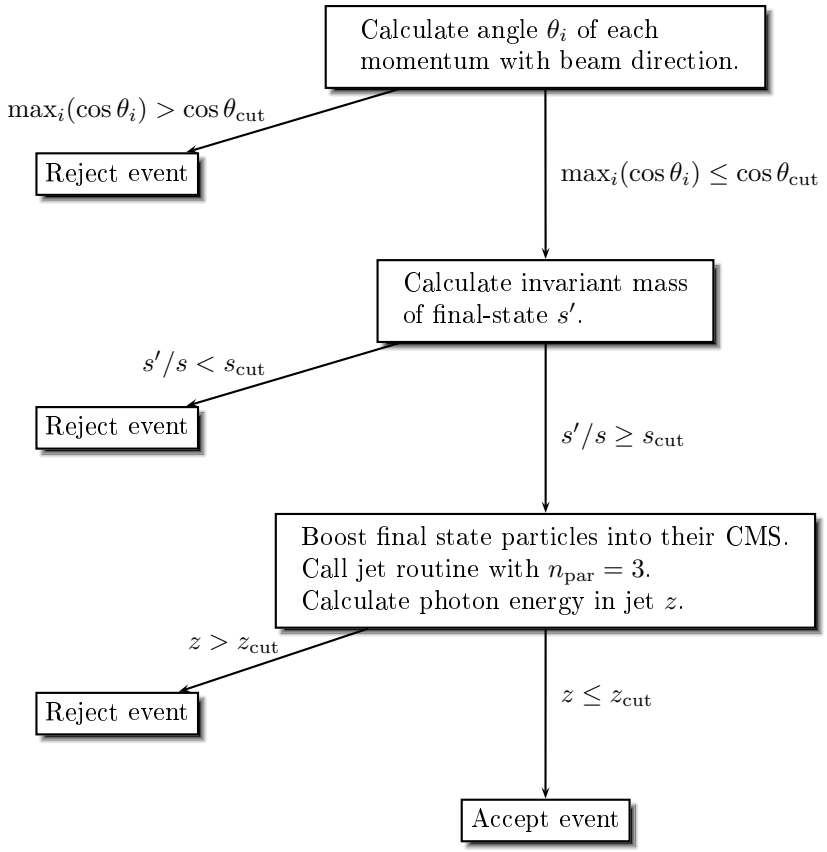

Figure 3.1: Three-parton event selection.

If one or more angles are smaller than a given value $\Theta_{\rm cut}$, the event is rejected, since it leads to a two-parton final state that only contributes to the endpoint of all event shape distributions. In the next step, the invariant mass of the final state $s' = (p_3 + p_4 + p_5)^2$ is calculated. This quantity is only different from the centre-of-mass energy squared in the calculation of the ISR parts of the slicing or subtraction matrix elements. If s'/s is lower than a preset value $s_{\rm cut}$, the event is rejected. Now we boost the momenta in their centre-of-mass system, execute the jet algorithm for three particles, and obtain the photonic energy fraction in a jet. If z is larger than a given value $z_{\rm cut}$ the event is rejected, otherwise it is accepted. A schematic overview of this procedure can be found in Fig. 3.1.

In the case of four-parton final states, we first calculate the production angle of all particle momenta with the beam. If two or more angles are smaller than a given value $\Theta_{\rm cut}$, the event is rejected, since it leads to a back-to-back two-particle final state. If

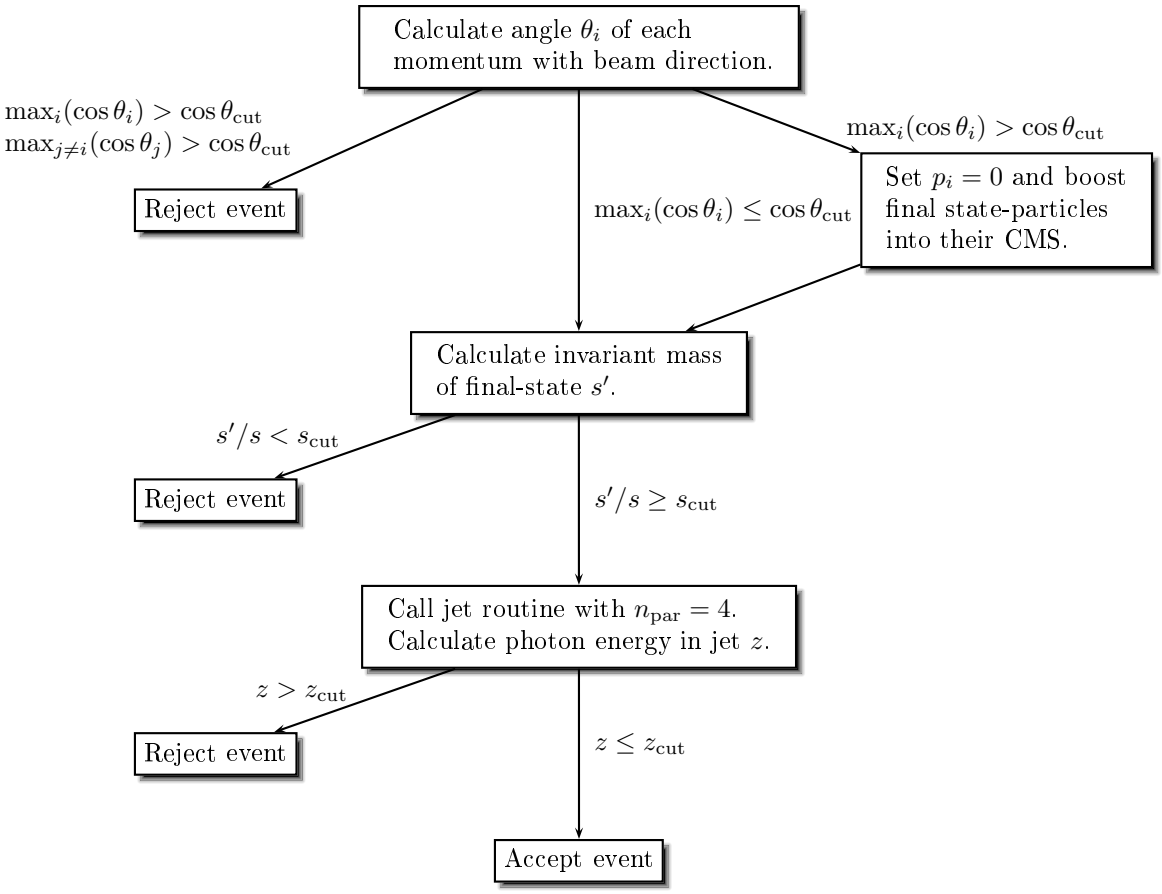

Figure 3.2: Four-parton event selection.

one angle is smaller than the cut value, we set the corresponding momentum to zero and boost the remaining momenta into their centre-of-mass frame. In the next step, we calculate the invariant mass of the final state $s' = (p_3 + p_4 + p_5 + p_6)^2$ and reject the event for $s'/s < s_{\rm cut}$. Next we execute the jet algorithm for four particles, obtain z, and reject the event if z is larger than $z_{\rm cut}$. Otherwise we accept the event. A schematic overview of this procedure can be found in Fig. 3.2. Note that in the case where a photon is present in the final state and it is not recombined with another particle, we find a purely photonic jet with $z = 1$ and the event is rejected.

In the calculation of $\sigma_{\rm had}$ we also encounter two-particle quark–antiquark final states. In this case, we only apply the cut on the production angle θ_i, where i can be either the quark or the antiquark. If we find $\cos\theta_i > \cos\theta_{\rm cut}$ for one of the particles we discard the event. The respective Bremsstrahlung process with quark–antiquark–photon final

states is treated as discussed in the case with three-particle final-states above with the only difference that we reject events where two particles are close to the beam. In this way we ensure that both the event-shape distribution and the normalisation to σ_{had} are treated in the same way, such that the expected cancellation of large initial-state radiation effects can take place.

Once an event passes the above cut routine, we proceed with the calculation of the event-shape observables. The observables defined in Section 1.2.2 are calculated in a single run of the program, where we impose an additional cut individually for each histogram. This cut is chosen such that the singularity in the two-jet region is avoided, typically as a lower cut-off for the respective observable (see Section 4.1). In this way the cut affects only the first bin of the histogram and does not cause a distortion of the shape of the distribution.

3.3 Functionality of the program

In this section we give an overview of the functionality of the program EW3J. The program is designed to calculate the electroweak corrections to the process defined in Eq. (2.3) and the QCD corrections to the process defined in Eq. (2.4) at arbitrary centre-of-mass energies. Both processes share the Bremsstrahlung process as defined in Eq. (2.34), such that phase-space slicing or subtraction both for the photon and the gluon in the real-radiation part is employed.

The input scheme for the electromagnetic coupling constant can be chosen to be either the $\alpha(0)$-scheme or the modified G_μ scheme. In the G_μ scheme the electromagnetic coupling is fixed via

$$\alpha = \alpha_{G_\mu} = \sqrt{2} G_\mu M_{\text{W}}^2 \left(1 - M_{\text{W}}^2/M_{\text{Z}}^2\right)/\pi,$$

where G_μ is the Fermi constant. The weak corrections to muon decay Δr are in this way contained in the charge renormalisation constant [104–107]. As a consequence the Born cross section times the constant Δr has to be subtracted from the virtual corrections once for each coupling in the Born amplitude that is parameterised by $\sqrt{\alpha_{G_\mu}}$. At the one-loop level Δr is given by

$$\begin{aligned}
\Delta r^{(1)} \;=\; & \frac{\partial \Sigma^{\gamma\gamma}(k^2)}{\partial k^2}\Big|_{k^2=0} - \frac{\cos^2\theta_{\text{w}}}{\sin^2\theta_{\text{w}}}\left(\frac{\Sigma^{\text{ZZ}}(M_{\text{Z}}^2)}{M_{\text{Z}}^2} - \frac{\Sigma^{\text{WW}}(M_{\text{W}}^2)}{M_{\text{W}}^2}\right) \\
& + \frac{\Sigma^{\text{WW}}(0) - \Sigma^{\text{WW}}(M_{\text{W}}^2)}{M_{\text{W}}^2} + 2\frac{\cos\theta_{\text{w}}}{\sin\theta_{\text{w}}}\frac{\Sigma^{\gamma\text{Z}}(0)}{M_{\text{Z}}^2} \\
& + \frac{\alpha}{4\pi\sin^2\theta_{\text{w}}}\left[6 + \frac{7 - 4\sin^2\theta_{\text{w}}}{2\sin^2\theta_{\text{w}}}\ln\left(\cos^2\theta_{\text{w}}\right)\right],
\end{aligned} \tag{3.20}$$

where $\Sigma^{VV'}(k^2)$ denotes the transverse part of the VV' gauge-boson self-energy at momentum transfer k^2.

As the leading electromagnetic corrections are related to the emission of real photons, we fix the electromagnetic coupling appearing in the relative corrections by $\alpha = \alpha(0)$, which is the appropriate choice for the leading photonic corrections. This is referred to as the modified G_μ scheme. Accordingly the cross section for $e^+e^- \to q\bar{q}g$ is proportional to $\alpha^2_{G_\mu}\alpha_s$, while the electroweak corrections to this process are proportional to $\alpha(0)\alpha^2_{G_\mu}\alpha_s$.

Finally, the following choices can be made:

- switch higher-order ISR as described in Section 2.3.6 on or off,
- calculate distributions for polarised or unpolarised incoming electrons and positrons,
- include only up-type (up, charm), down-type (down, strange), bottom-type final states, or the sum over the five light flavors,
- include the full $\mathcal{O}(\alpha)$ corrections or only weak (fermionic and massive bosonic loops) contributions.

Chapter 4

Results

In this chapter we present the results obtained with the program EW3J as discussed in Chapter 3. In Section 4.1 we describe our choice of input parameters. In Section 4.2 we discuss a number of checks we performed to prove the reliability of our results. In Section 4.3 we give the results for the total hadronic cross section for various energies as needed in the normalisation of the distributions as derived in Section 1.2.3. In Section 4.4 we display our findings for jet rates and event-shape distributions according to the discussion in Sections 1.2.1 and 1.2.2. The event-selection and particle identification is realised as highlighted in Section 3.2. The same criteria are applied in the calculation of $\sigma_{\rm had}$ and the jet rates and event-shape distributions. We investigate the effect of these event-selection cuts on the shape of the distributions in Section 4.5, using thrust as an example. In Section 4.6 we compare our findings to results already existing in the literature.

4.1 Input parameters and setup

We use the following set of input parameters [108],

$$\begin{aligned}
G_\mu &= 1.16637 \times 10^{-5}\,\mathrm{GeV}^{-2}, \quad \alpha(0) = 1/137.03599911, \quad \alpha_{G_\mu} = 1/132.43421099 \\
\alpha_{\rm s}(M_{\rm Z}) &= 0.1176, \\
M_{\rm W}^{\rm LEP} &= 80.403\,\mathrm{GeV}, \qquad \Gamma_{\rm W}^{\rm LEP} = 2.141\,\mathrm{GeV}, \\
M_{\rm Z}^{\rm LEP} &= 91.1876\,\mathrm{GeV}, \qquad \Gamma_{\rm Z}^{\rm LEP} = 2.4952\,\mathrm{GeV}, \\
m_{\rm e} &= 0.51099892\,\mathrm{MeV}, \qquad m_{\rm t} = 171.0\,\mathrm{GeV}, \qquad M_{\rm H} = 120\,\mathrm{GeV}.
\end{aligned} \tag{4.1}$$

We employ the complex-mass scheme [72], where a fixed width enters the resonant W- and Z-boson propagators, in contrast to the approach used at LEP to fit the W and Z resonances, where running widths are taken. Therefore, we have to convert the "on-shell" values of $M_V^{\rm LEP}$ and $\Gamma_V^{\rm LEP}$ ($V = {\rm W}, {\rm Z}$), resulting from LEP, to the "pole values"

denoted by M_V and Γ_V. The relation between the two sets is given by [109]

$$M_V = M_V^{\mathrm{LEP}}/\sqrt{1+(\Gamma_V^{\mathrm{LEP}}/M_V^{\mathrm{LEP}})^2}, \qquad \Gamma_V = \Gamma_V^{\mathrm{LEP}}/\sqrt{1+(\Gamma_V^{\mathrm{LEP}}/M_V^{\mathrm{LEP}})^2}, \tag{4.2}$$

leading to

$$\begin{aligned} M_{\mathrm{W}} &= 80.375\ldots\,\mathrm{GeV}, & \Gamma_{\mathrm{W}} &= 2.140\ldots\,\mathrm{GeV}, \\ M_{\mathrm{Z}} &= 91.1535\ldots\,\mathrm{GeV}, & \Gamma_{\mathrm{Z}} &= 2.4943\ldots\,\mathrm{GeV}. \end{aligned} \tag{4.3}$$

The scale dependence of α_{s} is determined according to the three-loop running [see Eq. (1.11)]. The number of active flavours is $n_{\mathrm{F}} = 5$ below m_{t} which leads to $\Lambda_5 = 0.221$. Above m_{t} we use six active flavours and obtain $\Lambda_6 = 0.089$. This results for example in $\alpha_{\mathrm{s}}(206\,\mathrm{GeV}) = 0.1050$ and $\alpha_{\mathrm{s}}(500\,\mathrm{GeV}) = 0.0949$.

We neglect effects due to quark mixing and set the CKM matrix to unity. Throughout this work, we parametrise the couplings appearing in LO in the G_μ scheme, whereas we fix the electromagnetic coupling appearing in the relative corrections by $\alpha = \alpha(0)$ (see Section 3.3). If not stated otherwise, we use the following set of parameters for the event selection:

$$\cos\theta_{\mathrm{cut}} = 0.965, \quad s_{\mathrm{cut}} = 0.81, \quad z_{\mathrm{cut}} = 0.9, \quad y_{\mathrm{cut}} = 0.002, \tag{4.4}$$

according to the event-selection criteria used in the ALEPH analysis [61] and employ the Durham jet algorithm together with the P_0 recombination scheme for the reconstruction of isolated photons (see Section 1.2.1).

As mentioned in Section 3.2, we implement a cut such that the singularity in the two-jet region is avoided. This cut requires the variables T, ρ, B_{T}, B_W, and C to be greater than 0.005, whereas Y_3 and y_{cut} for $\sigma_{3-\mathrm{jet}}$ are required to be greater than 0.00005. In this way the cut influences only the first bin of the respective distribution.

4.2 Checks of the calculation

To prove the reliability of our results, we performed the following checks:

- *UV finiteness* is checked through varying the reference scale μ of dimensional regularisation and finding that our results are independent of this variation.
- *IR finiteness* is verified through varying the infinitesimal photon mass m_γ and observing that the sum of the virtual corrections and the soft-photonic corrections in both the slicing and subtraction approach is invariant.
- *Mass singularities* related to collinear photon emission or exchange are shown to cancel between the virtual and the subtraction endpoint contributions by varying the small masses of the external fermions.

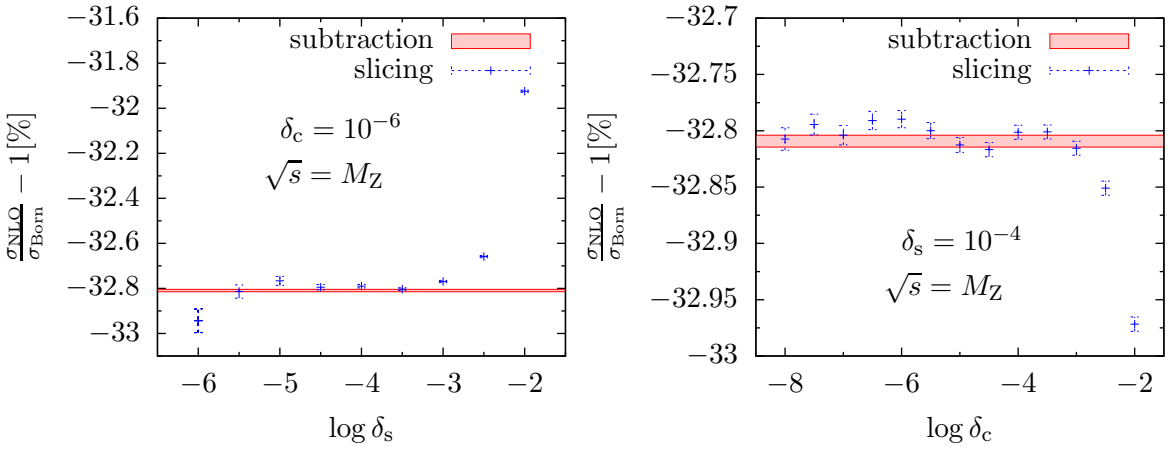

Figure 4.1: Slicing cut dependence of $\sigma_{\text{had}}\,(M_Z)$.

- *Two completely independent* calculations have been performed within our collaboration, one by S. Dittmaier and T. Gehrmann, the other by A. Denner and C. Kurz. We find complete agreement of the results for σ_{had}, jet rates, and event-shape distributions at the level of the Monte Carlo integration error which typically is at the per-mille level. For us, this constitutes the most important and convincing check.

Furthermore, we compare the results obtained with phase-space slicing and the subtraction method, which are completely independent techniques. In Fig. 4.1 we show the mutual agreement of both techniques for the NLO EW results for σ_{had}, in Fig. 4.2 for the full $\mathcal{O}(\alpha)$ results for the three-jet rate with $y_{\text{cut}} = 0.0006$ at $\sqrt{s} = M_Z$, and in Fig. 4.3 for the full $\mathcal{O}(\alpha)$ results for the thrust distribution at $\sqrt{s} = 206\,\text{GeV}$. We find that within integration errors the slicing results become independent of the cut-offs for $\delta_s \lesssim 10^{-3}$ and $\delta_c \lesssim 10^{-4}$ and fully agree with the results obtained using the subtraction method. For the sake of clarity, we show only curves for values of the slicing parameters that lie on the plateau in Fig. 4.3. For values of the slicing parameters outside the plateau, the behaviour follows the same pattern as in Figs. 4.1 and 4.2.

It turns out that the subtraction method is more efficient in terms of run-time compared to phase-space slicing. To obtain the results in Fig. 4.1, we use phase-space slicing with 10^6 events for the virtual corrections and 4×10^9 events for the real corrections, whereas when employing the subtraction approach we only use 4×10^8 events for the real corrections. In the case of phase-space slicing this results in a run-time of 18h on a single CPU, and in the case of subtraction it results in a run-time of 10h on a single CPU. For the thrust distribution shown in Fig. 4.3, we use phase-space slicing with 2×10^6 events for the virtual corrections and 5×10^9 events for the real corrections,

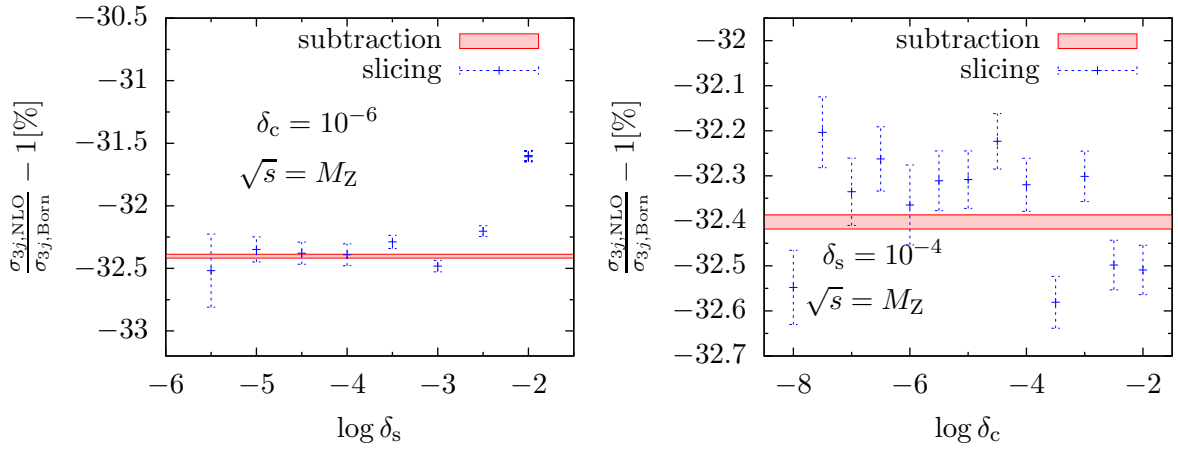

Figure 4.2: Dependence of the three-jet rate on the slicing parameters at $\sqrt{s} = M_Z$ for $y_{cut} = 0.0006$.

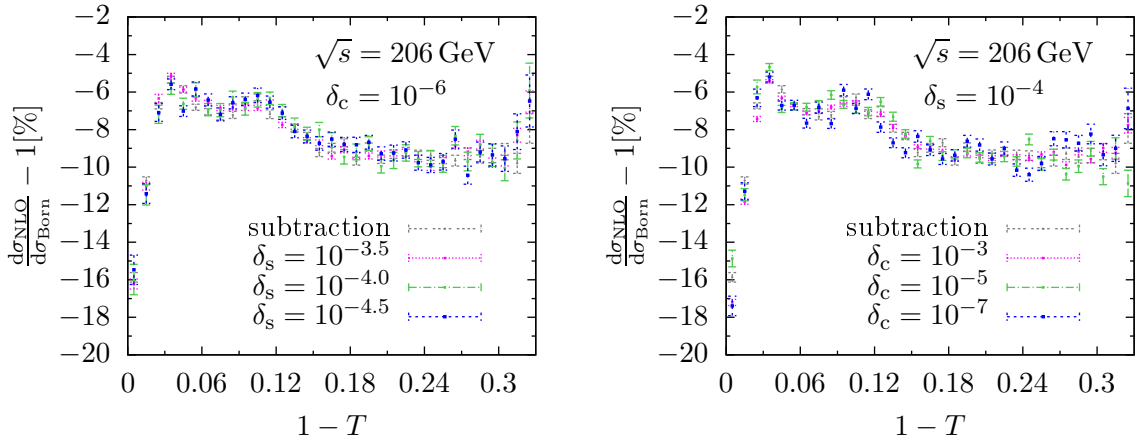

Figure 4.3: Dependence of the differential thrust distribution on the slicing parameters at $\sqrt{s} = 206\,\text{GeV}$.

whereas when employing the subtraction approach we only use 2×10^8 events for the real corrections. In the case of phase-space slicing this results in a run-time of 44h on a single CPU, and in the case of subtraction it results in a run-time of 23h on a single CPU. We therefore choose to use the subtraction method in the calculations presented in the following sections, both for σ_{had} and jet rates and event-shape distributions.

This analysis shows that the bulk of the run-time is used for the calculation of the real radiation process and the run-time for the virtual corrections is almost negligible.

4.3 Results for the total hadronic cross section

In Figure 4.4, we display the total hadronic cross section σ_{had} including NLO electroweak corrections and the relative corrections separately. We use the event selection as described in Section 3.2 with the parameters given in Eq. (4.4). For the latter, 'weak' refers to the electroweak NLO corrections without purely photonic corrections.

For most energies, the electroweak corrections are sizable and negative, ranging between -30% at the Z peak and about -10% at energies above and below. The numerically largest contribution is always due to ISR. However, above the Z resonance up to about 110 GeV the corrections are positive and of the order of the Born cross section due to the well-known radiative-return phenomenon [110]. It occurs only in this region because of our choice of s_{cut} and assumes its maximum for $\sqrt{s} \approx 100\,\text{GeV}$. Below 60 GeV and above 120 GeV the magnitude of the corrections is increased due to LL resummation of ISR, whereas it is decreased in the region in between. The virtual one-loop weak corrections (from fermionic and massive bosonic loops) yield only a moderate correction between -6% and $+5\%$ and are always negative for $M_{\text{Z}} < \sqrt{s} < 1\,\text{TeV}$.

Table 4.1 shows the Born contribution to σ_{had} in the first row, the weak $\mathcal{O}(\alpha)$ contribution in the second row, the full $\mathcal{O}(\alpha)$ contribution in the third row, and the full $\mathcal{O}(\alpha)$+ h.o. LL contribution in the fourth row for LEPI and LEPII energies, as well as for $\sqrt{s} = 500\,\text{GeV}$ and $\sqrt{s} = 1000\,\text{GeV}$. We show the absolute results in nanobarn in the first column and the relative corrections in per-cent in the second column. The numbers in parentheses give the uncertainties from Monte Carlo integration in the last digits of the predictions. From these values we extract $\delta_{\sigma,1}$ and $\delta_{\sigma,\text{LL}}$, as defined in Eq. (1.34) and Eq. (1.38), which in turn enter the calculation of normalised event-shape distributions and jet rates.

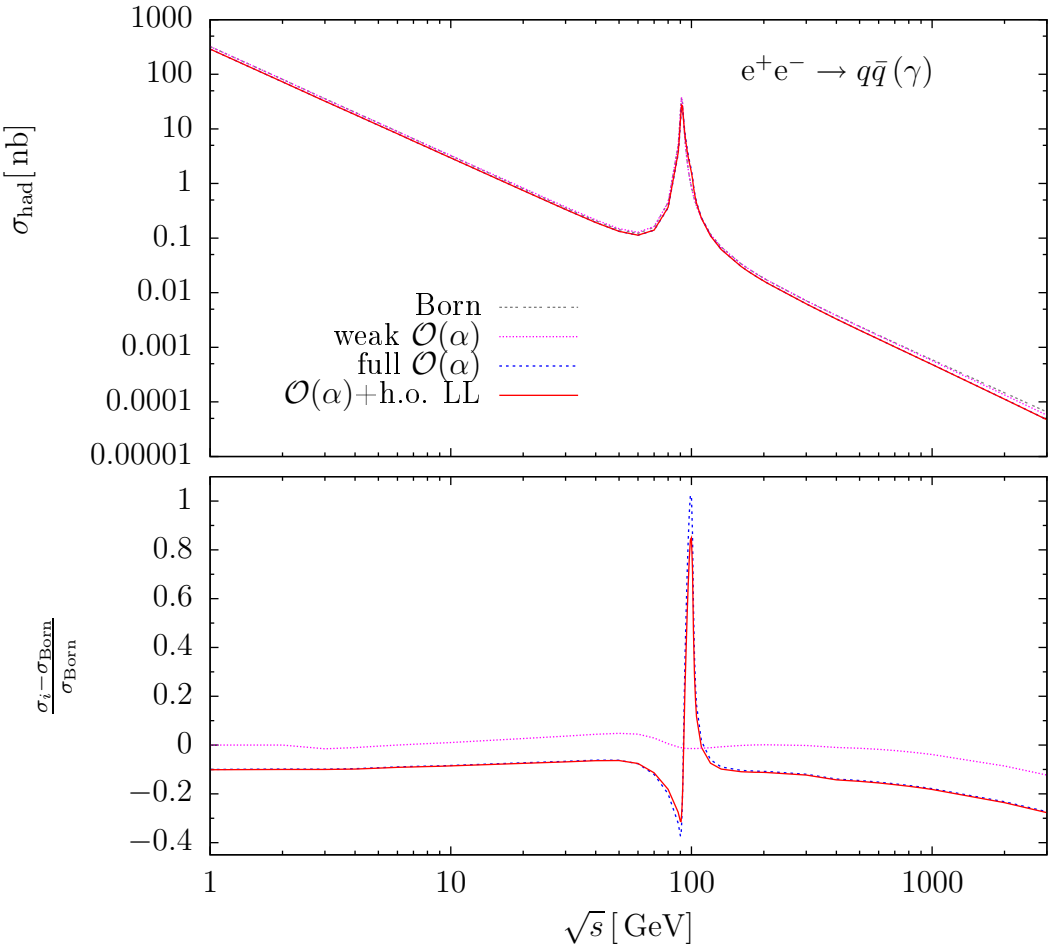

Figure 4.4: Total hadronic cross section $\sigma_{\mathrm{had}}\,(\sqrt{s})$.

	$\sqrt{s} = M_{\mathrm{Z}}$	$\frac{\mathrm{d}\sigma_i - \mathrm{d}\sigma_{\mathrm{Born}}}{\mathrm{d}\sigma_{\mathrm{Born}}}[\%]$	$\sqrt{s} = 133\,\mathrm{GeV}$	$\frac{\mathrm{d}\sigma_i - \mathrm{d}\sigma_{\mathrm{Born}}}{\mathrm{d}\sigma_{\mathrm{Born}}}[\%]$
$\sigma_{\mathrm{had}}^{\mathrm{Born}}/\,\mathrm{nb}$	38.2845(15)		0.068858(2)	
$\sigma_{\mathrm{had}}^{\mathrm{weak}}/\,\mathrm{nb}$	37.8541(2)	−1.1	0.068348(2)	−0.7
$\sigma_{\mathrm{had}}^{\mathrm{NLO}}/\,\mathrm{nb}$	25.729(3)	−32.8	0.06269(2)	−9
$\sigma_{\mathrm{had}}^{\mathrm{NLO+h.o.LL}}/\,\mathrm{nb}$	27.341(3)	−28.6	0.06208(2)	−9.8

	$\sqrt{s} = 161\,\mathrm{GeV}$	$\frac{\mathrm{d}\sigma_i - \mathrm{d}\sigma_{\mathrm{Born}}}{\mathrm{d}\sigma_{\mathrm{Born}}}[\%]$	$\sqrt{s} = 172\,\mathrm{GeV}$	$\frac{\mathrm{d}\sigma_i - \mathrm{d}\sigma_{\mathrm{Born}}}{\mathrm{d}\sigma_{\mathrm{Born}}}[\%]$
$\sigma_{\mathrm{had}}^{\mathrm{Born}}/\,\mathrm{nb}$	0.0338283(10)		0.0276993(8)	
$\sigma_{\mathrm{had}}^{\mathrm{weak}}/\,\mathrm{nb}$	0.0337575(10)	−0.2	0.0276780(8)	−0.1
$\sigma_{\mathrm{had}}^{\mathrm{NLO}}/\,\mathrm{nb}$	0.030309(9)	−10.4	0.024770(7)	−10.6
$\sigma_{\mathrm{had}}^{\mathrm{NLO+h.o.LL}}/\,\mathrm{nb}$	0.030124(9)	−11	0.024633(7)	−11.1

	$\sqrt{s} = 183\,\mathrm{GeV}$	$\frac{\mathrm{d}\sigma_i - \mathrm{d}\sigma_{\mathrm{Born}}}{\mathrm{d}\sigma_{\mathrm{Born}}}[\%]$	$\sqrt{s} = 189\,\mathrm{GeV}$	$\frac{\mathrm{d}\sigma_i - \mathrm{d}\sigma_{\mathrm{Born}}}{\mathrm{d}\sigma_{\mathrm{Born}}}[\%]$
$\sigma_{\mathrm{had}}^{\mathrm{Born}}/\,\mathrm{nb}$	0.0232520(7)		0.0213084(6)	
$\sigma_{\mathrm{had}}^{\mathrm{weak}}/\,\mathrm{nb}$	0.0232558(7)	0.02	0.0213189(6)	0.02
$\sigma_{\mathrm{had}}^{\mathrm{NLO}}/\,\mathrm{nb}$	0.020766(6)	−10.7	0.019020(5)	−10.7
$\sigma_{\mathrm{had}}^{\mathrm{NLO+h.o.LL}}/\,\mathrm{nb}$	0.020660(6)	−11.1	0.018926(5)	−11.2

	$\sqrt{s} = 200\,\mathrm{GeV}$	$\frac{\mathrm{d}\sigma_i - \mathrm{d}\sigma_{\mathrm{Born}}}{\mathrm{d}\sigma_{\mathrm{Born}}}[\%]$	$\sqrt{s} = 206\,\mathrm{GeV}$	$\frac{\mathrm{d}\sigma_i - \mathrm{d}\sigma_{\mathrm{Born}}}{\mathrm{d}\sigma_{\mathrm{Born}}}[\%]$
$\sigma_{\mathrm{had}}^{\mathrm{Born}}/\,\mathrm{nb}$	0.0183779(5)		0.0170486(5)	
$\sigma_{\mathrm{had}}^{\mathrm{weak}}/\,\mathrm{nb}$	0.0183928(5)	0.1	0.0170626(5)	0.1
$\sigma_{\mathrm{had}}^{\mathrm{NLO}}/\,\mathrm{nb}$	0.016390(5)	−10.8	0.015197(4)	−10.9
$\sigma_{\mathrm{had}}^{\mathrm{NLO+h.o.LL}}/\,\mathrm{nb}$	0.016313(5)	−11.2	0.015127(4)	−11.3

	$\sqrt{s} = 500\,\mathrm{GeV}$	$\frac{\mathrm{d}\sigma_i - \mathrm{d}\sigma_{\mathrm{Born}}}{\mathrm{d}\sigma_{\mathrm{Born}}}[\%]$	$\sqrt{s} = 1000\,\mathrm{GeV}$	$\frac{\mathrm{d}\sigma_i - \mathrm{d}\sigma_{\mathrm{Born}}}{\mathrm{d}\sigma_{\mathrm{Born}}}[\%]$
$\sigma_{\mathrm{had}}^{\mathrm{Born}}/\,\mathrm{nb}$	0.00241881(7)		0.00059139(2)	
$\sigma_{\mathrm{had}}^{\mathrm{weak}}/\,\mathrm{nb}$	0.00238722(7)	−1.3	0.00056838(2)	−3.9
$\sigma_{\mathrm{had}}^{\mathrm{NLO}}/\,\mathrm{nb}$	0.0020665(7)	−14.6	0.0004856(2)	−17.9
$\sigma_{\mathrm{had}}^{\mathrm{NLO+h.o.LL}}/\,\mathrm{nb}$	0.0020585(7)	−14.9	0.0004836(2)	−18.2

Table 4.1: Total hadronic cross section $\sigma_{\mathrm{had}}\,(\sqrt{s})$ for LEPI and LEPII energies, and for $\sqrt{s} = 500\,\mathrm{GeV}$ and $\sqrt{s} = 1\,\mathrm{TeV}$.

4.4 Results for the event-shape distributions and jet rates

In the following we present the results of our calculation for the three- and four-jet rates as well as for event-shape distributions as described in Sections 1.2.1 and 1.2.2. We show our findings for $\sqrt{s} = M_{\mathrm{Z}}$ as used at LEPI and the selected LEPII energies 172 GeV and 206 GeV. To stress the relevance of our work for future linear colliders, we also show results for $\sqrt{s} = 500\,\mathrm{GeV}$.

The precise size and shape of the corrections depend on the observable y in question. However, they share the common feature that $q\bar{q}\gamma$ final states contribute only in the two-jet region, typically for small values of y.

In a first step, we show our results for the distributions normalised to σ_0 for $\sqrt{s} = M_{\mathrm{Z}}$ in Figs. 4.5 and 4.6. The Born contribution is given by the A term of Eq. (1.35), while the full $\mathcal{O}(\alpha)$ corrections contain the tree-level $q\bar{q}\gamma$ contribution δ_γ and the NLO electroweak contribution δ_A of Eq. (1.35). The T, ρ, B_{T}, B_W, and C distributions are weighted by the respective variable y, evaluated at each bin centre. The relative corrections in the lower boxes are obtained by dividing the respective contributions to the corrections by the Born distribution given by the A term. We observe large negative corrections due to ISR, and moderate weak corrections in all distributions. The corrections are mainly constant for large y (note that we plot $1 - T$ instead of T), where the isolated photon veto rejects all contributions from $q\bar{q}\gamma$ final states. Near the two-jet limit, the contribution from $q\bar{q}\gamma$ final states dominates the relative corrections. Moreover, it turns out that the electromagnetic corrections depend non-trivially on the event-selection cuts (see Section 4.5 for a more detailed discussion). We observe a significant decrease from the second bin to the first bin in all distributions, caused by the lower cut-off that we impose individually for all distributions. Since the cut-off acts both in the Born and the NLO contribution, we find a meaningful result for the relative corrections in the first bin. In the Y_3 distribution we clearly see the onset of the $q\bar{q}\gamma$ final states for $Y_3 = 0.002$. Since we always cluster photons with $y < y_{\mathrm{cut}} = 0.002$ in the event selection (see Section 3.2), the contribution from $q\bar{q}\gamma$ final states is removed if $Y_3 > 0.002$ and only plays a role for $Y_3 < 0.002$.

In expanding the corrections according to Eq. (1.36), and retaining only terms up to LO in α_{s}, we obtain the genuine electroweak corrections to normalised event-shape distributions, which we display at $\sqrt{s} = M_{\mathrm{Z}}$ in Figs. 4.7 and 4.8. The Born contribution is given by the A term of Eq. (1.36), while the $\mathcal{O}(\alpha)$ corrections are now given by δ_{EW} of Eq. (1.37). It can be seen very clearly that the large ISR corrections cancel between the event-shape distributions and the hadronic cross section when expanding the normalised distributions properly, resulting in electroweak corrections of a few per-cent. Moreover, effects from ISR resummation are largely reduced as well. The purely weak corrections are below the per-mille level.

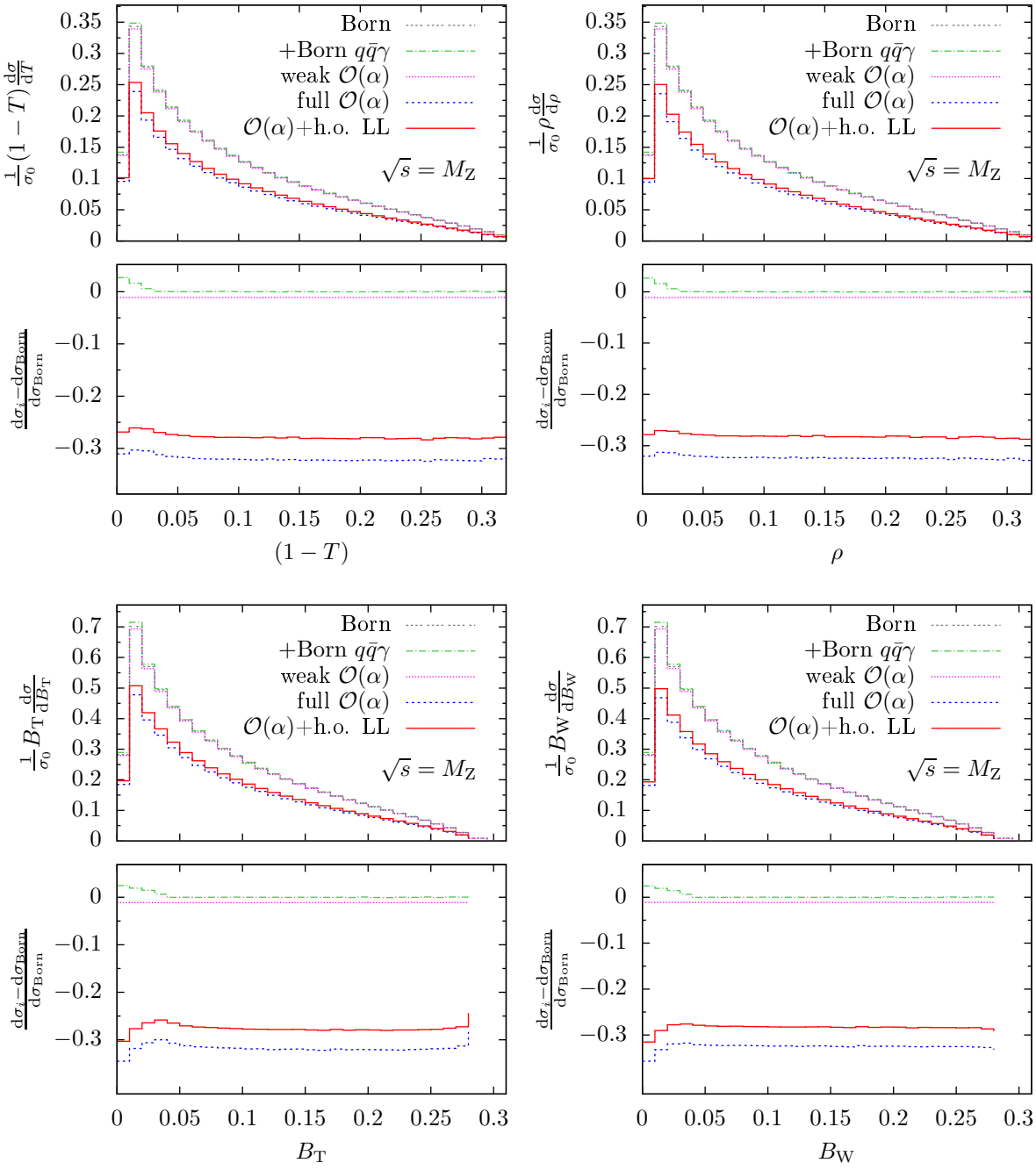

Figure 4.5: The T, ρ, B_T, B_W distributions normalised to σ_0 at $\sqrt{s} = M_Z$.

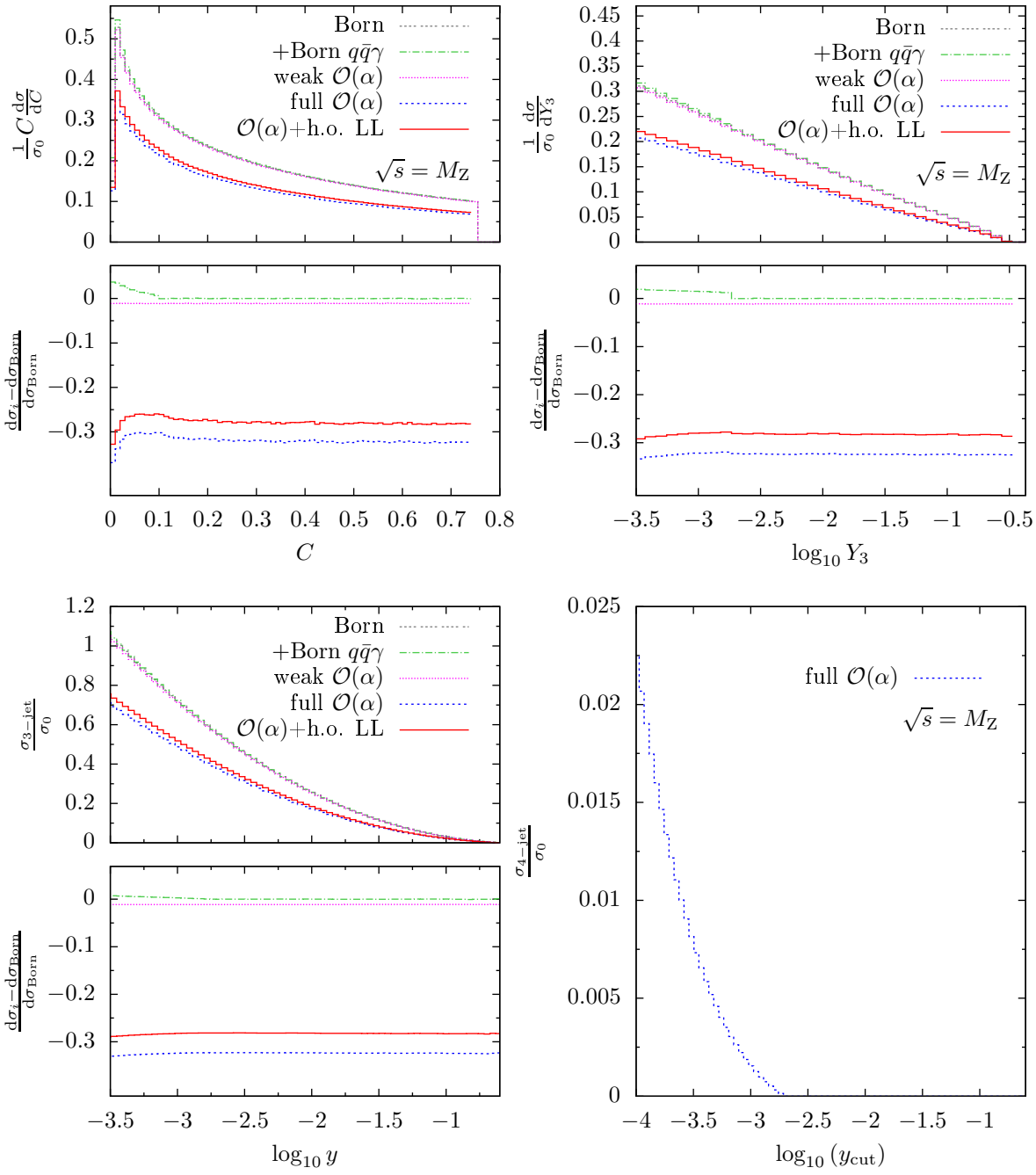

Figure 4.6: The C, and Y_3 distributions, as well as the three- and four-jet rates normalised to σ_0 at $\sqrt{s} = M_Z$.

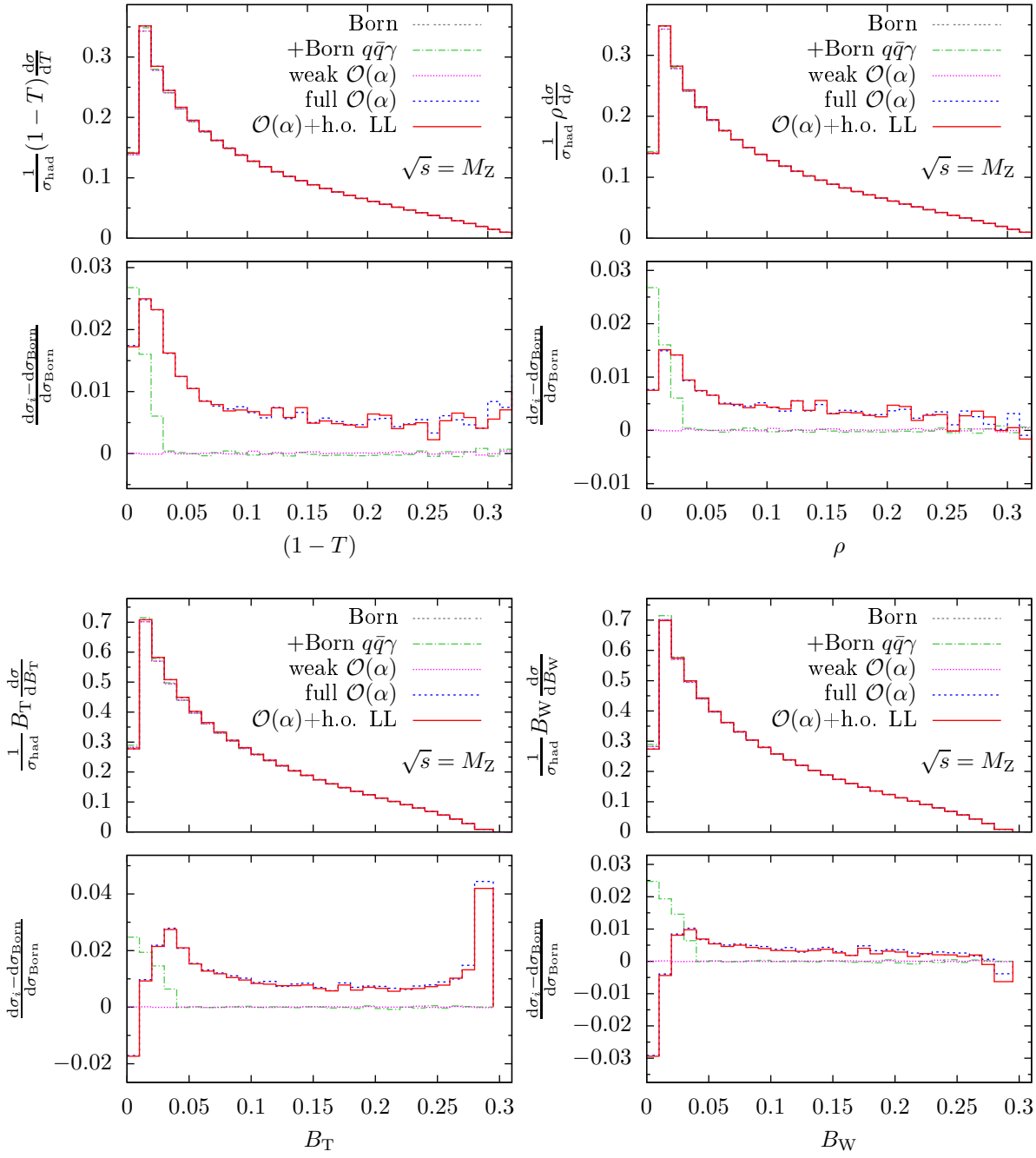

Figure 4.7: The T, ρ, B_T, B_W distributions normalised to σ_{had} at $\sqrt{s} = M_Z$.

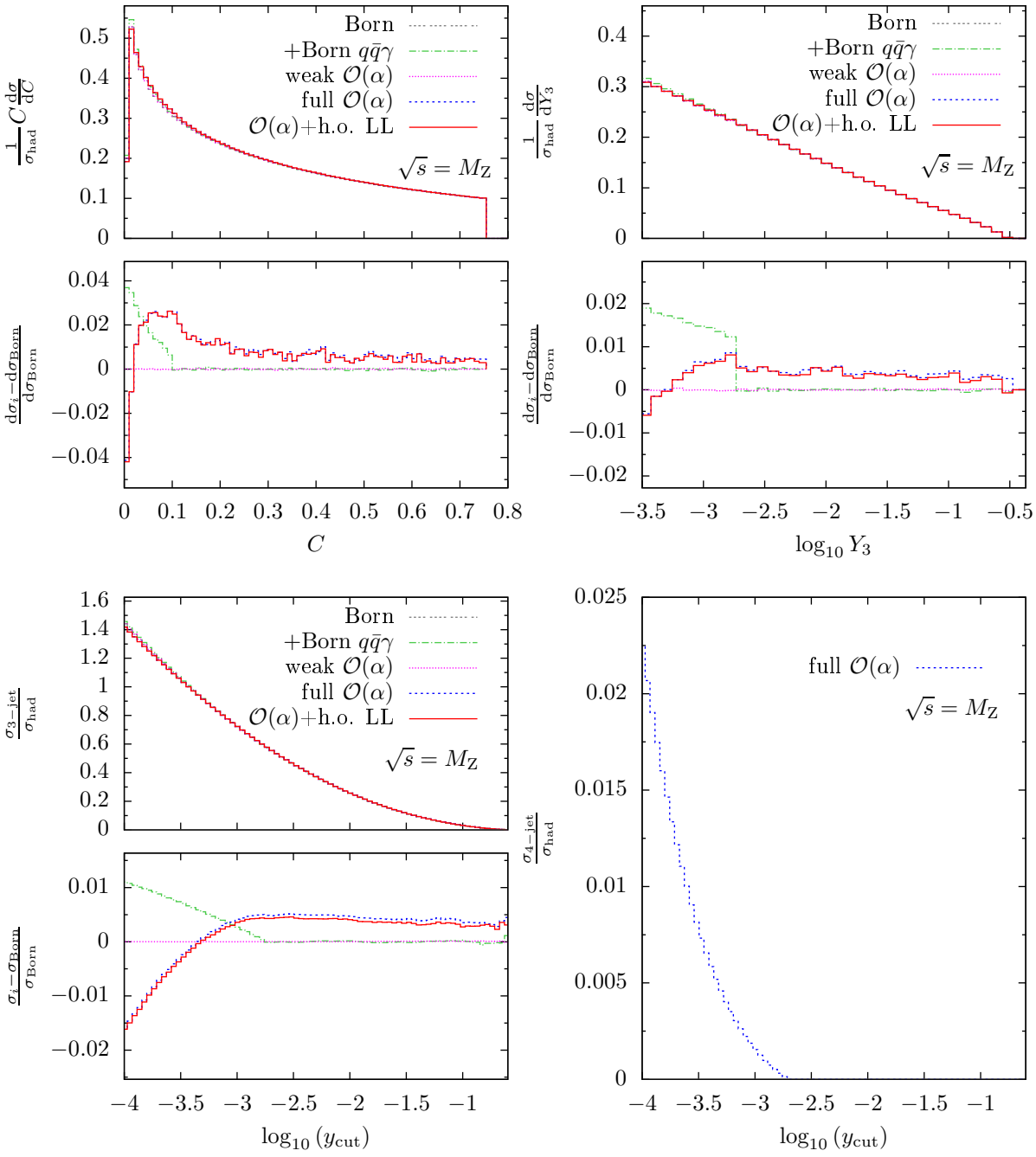

Figure 4.8: The C and Y_3 distributions, as well as the three- and four-jet rates normalised to σ_{had} at $\sqrt{s} = M_Z$.

For the thrust distribution, the full $\mathcal{O}(\alpha)$ corrections are almost constant around 0.5% for $(1-T) > 0.05$. The coefficient δ_γ starts to emerge for $(1-T) = 0.04$ and contributes up to 2.6%. The full $\mathcal{O}(\alpha)$ corrections peak for $(1-T) = 0.02$ at 2.5% and amount to 1.8% for $(1-T) = 0.01$ in the first bin. The maximum of the LO $q\bar{q}\gamma$ contribution in the ρ distribution is given by 2.6% for $\rho = 0.01$. For $\rho > 0.05$, the full $\mathcal{O}(\alpha)$ corrections are flat and around 0.5%, whereas they reach their maximum of 1.5% for $\rho = 0.02$ and drop to 0.8% in the first bin. The full $\mathcal{O}(\alpha)$ corrections of the B_T distribution are around 1% and almost flat for $B_\mathrm{T} > 0.05$. In the last bin, however, they amount to 4%. The coefficient δ_γ starts to emerge for $B_\mathrm{T} = 0.04$ and contributes up to 2.5% for $B_\mathrm{T} = 0.01$. The full $\mathcal{O}(\alpha)$ corrections show a peak of 2.9% at $B_\mathrm{T} = 0.04$ and drop to -1.9% in the first bin. The maximum of the LO $q\bar{q}\gamma$ contribution in the B_W distribution is given by 2.5% for $B_W = 0.01$. For $B_W > 0.05$, the full $\mathcal{O}(\alpha)$ corrections are flat and around 0.5%, whereas they reach their maximum of 1% for $B_W = 0.04$ and drop to -3% in the first bin. For the distribution in C, the full $\mathcal{O}(\alpha)$ corrections are almost constant around 0.5% for $C > 0.1$. The coefficient δ_γ starts to emerge for $C = 0.09$ and contributes up to 3.9%. The full $\mathcal{O}(\alpha)$ corrections peak for $C = 0.1$ at 2.9% and amount to -4.1% for $C = 0.01$ in the first bin. The maximum of the LO $q\bar{q}\gamma$ contribution in the Y_3 distribution is given by 2% for small Y_3. For $Y_3 > 0.002$, the full $\mathcal{O}(\alpha)$ corrections are flat and around 0.5%, whereas they reach their maximum of 0.9% for $Y_3 = 0.002$ and drop to -0.6% in the first bin. The full $\mathcal{O}(\alpha)$ corrections to the three-jet rate are about 0.5% for $y_\mathrm{cut} \gtrsim 0.002$. Because we use $y_\mathrm{cut} = 0.002$ in the event selection, $q\bar{q}\gamma$ final states contribute only if $y_\mathrm{cut} \lesssim 0.002$. The LO $q\bar{q}\gamma$ contribution amounts to 1%. For $y_\mathrm{cut} < 0.002$, the full $\mathcal{O}(\alpha)$ corrections become negative, reaching -1.5% in the first bin. For $y_\mathrm{cut} \lesssim 0.0005$ the three-jet rate becomes larger than σ_had. However, higher-order QCD corrections are large and negative [52, 111–113], such that once they are included as well, the ratio of $\sigma_{3-\mathrm{jet}}$ to σ_had is always less than unity. In our calculation, the four-jet rate receives only contributions from $q\bar{q}\mathrm{g}\gamma$ final states. Again, because of the value of y_cut in the event selection, it is different from zero only for $y_\mathrm{cut} \lesssim 0.002$. In Ref. [114], numerical results for the four-jet rate R_4 are presented. In $\mathcal{O}\left(\alpha^2\alpha_\mathrm{s}^2\right)$ and for $\log\left(y_\mathrm{cut}\right) = -3$ they find $R_4(0.001, M_\mathrm{Z}) = 0.35$. In $\mathcal{O}\left(\alpha^3\alpha_\mathrm{s}\right)$, we find $R_4(0.001, M_\mathrm{Z}) = 0.0015$, which is a 0.5% correction to the LO QCD result.

In Figs. 4.9 and 4.10 we show our results for $\sqrt{s} = 172\,\mathrm{GeV}$. We observe a similar behaviour as for $\sqrt{s} = M_\mathrm{Z}$. However, we now observe a peaking structure in the middle of the distributions. It is located at $1-T, \rho, B_\mathrm{W} \approx 0.2$, $B_\mathrm{T} \approx 0.25$, $C \approx 0.65$, $Y_3 \approx 0.8$, and $\log_{10}\left(y_\mathrm{cut}\right) \approx -1$. We investigate this behaviour in greater detail in the next section. In all event-shape distributions the LO $q\bar{q}\gamma$ contribution ranges between 3% and 8%. Outside the two-jet region and outside the domain where the peaking structure is located, the full $\mathcal{O}(\alpha)$ corrections are flat between 0.5% and 5%, they peak near the onset of the $q\bar{q}\gamma$ final states between 4% and 10%, and drop in the first bin down to between 1.5% and -10%. In the three-jet rate, the full $\mathcal{O}(\alpha)$ corrections are almost constant and range between 2.5% and 5% for $y_\mathrm{cut} > 0.002$. In the region $y_\mathrm{cut} < 0.002$,

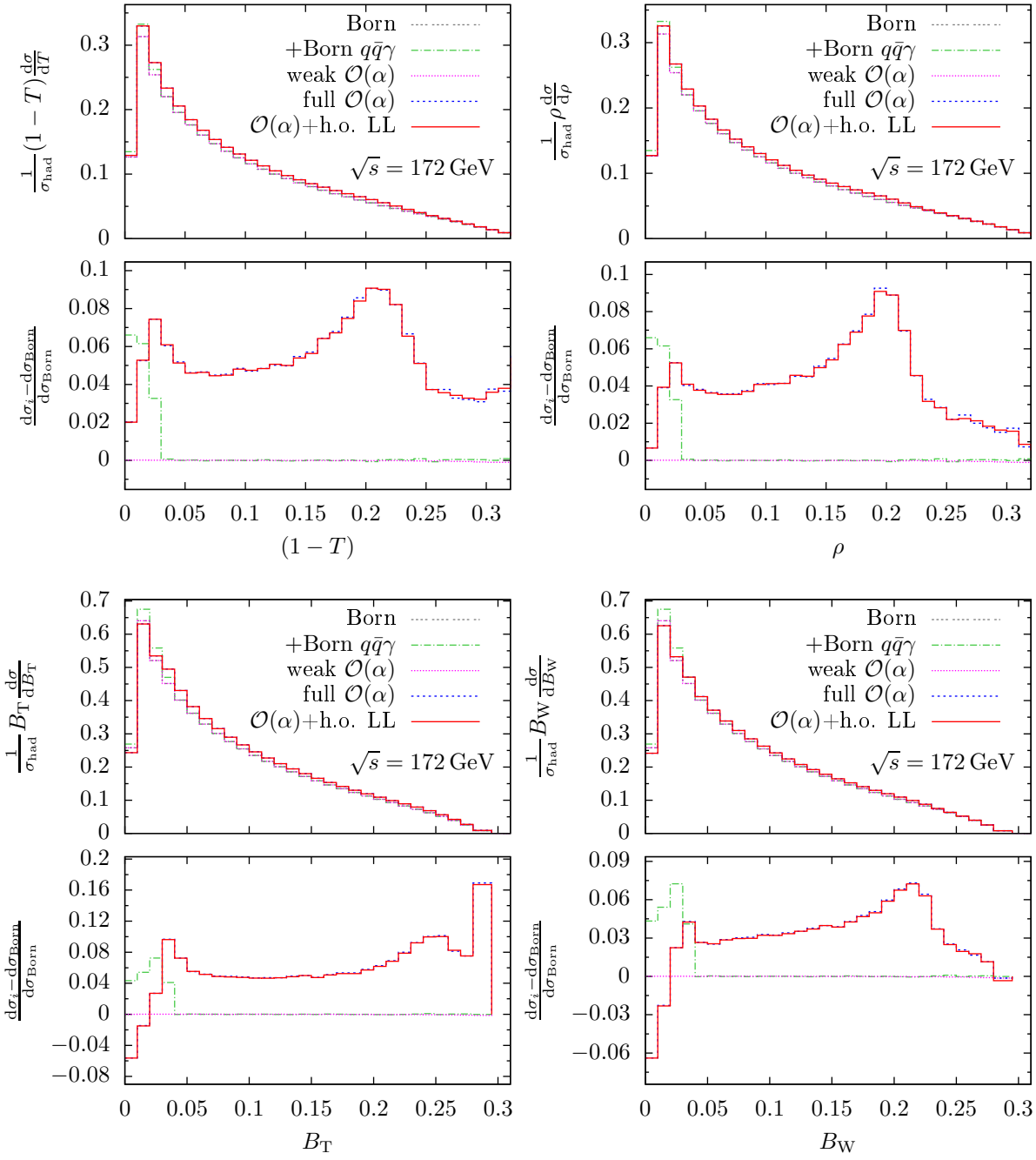

Figure 4.9: The T, ρ, B_{T}, B_W distributions normalised to σ_{had} at $\sqrt{s} = 172\,\mathrm{GeV}$.

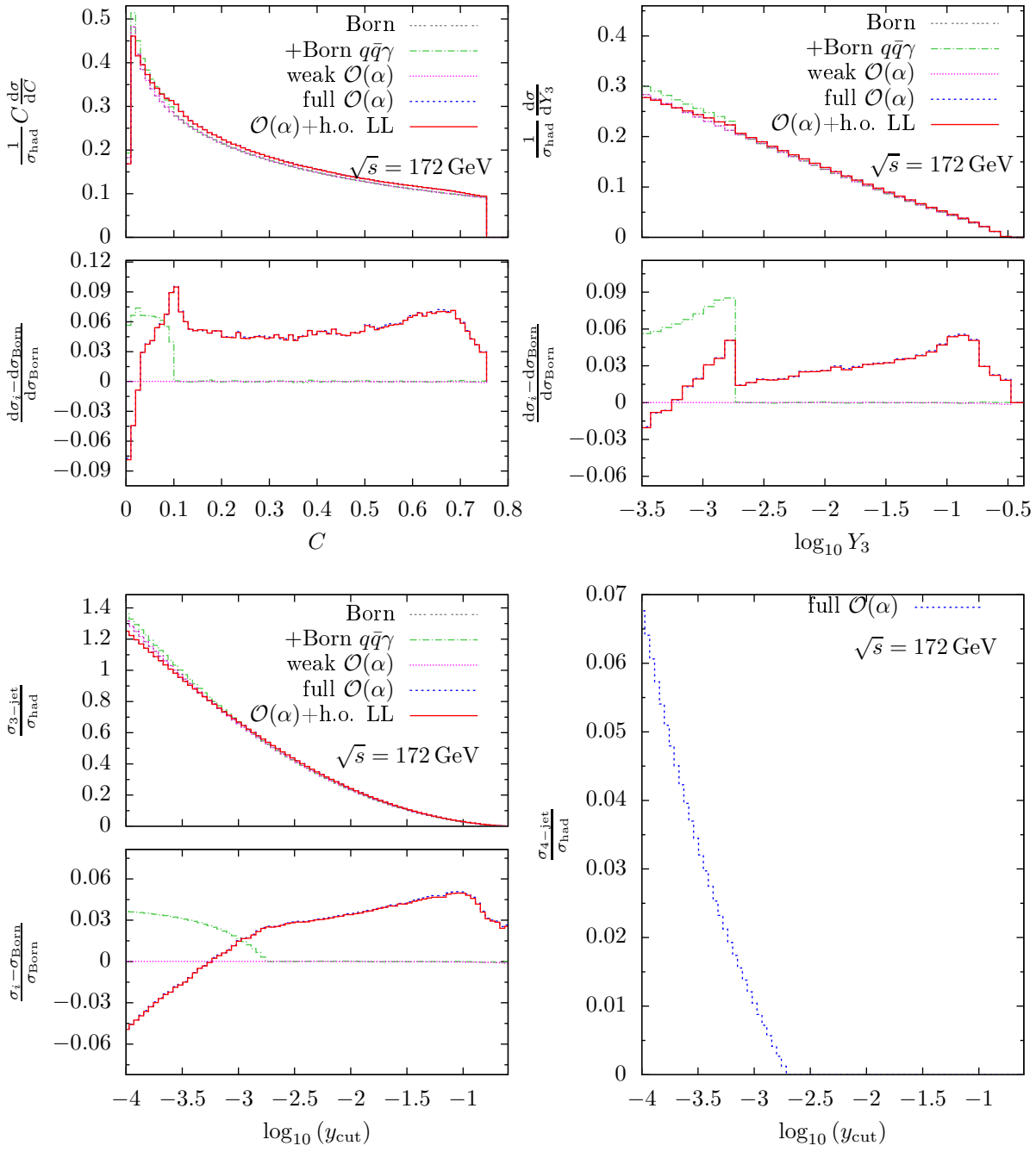

Figure 4.10: The C and Y_3 distributions, as well as the three- and four-jet rates normalised to σ_{had} at $\sqrt{s} = 172\,\mathrm{GeV}$.

we find a negative contribution of -6% for very small values of $y_{\rm cut}$.

We now come to our results for $\sqrt{s} = 206\,\text{GeV}$, which we show in Figs. 4.11 and 4.12. In all event-shape distributions the LO $q\bar{q}\gamma$ contribution ranges between 4% and 9%. Outside the two-jet region and outside the domain where the peaking structure is located, the full $\mathcal{O}(\alpha)$ corrections are flat between 0.1% and 2%, they peak near the onset of the $q\bar{q}\gamma$ final states between 5% and 9%, and drop in the first bin down to between 2% and -8%. In the three-jet rate, the full $\mathcal{O}(\alpha)$ corrections are almost constant and range between 1% and 2% for $y_{\rm cut} > 0.002$. In the region $y_{\rm cut} < 0.002$, we find a negative contribution of -5% for very small values of $y_{\rm cut}$. In Ref. [52], the four-jet rate at $\sqrt{s} = 206\,\text{GeV}$ in $\mathcal{O}\left(\alpha^2\alpha_{\rm s}^2\right)$ and for $\log\left(y_{\rm cut}\right) = -3$ has been given as $R_4(0.001, 206\,\text{GeV}) = 0.2$. In $\mathcal{O}\left(\alpha^3\alpha_{\rm s}\right)$, we find $R_4(0.001, 206\,\text{GeV}) = 0.01$ which amounts to a 5% correction to the LO QCD result. The peaking structure is now situated at smaller values of y and, especially for $B_{\rm W}$, $B_{\rm T}$, C, and Y_3, it extends over a larger range of y. Additionally, for large values of y, the weak contribution slightly increases.

Finally, in Figs. 4.13 and 4.20 we show our results for $\sqrt{s} = 500\,\text{GeV}$. In the event-shape distributions the LO $q\bar{q}\gamma$ contribution ranges between 2% and 9%. Outside the two-jet region, the full $\mathcal{O}(\alpha)$ corrections are flat between 2% and 3%, they peak near the onset of the $q\bar{q}\gamma$ final states between 2% and 9%, and drop in the first bin down to between 2% and -6%. In the three-jet rate, the full $\mathcal{O}(\alpha)$ corrections are almost constant and range between 2% and 3% for $y_{\rm cut} > 0.002$. In the region $y_{\rm cut} < 0.002$, we find a negative contribution of -4% for very small values of $y_{\rm cut}$. The weak corrections here contribute up to $+1\%$ in all observables for large values of y. The peaking structure as observed for $\sqrt{s} = 172\,\text{GeV}$ and $\sqrt{s} = 206\,\text{GeV}$ has completely disappeared.

4.5 Effects of the event-selection cuts on the event-shape distributions

In this section we discuss the effects of the event-selection cuts, especially the hard-photon cut, on the event-shape distributions using thrust as an example. In Figs. 4.9 and 4.10, we see that the relative corrections show a peaking structure for $1 - T \approx 0.2$. In the following we investigate how the event-selection cuts influence this peaking structure.

We employ a total of three different cuts in our calculation which depend on four parameters:

1) A cut on the production angle θ of all particles, such that only particles i with $\cos\theta_i < \cos\theta_{\rm cut}$ are used in the reconstruction of the event-shape variable. By default, we use the value $\cos\theta_{\rm cut} = 0.965$.

2) A cut on the visible energy squared of the final state s', such that only events

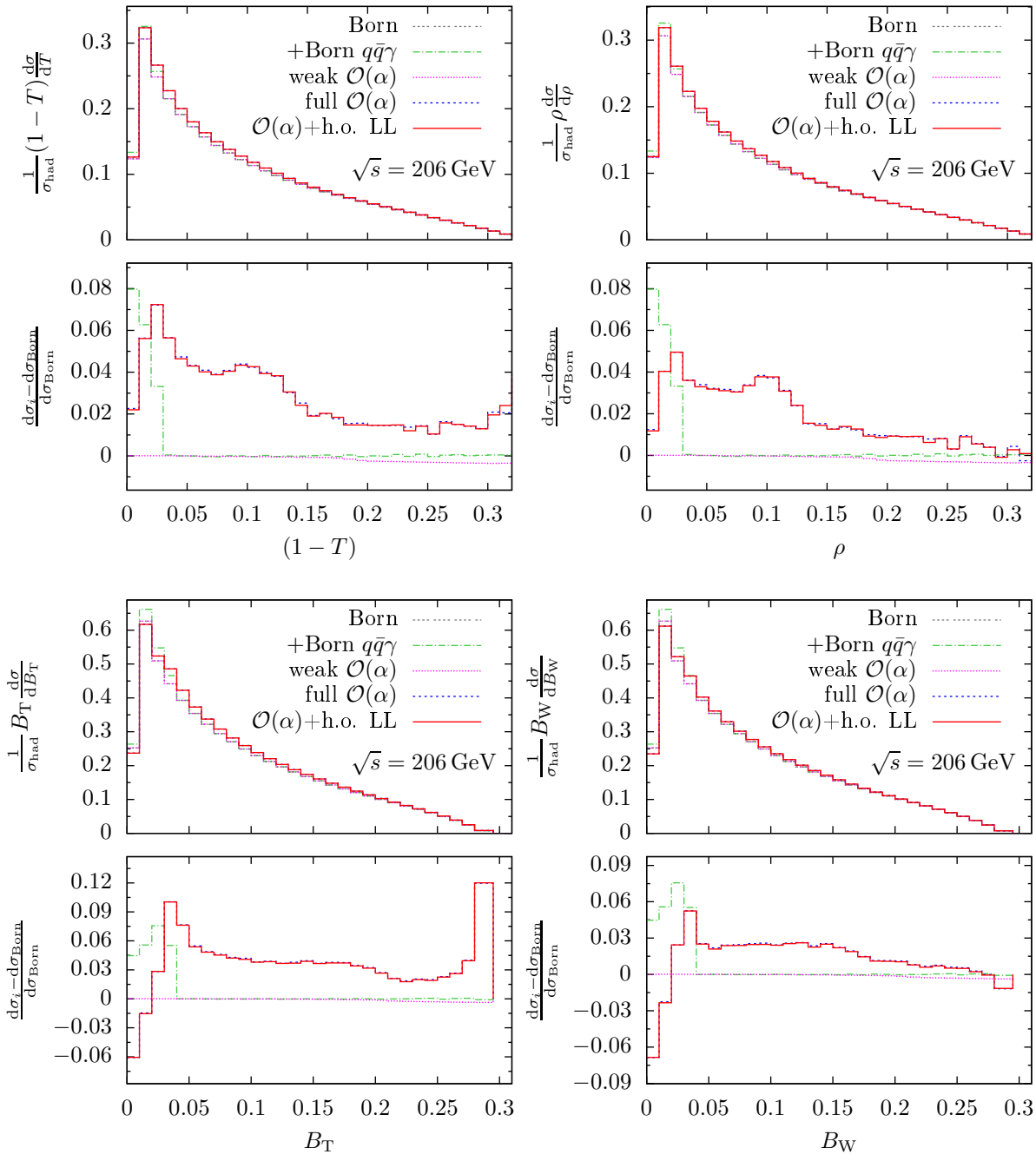

Figure 4.11: The T, ρ, B_{T}, B_W distributions normalised to σ_{had} at $\sqrt{s} = 206\,\mathrm{GeV}$.

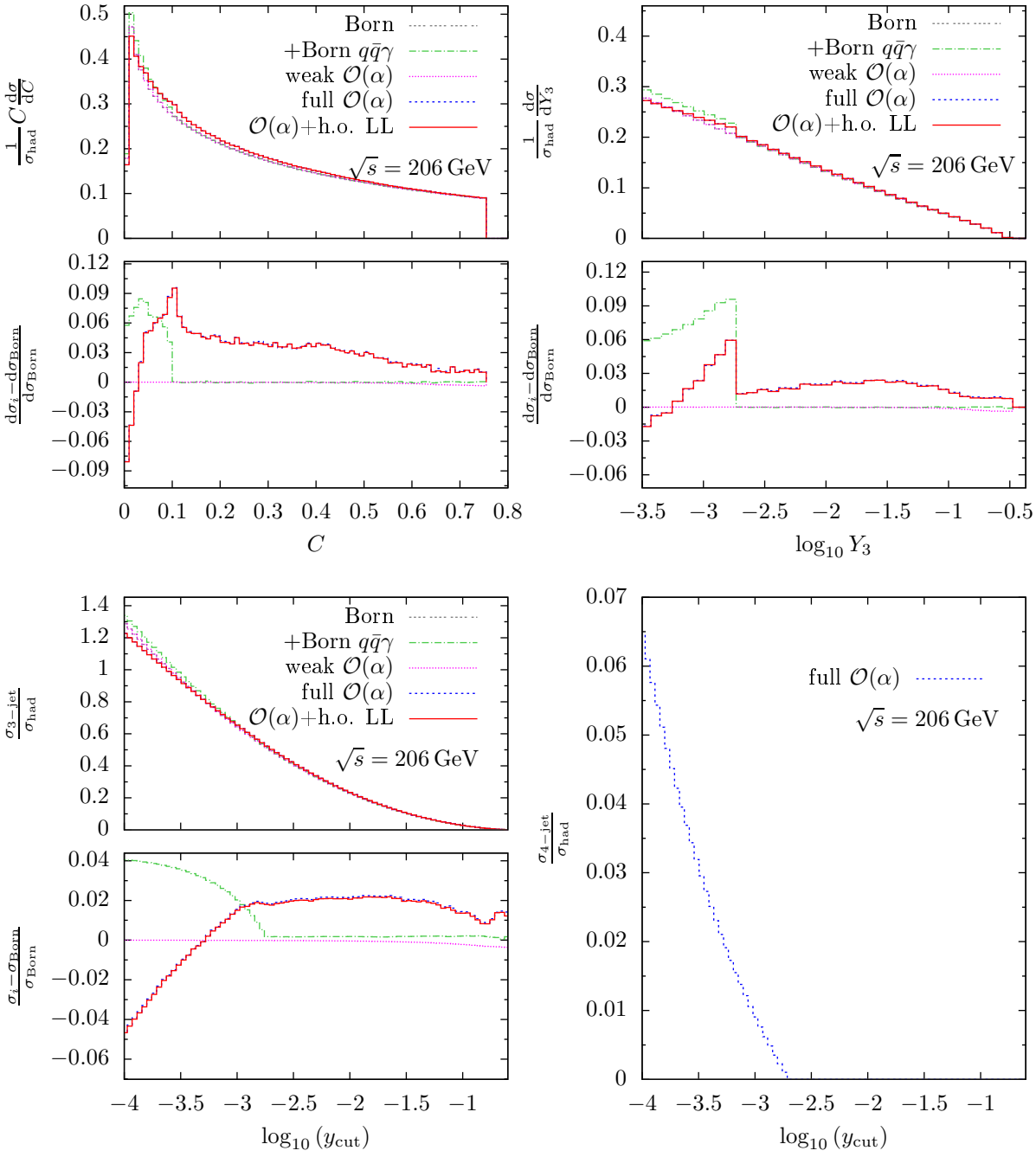

Figure 4.12: The C and Y_3 distributions, as well as the three- and four-jet rates normalised to σ_{had} at $\sqrt{s} = 206\,\mathrm{GeV}$.

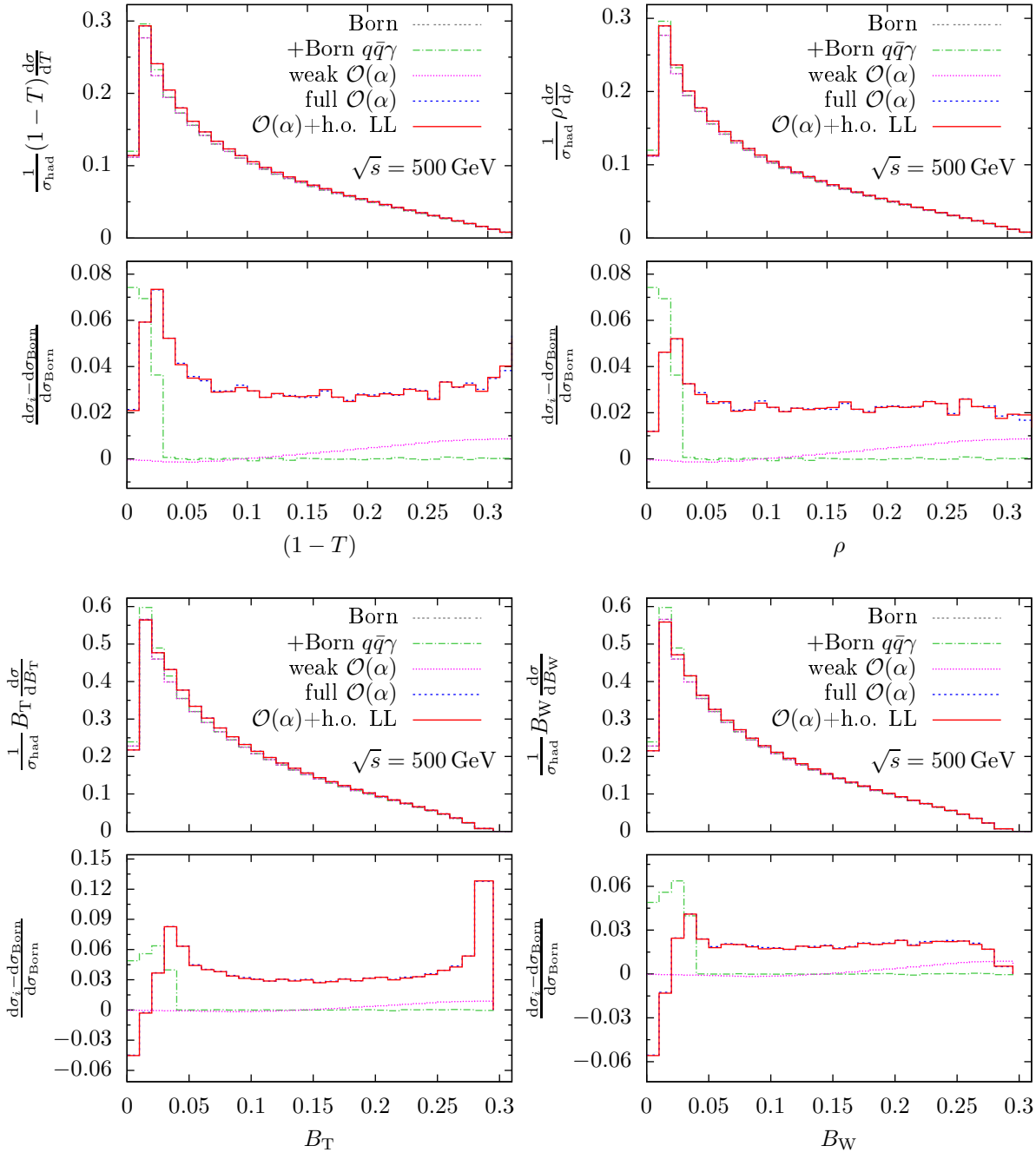

Figure 4.13: The T, ρ, B_{T}, B_W distributions normalised to σ_{had} at $\sqrt{s} = 500\,\mathrm{GeV}$.

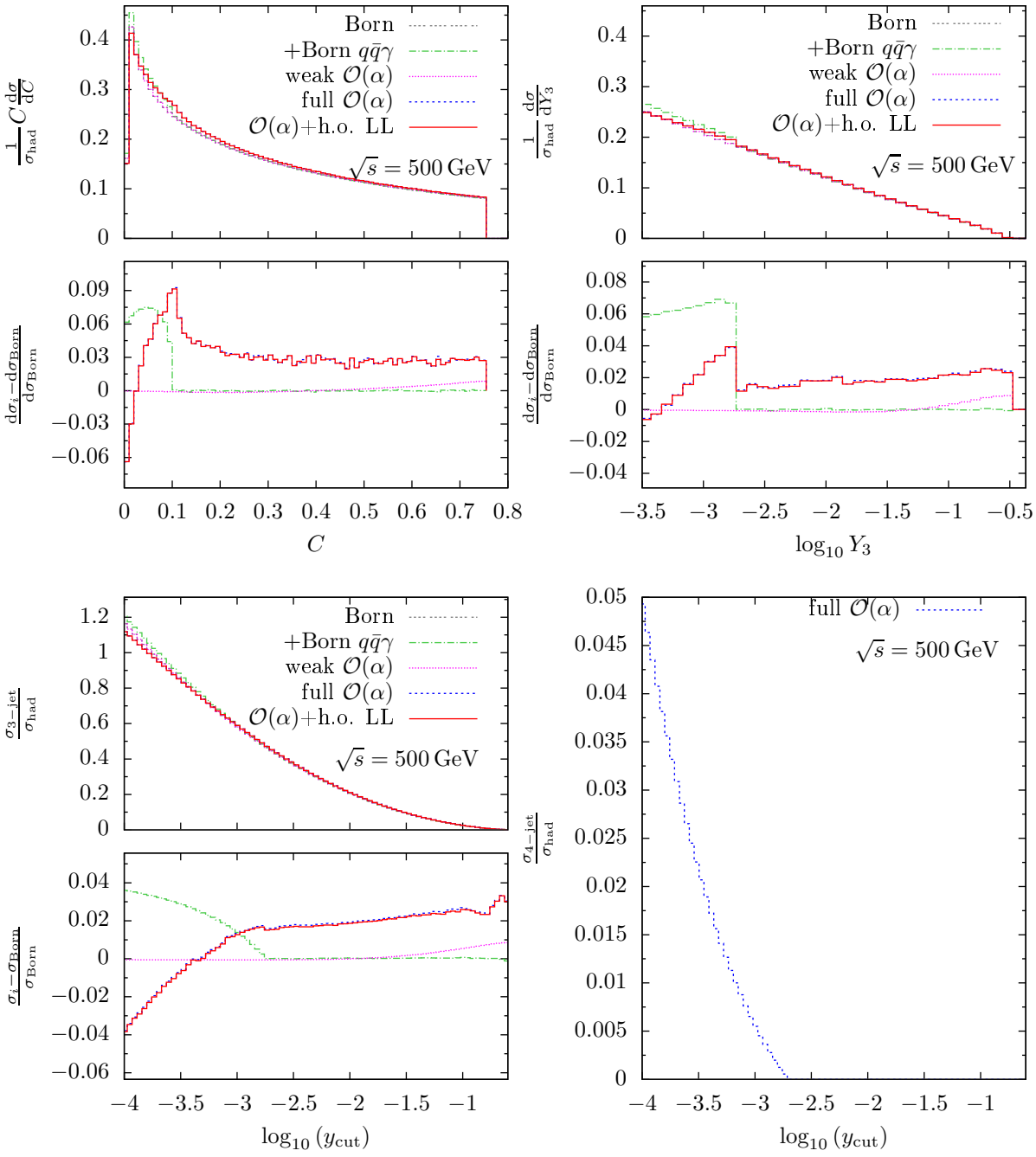

Figure 4.14: The C and Y_3 distributions distributions, as well as the three- and four-jet rates normalised to σ_had at $\sqrt{s} = 500\,\text{GeV}$.

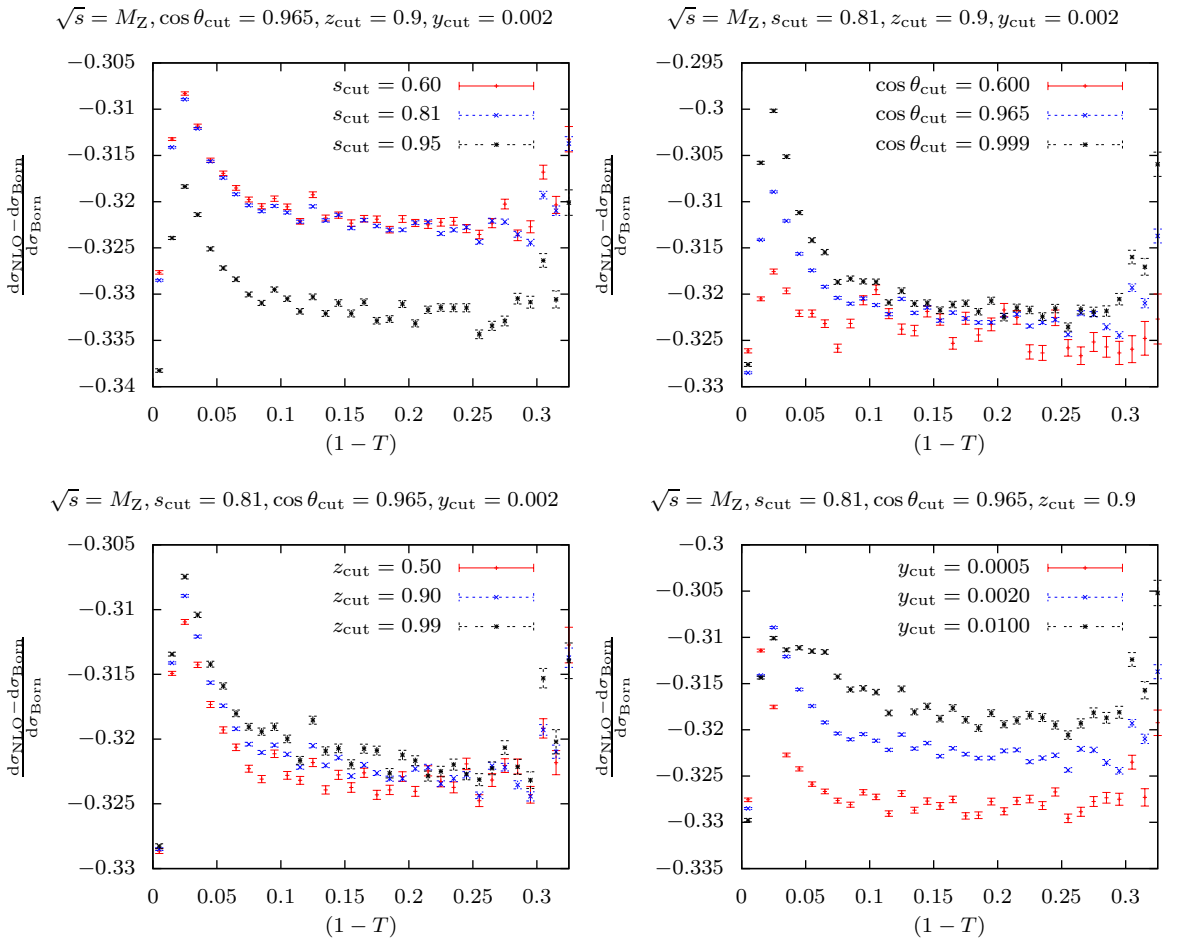

Figure 4.15: Dependence of the thrust distribution on different values of the phase space cuts at $\sqrt{s} = M_Z$.

with $s'/s > s_{cut}$ are accepted. By default, we use the value $s_{cut} = 0.81$.

3) The maximum photon energy in a jet z is restricted to be $z < z_{cut}$, where the particles are clustered according to the Durham jet algorithm with parameter y_{cut}. By default, we use the values $z_{cut} = 0.9$ and $y_{cut} = 0.002$.

In the following we show the full $\mathcal{O}(\alpha)$ corrections to the thrust distribution normalised to the Born contribution for $\sqrt{s} = M_Z$, 133 GeV, 172 GeV, 206 GeV, and 500 GeV. We plot the results for three different values of a single parameter while we set the other three parameters to their default value. Going from left to right and top to bottom, we vary s_{cut}, $\cos\theta_{cut}$, z_{cut}, and y_{cut} in Fig. 4.15 for $\sqrt{s} = M_Z$. By varying s_{cut} we observe a change in normalisation of about 1%, while the shape of the distribution stays the same. Varying $\cos\theta_{cut}$ and z_{cut} leaves the distribution unchanged for $1 - T > 0.05$. For

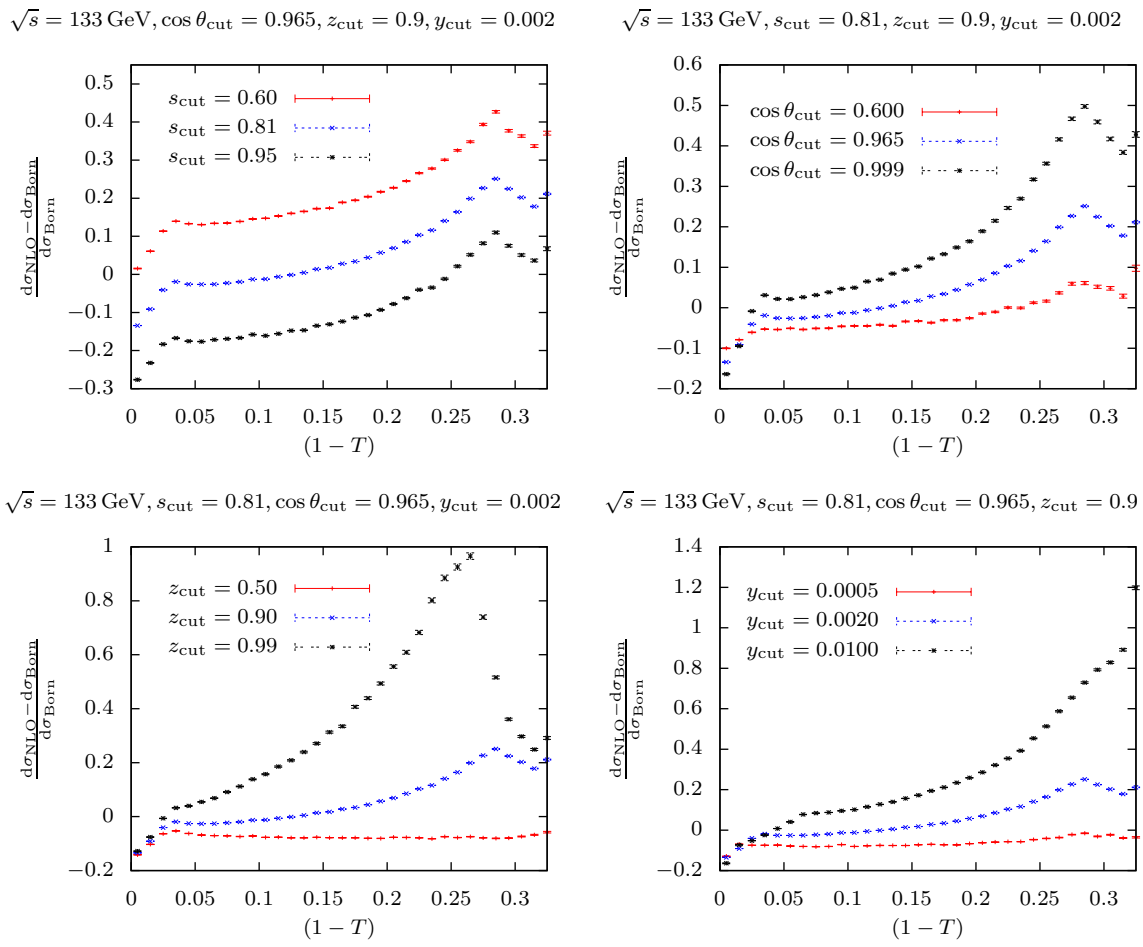

Figure 4.16: Dependence of the thrust distribution on different values of the phase space cuts at $\sqrt{s} = 133\,\mathrm{GeV}$.

$1-T \leq 0.05$ increasing both parameters causes a larger acceptance of ISR photons that leads to an increase of the NLO contribution of about 2%. By varying y_{cut}, we see that for larger values of this parameter the contribution of $q\bar{q}\gamma$ final states is extended to a larger region of $1 - T$. While for $y_{\mathrm{cut}} = 0.0005$ this region is given by $1 - T < 0.025$, it is given by $1 - T < 0.075$ for $y_{\mathrm{cut}} = 0.01$. For this value of y_{cut}, we can also see a plateau for $0.025 < 1 - T < 0.075$. For $1 - T < 0.025$, the NLO QCD corrections are large and negative, causing the steep decrease in the first three bins.

In Fig. 4.16 we show the results for the same procedure as described above for $\sqrt{s} = 133\,\mathrm{GeV}$. Varying s_{cut} from 0.6 to 0.95 only leads to a change in normalisation of about 30%, while the shape of the distribution stays the same. Varying $\cos\theta_{\mathrm{cut}}$ from larger to smaller values leads to a steeper decrease of the distribution in the region $1 - T < 0.03$. This can again be explained through the larger acceptance of ISR

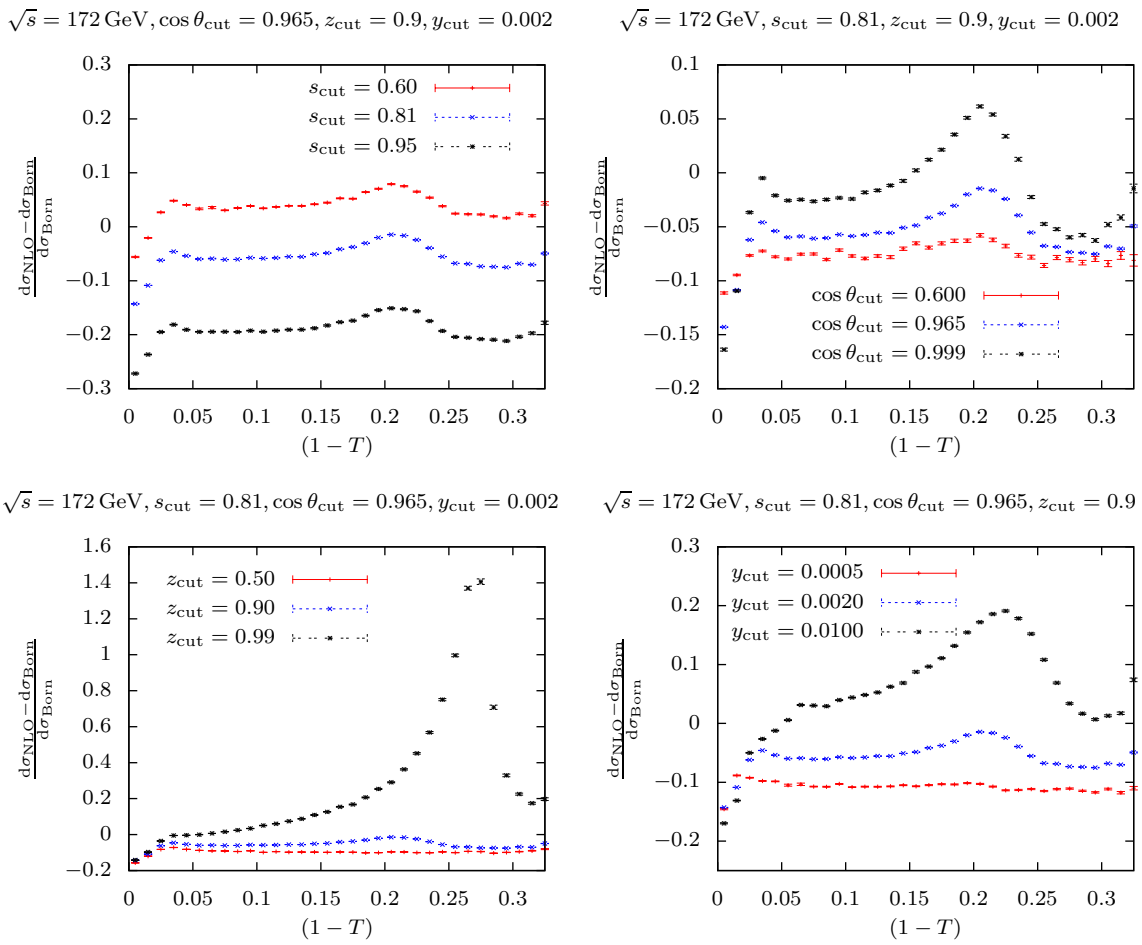

Figure 4.17: Dependence of the thrust distribution on different values of the phase space cuts at $\sqrt{s} = 172\,\mathrm{GeV}$.

photons. However, we see that a peaking structure at $1 - T \approx 0.28$ emerges, enhancing the corrections by about 50%. By changing z_{cut} from 0.5 to 0.99 we see an increase of the peak by almost 100%. We also observe that it changes position from $1 - T \approx 0.28$ for $z_{\mathrm{cut}} = 0.9$ to $1 - T \approx 0.25$ for $z_{\mathrm{cut}} = 0.99$. For larger values of y_{cut} we observe an enhancement of the peak, as well as a slight shift to larger values of $1 - T$.

In Figs. 4.17 and 4.18 we notice in principle the same qualitative behaviour for $\sqrt{s} = 172\,\mathrm{GeV}$ and $\sqrt{s} = 206\,\mathrm{GeV}$. Additionally, we find that the peaking structure moves to smaller $1 - T$ with increasing energy.

For $\sqrt{s} = 500\,\mathrm{GeV}$, the distributions are flat for $1 - T \gtrsim 0.05$, and show a steeper decrease for $1 - T \lesssim 0.05$ when increasing the parameters $\cos\theta_{\mathrm{cut}}$, z_{cut}, and y_{cut}, as can be seen in Fig. 4.19. We do not observe the formation of a peaking structure as for lower energies, but only a change in normalisation.

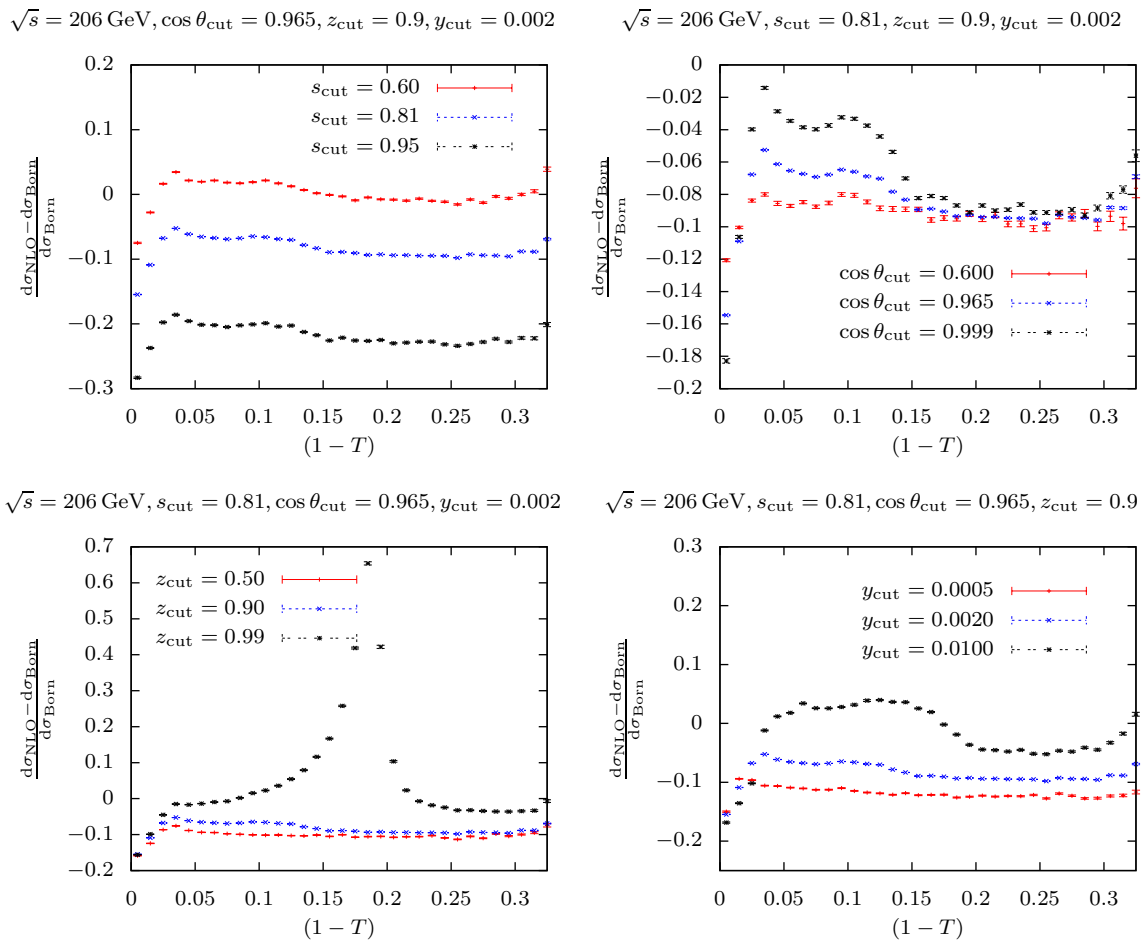

Figure 4.18: Dependence of the thrust distribution on different values of the phase space cuts at $\sqrt{s} = 206\,\mathrm{GeV}$.

Through analysing events at the level of the Monte Carlo event generator, we find that the enhancement in the region of the peaking structure always stems from $q\bar{q}g\gamma$ final states, where a soft gluon is clustered with a hard photon. Increasing $\cos\theta_{\mathrm{cut}}$ leads to a logarithmic enhancement of collinear ISR photons, increasing z_{cut} generally results in a larger acceptance of photons inside jets, and increasing y_{cut} causes more photons to be clustered together with other partons, resulting in less events with isolated photons being removed. We can therefore conclude that the peaking structure results from the ISR photon contribution, where a soft gluon is clustered together with the photon.

The peaking structure can be explained by the radiative return phenomenon. Since we do not remove all energetic photons, it is possible that a hard photon and a soft gluon are clustered together, such that the energy fraction of the photon in the jet does not exceed z_{cut} and the invariant mass of the quark–antiquark–gluon system $s_{q\bar{q}g}$

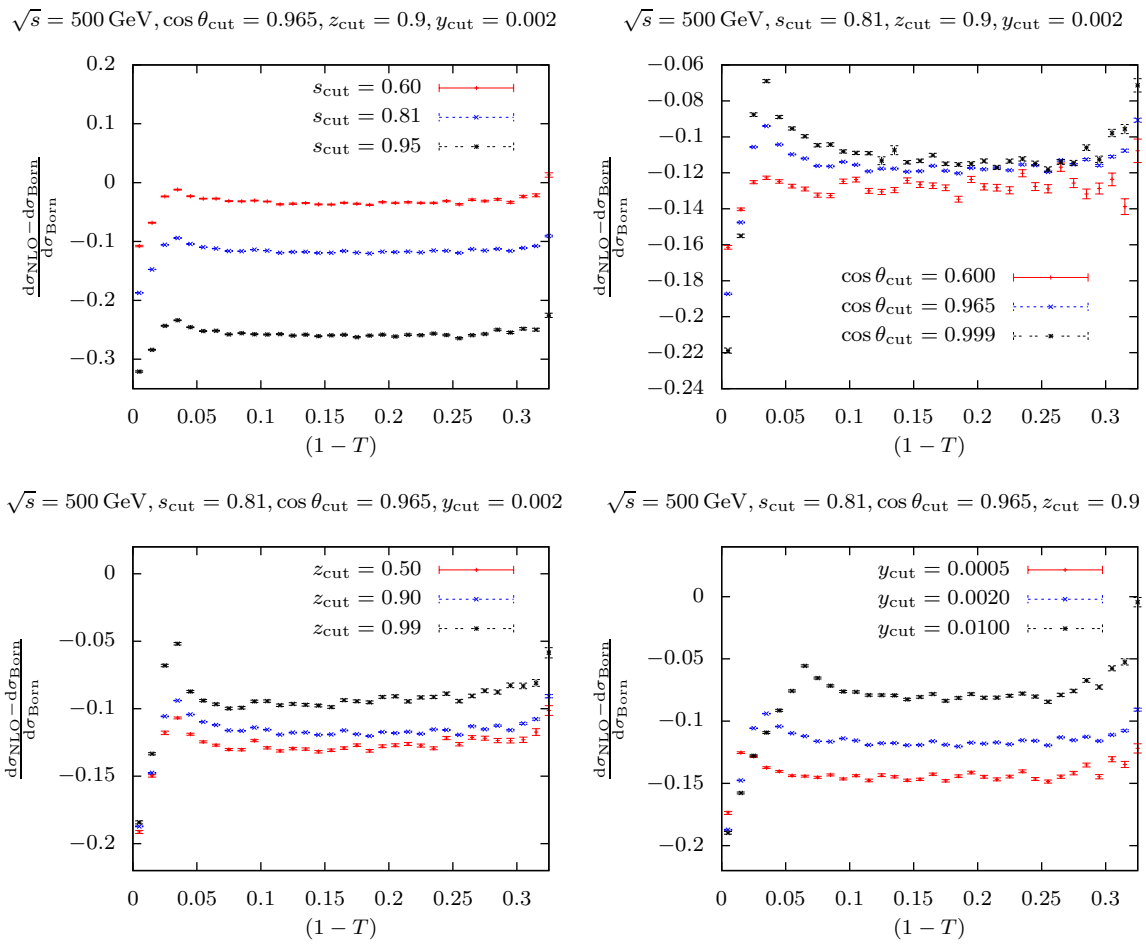

Figure 4.19: Dependence of the thrust distribution on different values of the phase space cuts at $\sqrt{s} = 500\,\mathrm{GeV}$.

is equal to the mass of the Z boson. Such a configuration leads on the one hand to an enhancement due to radiative return but also to a logarithmic enhancement due to the soft gluon.

In the following, we assume that the photon and the gluon are clustered together, such that we only have to consider a three-particle final state that consists of a quark, an antiquark, and a photonic jet. Assume that the quark, antiquark, and the photonic jet have the three-momenta $\vec{p}_q, \vec{p}_{\bar{q}}, \vec{p}_\gamma$ and the energies $E_q, E_{\bar{q}}, E_\gamma$, respectively. From energy-momentum conservation we know that

$$\begin{aligned} \vec{p}_q + \vec{p}_{\bar{q}} + \vec{p}_\gamma &= 0, \\ E_q + E_{\bar{q}} + E_\gamma &= \sqrt{s}. \end{aligned} \tag{4.5}$$

Furthermore, we demand that the invariant mass of the quark–antiquark pair is equal

to M_{Z}, such that

$$s_{q\bar{q}} = (E_q + E_{\bar{q}})^2 - (\vec{p}_q + \vec{p}_{\bar{q}})^2 = (E_q + E_{\bar{q}})^2 - (\vec{p}_\gamma)^2 = (E_q + E_{\bar{q}})^2 - E_\gamma^2 = M_{\mathrm{Z}}^2. \quad (4.6)$$

Replacing $E_q + E_{\bar{q}}$ by x and E_γ by y we find the system of equations

$$\begin{aligned} x^2 - y^2 &= M_{\mathrm{Z}}^2, \\ x + y &= \sqrt{s}, \end{aligned} \quad (4.7)$$

which has the solution

$$x = \frac{s + M_{\mathrm{Z}}^2}{2\sqrt{s}}, \quad y = \frac{s - M_{\mathrm{Z}}^2}{2\sqrt{s}}. \quad (4.8)$$

It can be shown that in a three-jet configuration with massless partons, thrust is always determined by the energy of the most energetic particle $E_{\max}$ [115, 116], i.e.

$$T = \frac{2E_{\max}}{\sqrt{s}}. \quad (4.9)$$

If we now assume that the quark and the antiquark carry the same energy, we can calculate the energies of all three jets in the final state at different energies. We find

$$\begin{aligned} E_q\,(133\,\mathrm{GeV}) = E_{\bar{q}}\,(133\,\mathrm{GeV}) \approx 49\,\mathrm{GeV}, \quad E_\gamma\,(133\,\mathrm{GeV}) &\approx 35\,\mathrm{GeV}, \\ E_q\,(172\,\mathrm{GeV}) = E_{\bar{q}}\,(172\,\mathrm{GeV}) \approx 55\,\mathrm{GeV}, \quad E_\gamma\,(172\,\mathrm{GeV}) &\approx 62\,\mathrm{GeV}, \\ E_q\,(206\,\mathrm{GeV}) = E_{\bar{q}}\,(206\,\mathrm{GeV}) \approx 61\,\mathrm{GeV}, \quad E_\gamma\,(206\,\mathrm{GeV}) &\approx 84\,\mathrm{GeV}, \\ E_q\,(500\,\mathrm{GeV}) = E_{\bar{q}}\,(500\,\mathrm{GeV}) \approx 129\,\mathrm{GeV}, \quad E_\gamma\,(500\,\mathrm{GeV}) &\approx 242\,\mathrm{GeV}, \end{aligned} \quad (4.10)$$

which leads to the following thrust values where the radiative return phenomena should appear:

$$\begin{aligned} (1 - T_{\mathrm{RR}})(\sqrt{s} = 133) &\approx 0.27, \\ (1 - T_{\mathrm{RR}})(\sqrt{s} = 172) &\approx 0.28, \\ (1 - T_{\mathrm{RR}})(\sqrt{s} = 206) &\approx 0.19, \\ (1 - T_{\mathrm{RR}})(\sqrt{s} = 500) &\approx 0.03. \end{aligned} \quad (4.11)$$

These values coincide perfectly with the peaks in Figs. 4.16–4.19. Relaxing the assumption that the quark and the antiquark carry the same energy only leads to a broadening of the peaking structure. Varying the value of z_{cut} leads to different energies of the photonic jet and therefore changes the allowed energies in the above analysis. For decreasing values of z_{cut}, we therefore either only observe the tail of the peak or cut it away completely which effectively looks like a shift of the position or the disappearance of the peak. For $\sqrt{s} = 133\,\mathrm{GeV}$ we observe the tail of the peak for $E_q < E_{q,\mathrm{peak}}$ such that for decreasing z_{cut} the peak seems to move to larger values of $(1 - T)$. For $\sqrt{s} = 172\,\mathrm{GeV}$ and $\sqrt{s} = 206\,\mathrm{GeV}$ we observe the tail of the peak for $E_\gamma < E_{\gamma,\mathrm{peak}}$ such that for decreasing z_{cut} the peak seems to move to smaller values of $(1 - T)$.

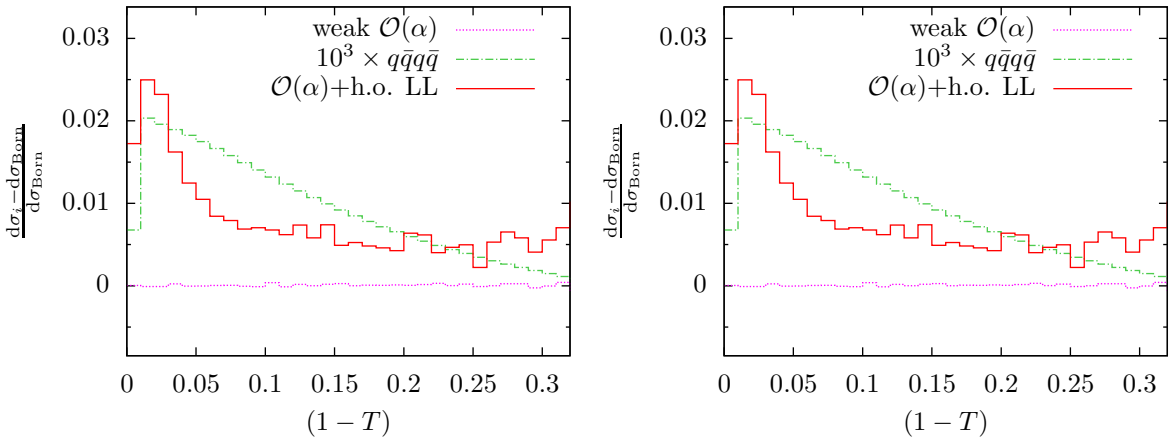

Figure 4.20: The thrust distribution including the contribution from $q\bar{q}q\bar{q}$ final states for energies between M_Z and 1000 GeV.

4.6 Comparison to related work

In Ref. [60], another calculation of electroweak corrections to three-jet observables was performed, which differs in two important aspects from the work presented here. First, the NLO electroweak corrections to the hadronic cross section were not taken into account, such that only unnormalised distributions were considered. Second, only the corrections to $q\bar{q}g$ final states were considered, while $q\bar{q}\gamma$ final states at LO and NLO were not taken into account. To remove singularities associated with infrared gluons in $q\bar{q}\gamma g$ final states, event-shape observables were calculated from the reconstructed jet momenta and not from the parton momenta, as used in experiment and in our work. Additionally, a lower cut on the energy of each jet has been imposed which leads to a distortion of the shape of the distributions near the two-jet region. From Ref. [60] it is not clear how exactly the event selection is performed in the calculation of the NLO corrections. Therefore a direct comparison with the results of Ref. [60] is at present not possible.

Taking care of the different renormalisation of α, we do observe, however, in the distributions normalised to σ_0, Figs. 4.5 and 4.6, that the relative size of the $\mathcal{O}(\alpha)$ weak and exact corrections, and of the LL-improved corrections to the thrust distribution agree at the per-cent level with the results of Ref. [60], except in the region $(1-T) < 0.05$, where $q\bar{q}\gamma$ final states contribute and the lower cut on the jet momenta is in effect.

Chapter 5

Conclusions

We have presented results for the NLO electroweak corrections to three- and four-jet production and related event-shape observables. In experimental analyses, these distributions are normalised to the total hadronic cross section σ_{had}. To consistently treat the normalisation in perturbation theory, we have calculated the NLO electroweak corrections to σ_{had} as well.

In particular, we have included the NLO electroweak corrections to the process $\mathrm{e^+e^-} \to q\bar{q}\mathrm{g}$. Since photons and hadrons are clustered democratically, we have also incorporated the NLO QCD corrections to the process $\mathrm{e^+e^-} \to q\bar{q}\gamma$. Both contributions are of the order $\alpha_{\mathrm{s}}\alpha^3$ and share the same Bremsstrahlung process $\mathrm{e^+e^-} \to q\bar{q}\mathrm{g}\gamma$. This allows us to treat all observables near the two-jet limit and only leaves a singularity in the endpoint. We have avoided this singularity by imposing a lower cut-off which does not influence the shape of the distribution but only enters in one, typically the first, bin of the respective distribution. For the normalisation, we have calculated the NLO electroweak corrections to the process $\mathrm{e^+e^-} \to q\bar{q}$. The NLO electroweak corrections have been complemented by higher-order initial-state-radiation effects in a leading-logarithmic structure-function approach.

Furthermore, the experimental event-selection procedure has been modelled as closely as possible. Specifically, we have implemented a cut on the photonic energy in a jet, which formally leads to the breakdown of infrared-safety. To restore infrared-safety we have used the photon fragmentation function together with the non-collinear-safe subtraction and phase-space-slicing methods. In this context we have shown analytic results for the required integrations over the fraction of photonic energy in a jet in the presence of a cut-off. The photon fragmentation function has been translated from dimensional regularisation to mass-regularisation which has been used throughout this thesis.

In addition, we have presented the analytical results for the tree-level and Bremsstrahlungs matrix elements. Together with the standard matrix elements of the virtual corrections, they have been evaluated using the Weyl-van der Waerden formalism.

The ingredients described above have been implemented in a Monte Carlo program based on the package POLE. The program is flexible such that the user can provide various event-selection cuts and investigate different observables. It has been extensively tested for internal consistency and comparisons with independent programs have been successfully carried out.

A numerical study revealed the following results: For energies between 1 GeV and 1 TeV, the NLO electroweak corrections to σ_{had} range between -10% and -30% and are dominated by electromagnetic initial-state-radiation effects. The virtual one-loop weak corrections only range between -5% and $+5\%$. For $\sqrt{s} = M_{\mathrm{Z}}$, higher-order leading-logarithmic corrections are of the order of a few per-cent, whereas below and above M_{Z} they are at the per-mille level.

For $\sqrt{s} = M_{\mathrm{Z}}$, we have shown the results for the NLO electroweak corrections to event-shape distributions and jet-rates, without taking the normalisation to σ_{had} into account. Away from the two-jet region they are usually flat and range between -25% and -32%. Near the two-jet region, $q\bar{q}\gamma$ final states contribute and lead to a distortion of the shape. Higher-order leading-logarithmic effects and the virtual one-loop weak corrections are at the per-cent level. Taking the normalisation to σ_{had} into account, the large initial-state-radiation corrections cancel between the event-shape distributions and the normalisation to the hadronic cross section, resulting in electroweak corrections between -4% and $+4\%$ for $\sqrt{s} = M_{\mathrm{Z}}$ and between -10% and $+10\%$ for $\sqrt{s} > M_{\mathrm{Z}}$. Moreover, effects from higher-order leading-logarithmic resummation are largely reduced as well such that the fixed-order corrections coincide with the corrections also including higher-order leading-logarithmic effects. The virtual one-loop weak corrections are typically at the per-mille level and slightly increase for higher energies.

We have shown that the shape of the corrections strongly depends on the values of the parameters used in the event selection. In particular, we see remnants of the radiative-return phenomenon that was believed to be excluded due to the specific choice of the event-selection parameters. We have estimated where this phenomenon appears, using the thrust distribution as an example, and have shown how it depends on the event-selection parameters.

Data on event-shape distributions and jet cross sections have been corrected for photonic radiation effects modelled by standard leading-logarithmic parton-shower Monte Carlo programs. They can thus not be compared directly with the NLO electroweak corrections computed here. Incorporation of these corrections requires a more profound reanalysis of LEP data, in order to quantify the impact of the NLO electroweak corrections on precision QCD studies, such as the precise extraction of the strong coupling constant.

For future experiments, it is mandatory to define an infrared-safe event selection, such that higher-order perturbative theoretical predictions can be used in the analysis of experimental data.

Appendix A

Evaluation of Matrix Elements and Analytical Results

In order to calculate the SMEs introduced in Chapter 2 as well as to compute the real corrections to the process at hand in an efficient manner, we employ the Weyl–van der Waerden (WvdW) formalism as presented in Ref. [86].

A.1 Weyl–van der Waerden formalism

In the WvdW formalism one reduces all mathematical objects belonging to higher-dimensional representations of the Lorentz group to the two-dimensional irreducible representations $D\left(\frac{1}{2},0\right)$ and $D\left(0,\frac{1}{2}\right)$. We define the two-dimensional covariant spinor ψ_A and contravariant spinor $\psi^{\dot{A}}$ which transform according to the above mentioned representations. Using complex conjugation and a similarity transformation mediated by the 2×2 antisymmetric matrix ϵ

$$\epsilon^{AB} = \epsilon^{\dot{A}\dot{B}} = \epsilon_{AB} = \epsilon_{\dot{A}\dot{B}} = \begin{pmatrix} 0 & +1 \\ -1 & 0 \end{pmatrix}, \tag{A.1}$$

we can relate the spinors belonging to the two representations by

$$\psi_{\dot{A}} = (\psi_A)^*, \quad \psi^A = \left(\psi^{\dot{A}}\right)^*, \tag{A.2}$$

and

$$\psi^A = \epsilon^{AB}\psi_B, \quad \psi^{\dot{A}} = \epsilon^{\dot{A}\dot{B}}\psi_{\dot{B}}, \quad \psi_A = \psi^B\epsilon_{BA}, \quad \psi_{\dot{A}} = \psi^{\dot{B}}\epsilon_{\dot{B}\dot{A}}. \tag{A.3}$$

The matrix ϵ also induces a *spinor metric*, which can be employed to define a Lorentz-invariant antisymmetric spinor product through

$$\langle\phi\psi\rangle = \phi_A\psi^A = \phi_1\psi_2 - \phi_2\psi_1, \quad \langle\phi\psi\rangle^* = \phi_{\dot{A}}\psi^{\dot{A}} = (\phi_1\psi_2 - \phi_2\psi_1)^*, \tag{A.4}$$

$$\langle\phi\psi\rangle = -\langle\psi\phi\rangle, \quad \langle\phi\phi\rangle = 0. \tag{A.5}$$

In analogy to the Schouten identity Eq. (2.16) in four dimensions, there cannot exist a two-dimensional antisymmetric tensor with rank higher than two in spinor space, which leads to the equation

$$\epsilon^{AB}\epsilon^{CD} + \epsilon^{AC}\epsilon^{DB} + \epsilon^{AD}\epsilon^{BC} = 0, \tag{A.6}$$

resulting in the identity for spinors

$$\langle\phi\psi\rangle\langle\xi\eta\rangle + \langle\phi\xi\rangle\langle\eta\psi\rangle + \langle\phi\eta\rangle\langle\psi\xi\rangle = 0. \tag{A.7}$$

Throughout our calculation we need four-vectors, Dirac spinors, and polarisation vectors of massless particles. In the following we describe how one can express the above objects in terms of WvdW spinors.

Let us start with a usual four-vector $k^\mu = (k^0, \mathbf{k})$, which belongs to the $D\left(\frac{1}{2}, \frac{1}{2}\right)$ representation of the Lorentz group. Using the matrices

$$\sigma^{\mu,\dot{A}B} = \left(\sigma^0, \sigma\right), \quad \sigma^\mu_{A\dot{B}} = \left(\sigma^0, -\sigma\right), \tag{A.8}$$

where σ^0 is the 2×2 unit matrix and σ^a the Pauli matrices, we can relate k^μ to the 2×2 matrix

$$K_{\dot{A}B} = k^\mu \sigma_{\mu,\dot{A}B} = \begin{pmatrix} k^0 + k^3 & k^1 + \mathrm{i}k^2 \\ k^1 - \mathrm{i}k^2 & k^0 - k^3 \end{pmatrix}. \tag{A.9}$$

The identities Eq. (A.3) also hold for $K_{\dot{A}B}$. If the components of k^μ are real, $K_{\dot{A}B}$ is Hermitian. In this case we can find its eigenvalues λ_i and write

$$K_{\dot{A}B} = \sum_{i=1,2} k_{i,\dot{A}} k_{i,B}, \tag{A.10}$$

with

$$k_{1,A} = \sqrt{\lambda_1} \begin{pmatrix} e^{-\mathrm{i}\phi}\cos\frac{\theta}{2} \\ \sin\frac{\theta}{2} \end{pmatrix}, \quad k_{2,A} = \sqrt{\lambda_2} \begin{pmatrix} \sin\frac{\theta}{2} \\ -e^{+\mathrm{i}\phi}\cos\frac{\theta}{2} \end{pmatrix}, \tag{A.11}$$

where θ and ϕ denote the polar and azimuthal angles of the euclidean vector $\mathbf{k}$. For a light-like vector k^μ with $k^2 = 0$, one of the eigenvectors vanishes and there remains just one momentum spinor k_1.

We now turn to fermionic wave functions, which transform according to the representation $D\left(\frac{1}{2}, 0\right) \oplus D\left(0, \frac{1}{2}\right)$ of the Lorentz group and can thus be written as

$$\Psi = \begin{pmatrix} \phi_A \\ \psi^{\dot{A}} \end{pmatrix}. \tag{A.12}$$

The behaviour of fermionic spinors is governed by the Dirac equation

$$(\mathrm{i}\partial\!\!\!/ - m)\,\Psi = 0, \tag{A.13}$$

where m denotes the mass of the fermion under consideration and the Dirac matrices γ^μ in the chiral representation are given by

$$\gamma^\mu = \begin{pmatrix} 0 & \sigma^\mu_{A\dot{B}} \\ \sigma^{\mu,\dot{A}B} & 0 \end{pmatrix}, \qquad \gamma^5 = \mathrm{i}\gamma^1\gamma^1\gamma^2\gamma^3 = \begin{pmatrix} \sigma^0 & 0 \\ 0 & -\sigma^0 \end{pmatrix}. \tag{A.14}$$

The plane-wave solutions of this equation are of the form

$$\Psi^\pm = e^{\mp \mathrm{i}kx}\Psi^\pm_k, \qquad k^2 = m^2. \tag{A.15}$$

The components $\Psi^\pm_k$ are solutions of the Weyl equations, a system of coupled differential equations, and read

$$\Psi^\pm_{k,1} = \begin{pmatrix} k_{1,A} \\ \mp k_2^{\dot{A}} \end{pmatrix}, \qquad \Psi^\pm_{k,2} = \begin{pmatrix} \pm k_{2,A} \\ k_1^{\dot{A}} \end{pmatrix}, \tag{A.16}$$

whereas the adjoint spinors $\overline{\Psi} = \Psi^\dagger\gamma_0$ are given by

$$\overline{\Psi}^\pm_{k,1} = \left(\mp k_2^A, k_{1,\dot{A}}\right), \qquad \overline{\Psi}^\pm_{k,2} = \left(k_1^A, \pm k_{2,\dot{A}}\right). \tag{A.17}$$

In the special case of massless spinors, Eqs. (A.16) and (A.17) simplify to

$$\begin{aligned} \Psi^\pm_{k,1} &= \begin{pmatrix} k_A \\ 0 \end{pmatrix}, & \Psi^\pm_{k,2} &= \begin{pmatrix} 0 \\ k^{\dot{A}} \end{pmatrix}, \\ \overline{\Psi}^\pm_{k,1} &= (0, k_{\dot{A}}), & \overline{\Psi}^\pm_{k,2} &= \left(k^A, 0\right). \end{aligned} \tag{A.18}$$

The last objects we need in our calculation are polarisation vectors. In contrast to an ordinary four-vector, polarisation vectors need not have real components and are therefore not Hermitian. Thus, we cannot treat them according to Eqs. (A.10) and (A.11).

The procedure to derive the form of the polarisation vectors of spin-1 particles in the WvdW formalism is similar to the case of Dirac fermions, using instead of the Dirac equation the Proca equation. We therefore display only the results for massless spin-1 particles, which we encounter in our calculation. The polarisation vectors $\epsilon^\mu_\pm$ read

$$\begin{aligned} \epsilon_{+,\dot{A}B}(k) &= \frac{\sqrt{2}g_{+,\dot{A}}k_B}{\langle g_+ k\rangle^*}, & \epsilon_{-,\dot{A}B}(k) &= \frac{\sqrt{2}k_{\dot{A}}g_{-,B}}{\langle g_- k\rangle}, \\ \epsilon^*_{+,\dot{A}B}(k) &= \frac{\sqrt{2}k_{\dot{A}}g_{+,B}}{\langle g_+ k\rangle}, & \epsilon^*_{-,\dot{A}B}(k) &= \frac{\sqrt{2}g_{-,\dot{A}}k_B}{\langle g_- k\rangle^*}, \end{aligned} \tag{A.19}$$

where $g_{\pm,A}$ denotes arbitrary gauge spinors, which reflect the freedom to choose a gauge for the polarisation vector. Physical observables do not depend on the gauge spinor, therefore their variation can be used to check the gauge independence of the amplitude.

A.2 Analytical results for the tree-level amplitude

In this section we give the analytical results for the amplitudes contributing to the Born processes using the techniques described in Section A.1. Fermion masses are set to zero everywhere.

The corresponding Feynman diagrams are shown in Figs. 2.1–2.3. We use the generic couplings of the Z boson and the photon to the fermions given by

$$g^{\pm}_{\gamma f} = -Q_f, \quad g^{+}_{Zf} = -\frac{s_\mathrm{w}}{c_\mathrm{w}} Q_f, \quad g^{-}_{Zf} = -\frac{s_\mathrm{w}}{c_\mathrm{w}} Q_f + \frac{I_{\mathrm{w},f}}{c_\mathrm{w} s_\mathrm{w}}, \tag{A.20}$$

where c_w and s_w are the sine and cosine of the weak mixing angle respectively, Q_f is the relative electromagnetic charge of the fermion f, and $I_{\mathrm{w},f} = \pm\frac{1}{2}$ is the weak isospin of the left-handed part of the fermion field f. The electroweak Standard Model does not conserve parity, but we can find a relation which connects amplitudes with opposite helicity configurations and additionally involves the interchange of the chiral couplings:

$$\mathcal{M}\left(-\sigma, -\sigma', -\lambda\right) = \mathcal{M}\left(\sigma, \sigma', \lambda\right)^* \big|_{\substack{(g^{\pm})^* \leftrightarrow g^{\mp} \\ M_V \to M_V^*}}. \tag{A.21}$$

We decompose the matrix elements $\mathcal{M}$ according to the boson in the s channel,

$$\mathcal{M}\left(\sigma, \sigma', \lambda\right) = 2\sqrt{2}\, e^2 g_\mathrm{s} \sum_{V=\gamma,Z} A^{(V)}_{\lambda}\left(\sigma, \sigma'\right), \tag{A.22}$$

where g_s is the strong coupling constant and the function $A^{(V)}_{\lambda}$ is a generic function for the exchange of a vector boson V.

For the process in Eq. (2.2) we find

$$\begin{aligned} \mathcal{M}\left(\sigma, \sigma'\right) \;=\; & \frac{2\, e^2}{\left[(k_1+k_2)^2 - M_V^2\right]} \Big\{ g^{+}_{Ve} g^{+}_{Vq} \langle k_1 k_4\rangle \langle k_2 k_3\rangle^* + g^{+}_{Ve} g^{-}_{Vq} \langle k_1 k_3\rangle \langle k_2 k_4\rangle^* \\ & + g^{-}_{Ve} g^{+}_{Vq} \langle k_2 k_4\rangle \langle k_1 k_3\rangle^* + g^{-}_{Ve} g^{-}_{Vq} \langle k_2 k_3\rangle \langle k_1 k_4\rangle^* \Big\}. \end{aligned} \tag{A.23}$$

Since there is no photon in the final state, there is also no dependence on the helicity λ in Eq. (A.22).

The amplitude for the process in Eq. (2.3) is given by

$$\begin{aligned} A^{(V)}_{+} \;=\; & \frac{1}{\left[(k_1+k_2)^2 - M_V^2\right] \langle k_3 k_5\rangle \langle k_4 k_5\rangle} \Big\{ \\ & - g^{+}_{Ve} g^{+}_{Vq} \left[\langle k_1 k_4\rangle^2 \langle k_1 k_2\rangle^*\right] + g^{+}_{Ve} g^{-}_{Vq} \left[\langle k_1 k_3\rangle^2 \langle k_1 k_2\rangle^*\right] \\ & + g^{-}_{Ve} g^{+}_{Vq} \left[\langle k_2 k_4\rangle^2 \langle k_1 k_2\rangle^*\right] - g^{-}_{Ve} g^{-}_{Vq} \left[\langle k_2 k_3\rangle^2 \langle k_1 k_2\rangle^*\right] \Big\}. \end{aligned} \tag{A.24}$$

The amplitude for $\lambda = -1$ can be obtained using Eq. (A.21).

Finally for the third process in Eq. (2.4) we find

$$\begin{aligned}
A_{+}^{(V)} = & \frac{Q_q}{\left[(k_1+k_2)^2 - M_V^2\right]\langle k_3 k_5\rangle\langle k_4 k_5\rangle}\Big\{ \\
& - g_{Ve}^{+} g_{Vq}^{+}\left[\langle k_1 k_4\rangle^2 \langle k_1 k_2\rangle^*\right] + g_{Ve}^{+} g_{Vq}^{-}\left[\langle k_1 k_3\rangle^2 \langle k_1 k_2\rangle^*\right] \\
& + g_{Ve}^{-} g_{Vq}^{+}\left[\langle k_2 k_4\rangle^2 \langle k_1 k_2\rangle^*\right] - g_{Ve}^{-} g_{Vq}^{-}\left[\langle k_2 k_3\rangle^2 \langle k_1 k_2\rangle^*\right] \Big\} \\
& + \frac{1}{\left[(k_1+k_2-k_5)^2 - M_V^2\right]\langle k_1 k_5\rangle\langle k_3 k_5\rangle}\Big\{ \\
& \quad g_{Ve}^{+} g_{Vq}^{+}\langle k_1 k_4\rangle^2 \langle k_3 k_4\rangle^* - g_{Ve}^{+} g_{Vq}^{-}\langle k_1 k_3\rangle^2 \langle k_3 k_4\rangle^* \\
& \quad - g_{Ve}^{-} g_{Vq}^{+}\langle k_2 k_4\rangle^2 \langle k_3 k_4\rangle^* + g_{Ve}^{-} g_{Vq}^{-}\langle k_2 k_3\rangle^2 \langle k_3 k_4\rangle^* \Big\}.
\end{aligned} \tag{A.25}$$

The amplitude for $\lambda = -1$ can be obtained using Eq. (A.21).

A.3 Analytical results for the real-radiation amplitudes

We now turn to the real-radiation amplitude induced by the radiation of a real photon, which is given by the process in Eq. (2.34). The contributing Feynman diagrams are shown in Fig. A.1. We again decompose the matrix elements $\mathcal{M}$ according to the boson in the s channel,

$$\mathcal{M}(\sigma, \sigma', \lambda_1, \lambda_2) = \frac{1}{4} e^3 g_s \sum_{V=\gamma,Z} A_{\lambda_1\lambda_2}^{(V)}(\sigma, \sigma'), \tag{A.26}$$

with

$$\begin{aligned}
A_{++}^{(V)} = & \frac{\langle k_3 k_4\rangle Q_q}{\left[(k_1+k_2)^2 - M_V^2\right]\langle k_3 k_5\rangle\langle k_3 k_6\rangle\langle k_4 k_5\rangle\langle k_4 k_6\rangle}\Big\{ \\
& - g_{Ve}^{+} g_{Vq}^{+}\langle k_1 k_4\rangle^2 \langle k_3 k_4\rangle\langle k_1 k_2\rangle^* + g_{Ve}^{+} g_{Vq}^{-}\langle k_1 k_3\rangle^2 \langle k_3 k_4\rangle\langle k_1 k_2\rangle^* \\
& + g_{Ve}^{-} g_{Vq}^{+}\langle k_2 k_4\rangle^2 \langle k_3 k_4\rangle\langle k_1 k_2\rangle^* - g_{Ve}^{-} g_{Vq}^{-}\langle k_2 k_3\rangle^2 \langle k_3 k_4\rangle\langle k_1 k_2\rangle^* \Big\} \\
& + \frac{\langle k_3 k_4\rangle}{\left[(k_1+k_2-k_6)^2 - M_V^2\right]\langle k_1 k_6\rangle\langle k_2 k_6\rangle\langle k_3 k_5\rangle\langle k_4 k_5\rangle}\Big\{ \\
& g_{Ve}^{+} g_{Vq}^{+}\Big[\langle k_1 k_4\rangle\left(\langle k_1 k_2\rangle\left(\langle k_4 k_5\rangle\langle k_2 k_5\rangle^* - \langle k_3 k_4\rangle\langle k_2 k_3\rangle^*\right)\right. \\
& \qquad \left. + \langle k_1 k_6\rangle\left(\langle k_4 k_5\rangle\langle k_5 k_6\rangle^* - \langle k_3 k_4\rangle\langle k_3 k_6\rangle^*\right)\right)\Big] \\
& - g_{Ve}^{+} g_{Vq}^{-}\Big[\langle k_1 k_3\rangle\left(\langle k_1 k_2\rangle\left(\langle k_3 k_4\rangle\langle k_2 k_4\rangle^* + \langle k_3 k_5\rangle\langle k_2 k_5\rangle^*\right)\right.
\end{aligned}$$

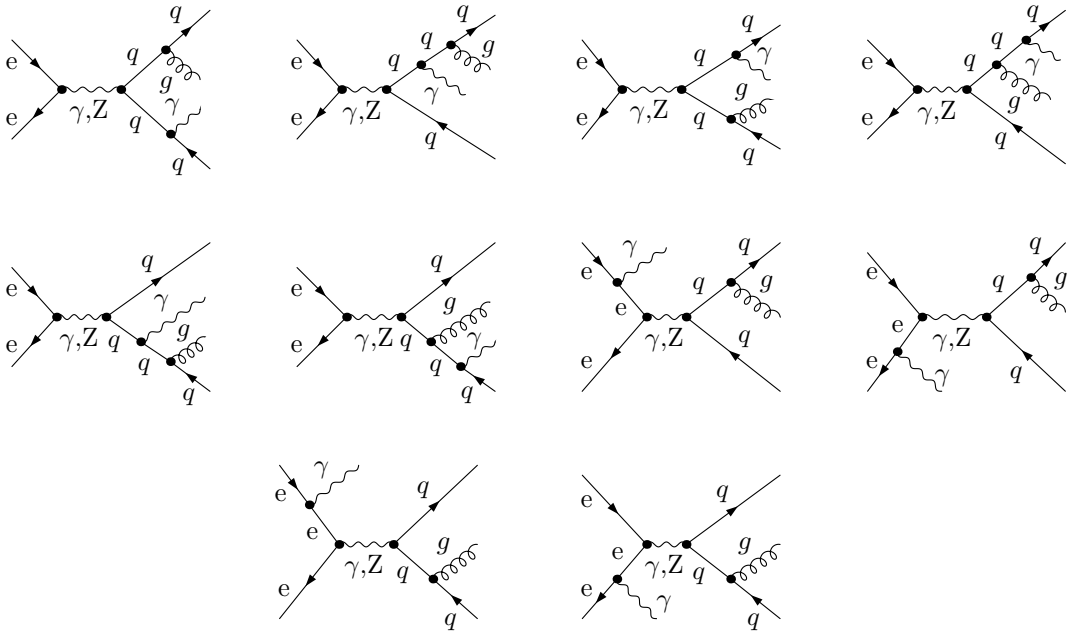

Figure A.1: Feynman diagrams for $e^+e^- \to q\bar{q}g\gamma$.

$$
\begin{aligned}
&\quad + \langle k_1 k_6\rangle \left(\langle k_3 k_4\rangle \langle k_4 k_6\rangle^* + \langle k_3 k_5\rangle \langle k_5 k_6\rangle^*\right)\Big] \\
&+ g_{Ve}^- g_{Vq}^+ \Big[\langle k_2 k_4\rangle \left(\langle k_1 k_2\rangle \left(\langle k_4 k_5\rangle \langle k_1 k_5\rangle^* - \langle k_3 k_4\rangle \langle k_1 k_3\rangle^*\right)\right. \\
&\quad \left. + \langle k_2 k_6\rangle \left(\langle k_3 k_4\rangle \langle k_3 k_6\rangle^* - \langle k_4 k_5\rangle \langle k_5 k_6\rangle^*\right)\right)\Big] \\
&+ g_{Ve}^- g_{Vq}^- \Big[\langle k_2 k_6\rangle \left(\langle k_3 k_4\rangle \langle k_4 k_6\rangle^* + \langle k_3 k_5\rangle \langle k_5 k_6\rangle^*\right)\Big) \\
&\quad - \langle k_2 k_3\rangle \left(\langle k_1 k_2\rangle \left(\langle k_3 k_4\rangle \langle k_1 k_4\rangle^* + \langle k_3 k_5\rangle \langle k_1 k_5\rangle^*\right)\right)\Big]\Big\} \qquad \text{(A.27)}
\end{aligned}
$$

and

$$
\begin{aligned}
A_{+-}^{(V)} = \frac{Q_q}{\left[(k_1+k_2)^2 - M_V^2\right]}\Bigg\{ & \\
g_{Ve}^+ g_{Vq}^+ \Bigg[& \frac{\langle k_1 k_4\rangle \langle k_3 k_4\rangle \langle k_2 k_3\rangle^* \langle k_3 k_4\rangle^* - \langle k_1 k_6\rangle \langle k_4 k_5\rangle \langle k_2 k_5\rangle^* \langle k_3 k_6\rangle^*}{\langle k_3 k_5\rangle \langle k_4 k_5\rangle \langle k_3 k_6\rangle^* \langle k_4 k_6\rangle^*} \\
& + \frac{\langle k_1 k_4\rangle \langle k_3 k_6\rangle \langle k_2 k_3\rangle^* \langle k_4 k_5\rangle^*}{s_{356} \langle k_3 k_5\rangle \langle k_4 k_6\rangle^*} - \frac{\langle k_1 k_4\rangle \langle k_2 k_5\rangle^* \langle k_3 k_4\rangle^* \langle k_3 k_5\rangle^*}{s_{356} \langle k_3 k_6\rangle^* \langle k_4 k_6\rangle^*} \\
& + \frac{\langle k_1 k_4\rangle \langle k_5 k_6\rangle \langle k_2 k_5\rangle^* \langle k_4 k_5\rangle^*}{s_{356} \langle k_3 k_5\rangle \langle k_4 k_6\rangle^*} - \frac{\langle k_1 k_4\rangle \langle k_3 k_6\rangle \langle k_2 k_6\rangle^* \langle k_3 k_4\rangle^* \langle k_3 k_5\rangle^*}{s_{356} \langle k_3 k_5\rangle \langle k_3 k_6\rangle^* \langle k_4 k_6\rangle^*}
\end{aligned}
$$

$$
\begin{aligned}
&+\frac{\langle k_1k_6\rangle\langle k_3k_4\rangle\langle k_4k_6\rangle\langle k_2k_3\rangle^*}{s_{456}\langle k_3k_5\rangle\langle k_4k_5\rangle}+\frac{\langle k_1k_4\rangle\langle k_3k_6\rangle\langle k_2k_3\rangle^*\langle k_4k_5\rangle^*}{s_{456}\langle k_3k_5\rangle\langle k_4k_6\rangle^*}\\
&+\frac{\langle k_1k_5\rangle\langle k_3k_4\rangle\langle k_4k_6\rangle\langle k_2k_3\rangle^*\langle k_4k_5\rangle^*}{s_{456}\langle k_3k_5\rangle\langle k_4k_5\rangle\langle k_4k_6\rangle^*}-\frac{\langle k_1k_6\rangle\langle k_3k_6\rangle\langle k_2k_3\rangle^*\langle k_5k_6\rangle^*}{s_{456}\langle k_3k_5\rangle\langle k_4k_6\rangle^*}\Bigg]\\
&+g_{Ve}^+g_{Vq}^-\Bigg[\frac{\langle k_1k_3\rangle(\langle k_4k_6\rangle\langle k_2k_4\rangle^*+\langle k_5k_6\rangle\langle k_2k_5\rangle^*)\langle k_4k_5\rangle^*}{s_{456}\langle k_4k_5\rangle\langle k_4k_6\rangle^*}\\
&+\frac{\langle k_3k_6\rangle\langle k_2k_4\rangle^*(\langle k_1k_3\rangle\langle k_3k_5\rangle^*-\langle k_1k_6\rangle\langle k_5k_6\rangle^*)}{s_{356}\langle k_3k_5\rangle\langle k_3k_6\rangle^*}\\
&+\frac{(\langle k_3k_4\rangle\langle k_2k_4\rangle^*+\langle k_3k_5\rangle\langle k_2k_5\rangle^*)(\langle k_1k_3\rangle\langle k_3k_4\rangle^*-\langle k_1k_6\rangle\langle k_4k_6\rangle^*)}{\langle k_3k_5\rangle\langle k_4k_5\rangle\langle k_3k_6\rangle^*\langle k_4k_6\rangle^*}\Bigg]\\
&+g_{Ve}^-g_{Vq}^+\Bigg[\frac{\langle k_2k_4\rangle\langle k_3k_4\rangle\langle k_1k_3\rangle^*\langle k_3k_4\rangle^*-\langle k_2k_6\rangle\langle k_1k_5\rangle^*\langle k_4k_5\rangle\langle k_3k_6\rangle^*}{\langle k_3k_5\rangle\langle k_4k_5\rangle\langle k_3k_6\rangle^*\langle k_4k_6\rangle^*}\\
&+\frac{\langle k_2k_4\rangle\langle k_1k_5\rangle^*\langle k_3k_4\rangle^*\langle k_3k_5\rangle^*}{s_{356}\langle k_3k_6\rangle^*\langle k_4k_6\rangle^*}-\frac{\langle k_2k_4\rangle\langle k_3k_6\rangle\langle k_1k_6\rangle^*\langle k_3k_4\rangle^*\langle k_3k_5\rangle^*}{s_{356}\langle k_3k_5\rangle\langle k_3k_6\rangle^*\langle k_4k_6\rangle^*}\\
&+\frac{\langle k_2k_4\rangle\langle k_3k_6\rangle\langle k_1k_3\rangle^*\langle k_4k_5\rangle^*}{s_{356}\langle k_3k_5\rangle\langle k_4k_6\rangle^*}+\frac{\langle k_2k_4\rangle\langle k_5k_6\rangle\langle k_1k_5\rangle^*\langle k_4k_5\rangle^*}{s_{356}\langle k_3k_5\rangle\langle k_4k_6\rangle^*}\\
&+\frac{\langle k_2k_6\rangle\langle k_3k_4\rangle\langle k_4k_6\rangle\langle k_1k_3\rangle^*}{s_{456}\langle k_3k_5\rangle\langle k_4k_5\rangle}+\frac{\langle k_2k_4\rangle\langle k_3k_6\rangle\langle k_1k_3\rangle^*\langle k_4k_5\rangle^*}{s_{456}\langle k_3k_5\rangle\langle k_4k_6\rangle^*}\\
&+\frac{\langle k_2k_5\rangle\langle k_3k_4\rangle\langle k_4k_6\rangle\langle k_1k_3\rangle^*\langle k_4k_5\rangle^*}{s_{456}\langle k_3k_5\rangle\langle k_4k_5\rangle\langle k_4k_6\rangle^*}-\frac{\langle k_2k_6\rangle\langle k_3k_6\rangle\langle k_1k_3\rangle^*\langle k_5k_6\rangle^*}{s_{456}\langle k_3k_5\rangle\langle k_4k_6\rangle^*}\Bigg]\\
&+g_{Ve}^-g_{Vq}^-\Bigg[\frac{\langle k_2k_3\rangle(\langle k_4k_6\rangle\langle k_1k_4\rangle^*+\langle k_5k_6\rangle\langle k_1k_5\rangle^*)\langle k_4k_5\rangle^*}{s_{456}\langle k_4k_5\rangle\langle k_4k_6\rangle^*}\\
&+\frac{\langle k_3k_6\rangle\langle k_1k_4\rangle^*(\langle k_2k_3\rangle\langle k_3k_5\rangle^*-\langle k_2k_6\rangle\langle k_5k_6\rangle^*)}{s_{356}\langle k_3k_5\rangle\langle k_3k_6\rangle^*}\\
&+\frac{(\langle k_3k_4\rangle\langle k_1k_4\rangle^*+\langle k_3k_5\rangle\langle k_1k_5\rangle^*)(\langle k_2k_3\rangle\langle k_3k_4\rangle^*-\langle k_2k_6\rangle\langle k_4k_6\rangle^*)}{\langle k_3k_5\rangle\langle k_4k_5\rangle\langle k_3k_6\rangle^*\langle k_4k_6\rangle^*}\Bigg]\Bigg\}\\
&+\frac{\langle k_3k_4\rangle}{\left[(k_1+k_2-k_6)^2-M_V^2\right]\langle k_3k_5\rangle\langle k_4k_5\rangle\langle k_1k_6\rangle^*\langle k_2k_6\rangle^*}\Big\{\\
&g_{Ve}^+g_{Vq}^+\Big[(\langle k_4k_5\rangle\langle k_2k_5\rangle^*-\langle k_3k_4\rangle\langle k_2k_3\rangle^*)(\langle k_4k_6\rangle\langle k_2k_6\rangle^*-\langle k_1k_4\rangle\langle k_1k_2\rangle^*)\Big]\\
&+g_{Ve}^+g_{Vq}^-\Big[(\langle k_3k_4\rangle\langle k_2k_4\rangle^*+\langle k_3k_5\rangle\langle k_2k_5\rangle^*)(\langle k_3k_6\rangle\langle k_2k_6\rangle^*-\langle k_1k_3\rangle\langle k_1k_2\rangle^*)\Big]\\
&+g_{Ve}^-g_{Vq}^+\Big[(-\langle k_3k_4\rangle\langle k_1k_3\rangle^*+\langle k_4k_5\rangle\langle k_1k_5\rangle^*)(\langle k_2k_4\rangle\langle k_1k_2\rangle^*+\langle k_4k_6\rangle\langle k_1k_6\rangle^*)\Big]\\
&-g_{Ve}^-g_{Vq}^-\Big[(\langle k_3k_4\rangle\langle k_1k_4\rangle^*+\langle k_3k_5\rangle\langle k_1k_5\rangle^*)(\langle k_2k_3\rangle\langle k_1k_2\rangle^*+\langle k_3k_6\rangle\langle k_1k_6\rangle^*)\Big]\Big\},
\end{aligned}
\tag{A.28}
$$

where $s_{ijk} = \langle k_i k_j\rangle\langle k_i k_j\rangle^* + \langle k_i k_k\rangle\langle k_i k_k\rangle^* + \langle k_j k_k\rangle\langle k_j k_k\rangle^*$.

The amplitudes $A^{(V)}_{--}$ and $A^{(V)}_{-+}$ can be obtained from

$$\mathcal{M}\left(-\sigma,-\sigma',-\lambda_1,-\lambda_2\right) = \mathcal{M}\left(\sigma,\sigma',\lambda_1,\lambda_2\right)^* |_{\substack{(g^\pm_{\dots})^*\leftrightarrow g^\mp_{\dots} \\ M_V\to M_V^*}}. \tag{A.29}$$

Again, in this section we set all masses of the external fermions to zero, and finite-mass effects are treated in Section 2.3.

A.4 The standard structures of the one-loop amplitude in the WvdW formalism

We now want to give the expressions Eq. (2.30) and Eq. (2.23) in the WvdW formalism. The ϵ-Tensor in the spinor calculus reads

$$\epsilon^{\mu\nu\rho\kappa} = \frac{\mathrm{i}}{4}\left(\sigma^\mu_{\dot A B}\sigma^{\nu,B\dot C}\sigma^\kappa_{\dot C D}\sigma^{\rho,D\dot A} - \sigma^\mu_{\dot A B}\sigma^{\rho,B\dot C}\sigma^\kappa_{\dot C D}\sigma^{\nu,D\dot A}\right), \tag{A.30}$$

and we can therefore write

$$\begin{aligned}
A^{++-+}_{ijkl} &= \frac{1}{2}\langle k_i k_j\rangle\langle k_k k_l\rangle\langle k_i k_k\rangle^*\langle k_j k_l\rangle^*,\\
A^{+-++}_{ijkl} &= \frac{1}{2}\langle k_i k_l\rangle\langle k_k k_j\rangle\langle k_i k_j\rangle^*\langle k_k k_l\rangle^*,\\
A^{-+++}_{ijkl} &= \frac{1}{2}\langle k_i k_k\rangle\langle k_j k_l\rangle\langle k_i k_l\rangle^*\langle k_j k_k\rangle^*,\\
A^{abc-}_{ijkl} &= (A^{abc+}_{ijkl})^*.
\end{aligned} \tag{A.31}$$

The standard structures read

$$\begin{aligned}
(k_i k_j) &= \frac{1}{2}\langle k_i k_j\rangle\langle k_i k_j\rangle^*,\\
\left((\epsilon^*)^+ k_i\right) = \frac{\langle k_i k_2\rangle\langle k_i k_5\rangle^*}{\sqrt{2}\langle k_2 k_5\rangle} &\quad , \quad \left((\epsilon^*)^- k_i\right) = \frac{\langle k_i k_5\rangle\langle k_i k_2\rangle^*}{\sqrt{2}\langle k_2 k_5\rangle^*},\\
\left[\not{k}_l\right]^-_{ij} = \langle k_l k_i\rangle\langle k_l k_j\rangle^* &\quad , \quad \left[\not{k}_l\right]^+_{ij} = \langle k_l k_i\rangle^*\langle k_l k_j\rangle,\\
\left[(\not{\epsilon}^*)^+\right]^+_{ij} = \frac{\sqrt{2}\langle k_i k_2\rangle\langle k_j k_5\rangle^*}{\langle k_2 k_5\rangle} &\quad , \quad \left[(\not{\epsilon}^*)^+\right]^-_{ij} = \frac{\sqrt{2}\langle k_j k_2\rangle\langle k_i k_5\rangle^*}{\langle k_2 k_5\rangle},\\
\left[(\not{\epsilon}^*)^-\right]^+_{ij} = \frac{\sqrt{2}\langle k_i k_5\rangle\langle k_j k_2\rangle^*}{\langle k_2 k_5\rangle^*} &\quad , \quad \left[(\not{\epsilon}^*)^-\right]^-_{ij} = \frac{\sqrt{2}\langle k_j k_5\rangle\langle k_i k_2\rangle^*}{\langle k_2 k_5\rangle^*},
\end{aligned} \tag{A.32}$$

where we chose the gauge spinor parallel to k_2.

Bibliography

[1] H. Fritzsch, M. Gell-Mann, and H. Leutwyler, Phys. Lett. **B47**, 365 (1973).

[2] D. J. Gross and F. Wilczek, Phys. Rev. Lett. **30**, 1343 (1973).

[3] D. J. Gross and F. Wilczek, Phys. Rev. **D8**, 3633 (1973).

[4] H. D. Politzer, Phys. Rev. Lett. **30**, 1346 (1973).

[5] S. L. Glashow, Nucl. Phys. **22**, 579 (1961).

[6] S. Weinberg, Phys. Rev. Lett. **19**, 1264 (1967).

[7] A. Salam, Originally printed in *Svartholm: Elementary Particle Theory, Proceedings Of The Nobel Symposium Held 1968 At Lerum, Sweden*, Stockholm 1968, 367-377.

[8] G. 't Hooft, Nucl. Phys. **B33**, 173 (1971).

[9] G. 't Hooft, Nucl. Phys. **B35**, 167 (1971).

[10] G. 't Hooft and M. J. G. Veltman, Nucl. Phys. **B44**, 189 (1972).

[11] P. W. Higgs, Phys. Lett. **12**, 132 (1964).

[12] P. W. Higgs, Phys. Rev. Lett. **13**, 508 (1964).

[13] P. W. Higgs, Phys. Rev. **145**, 1156 (1966).

[14] F. Englert and R. Brout, Phys. Rev. Lett. **13**, 321 (1964).

[15] G. S. Guralnik, C. R. Hagen, and T. W. B. Kibble, Phys. Rev. Lett. **13**, 585 (1964).

[16] A. Einstein, Annalen Phys. **49**, 769 (1916).

[17] O. Biebel, Phys. Rept. **340**, 165 (2001).

[18] S. Kluth, Rept. Prog. Phys. **69**, 1771 (2006), hep-ex/0603011.

[19] R. K. Ellis, W. J. Stirling, and B. R. Webber, Camb. Monogr. Part. Phys. Nucl. Phys. Cosmol. **8**, 1 (1996).

[20] JADE, S. Bethke *et al.*, Phys. Lett. **B213**, 235 (1988).

[21] N. Brown and W. J. Stirling, Phys. Lett. **B252**, 657 (1990).

[22] S. Catani, Y. L. Dokshitzer, M. Olsson, G. Turnock, and B. R. Webber, Phys. Lett. **B269**, 432 (1991).

[23] S. Bethke, Z. Kunszt, D. E. Soper, and W. J. Stirling, Nucl. Phys. **B370**, 310 (1992).

[24] S. Brandt, C. Peyrou, R. Sosnowski, and A. Wroblewski, Phys. Lett. **12**, 57 (1964).

[25] E. Farhi, Phys. Rev. Lett. **39**, 1587 (1977).

[26] L. Clavelli and D. Wyler, Phys. Lett. **B103**, 383 (1981).

[27] P. E. L. Rakow and B. R. Webber, Nucl. Phys. **B191**, 63 (1981).

[28] S. Catani, G. Turnock, and B. R. Webber, Phys. Lett. **B295**, 269 (1992).

[29] G. Parisi, Phys. Lett. **B74**, 65 (1978).

[30] J. F. Donoghue, F. E. Low, and S.-Y. Pi, Phys. Rev. **D20**, 2759 (1979).

[31] N. Brown and W. J. Stirling, Z. Phys. **C53**, 629 (1992).

[32] W. J. Stirling, J. Phys. **G17**, 1567 (1991).

[33] R. K. Ellis, D. A. Ross, and A. E. Terrano, Nucl. Phys. **B178**, 421 (1981).

[34] Z. Kunszt, Phys. Lett. **B99**, 429 (1981).

[35] J. A. M. Vermaseren, K. J. F. Gaemers, and S. J. Oldham, Nucl. Phys. **B187**, 301 (1981).

[36] K. Fabricius, I. Schmitt, G. Kramer, and G. Schierholz, Zeit. Phys. **C11**, 315 (1981).

[37] W. T. Giele and E. W. N. Glover, Phys. Rev. **D46**, 1980 (1992).

[38] S. Catani and M. H. Seymour, Phys. Lett. **B378**, 287 (1996), hep-ph/9602277.

[39] S. Catani, G. Turnock, B. R. Webber, and L. Trentadue, Phys. Lett. **B263**, 491 (1991).

[40] S. Catani, L. Trentadue, G. Turnock, and B. R. Webber, Nucl. Phys. **B407**, 3 (1993).

[41] G. P. Korchemsky and G. Sterman, Nucl. Phys. **B437**, 415 (1995), hep-ph/9411211.

[42] Y. L. Dokshitzer and B. R. Webber, Phys. Lett. **B352**, 451 (1995), hep-ph/9504219.

[43] Y. L. Dokshitzer and B. R. Webber, Phys. Lett. **B404**, 321 (1997), hep-ph/9704298.

[44] Y. L. Dokshitzer, A. Lucenti, G. Marchesini, and G. P. Salam, JHEP **05**, 003 (1998), hep-ph/9802381.

[45] A. Gehrmann-De Ridder, T. Gehrmann, E. W. N. Glover, and G. Heinrich, JHEP **12**, 094 (2007), 0711.4711.

[46] T. Becher and M. D. Schwartz, JHEP **07**, 034 (2008), 0803.0342.

[47] T. Gehrmann, G. Luisoni, and H. Stenzel, Phys. Lett. **B664**, 265 (2008), 0803.0695.

[48] T. Gehrmann, G. Luisoni, and H. Stenzel, (2008), 0810.3599.

[49] C. Anastasiou, K. Melnikov, and F. Petriello, Phys. Rev. Lett. **93**, 032002 (2004), hep-ph/0402280.

[50] A. Gehrmann-De Ridder, T. Gehrmann, and E. W. N. Glover, Nucl. Phys. **B691**, 195 (2004), hep-ph/0403057.

[51] S. Weinzierl, Phys. Rev. **D74**, 014020 (2006), hep-ph/0606008.

[52] A. Gehrmann-De Ridder, T. Gehrmann, E. W. N. Glover, and G. Heinrich, Phys. Rev. Lett. **100**, 172001 (2008), 0802.0813.

[53] Kunszt, Z. et al., in Altarelli, G., R. Kleiss, and C. Verzegnassi, p. 373, REPORT-NUM–CERN-89-08.

[54] A. Signer and L. J. Dixon, Phys. Rev. Lett. **78**, 811 (1997), hep-ph/9609460.

[55] L. J. Dixon and A. Signer, Phys. Rev. **D56**, 4031 (1997), hep-ph/9706285.

[56] Z. Nagy and Z. Trocsanyi, Phys. Rev. Lett. **79**, 3604 (1997), hep-ph/9707309.

[57] J. M. Campbell, M. A. Cullen, and E. W. N. Glover, Eur. Phys. J. **C9**, 245 (1999), hep-ph/9809429.

[58] S. Weinzierl and D. A. Kosower, Phys. Rev. **D60**, 054028 (1999), hep-ph/9901277.

[59] E. Maina, S. Moretti, and D. A. Ross, JHEP **04**, 056 (2003), hep-ph/0210015.

[60] C. M. Carloni-Calame, S. Moretti, F. Piccinini, and D. A. Ross, (2008), 0804.3771.

[61] ALEPH, R. Barate *et al.*, Phys. Rept. **294**, 1 (1998).

[62] T. Kinoshita, J. Math. Phys. **3**, 650 (1962).

[63] T. D. Lee and M. Nauenberg, Phys. Rev. **133**, B1549 (1964).

[64] F. Bloch and A. Nordsieck, Phys. Rev. **52**, 54 (1937).

[65] M. Böhm, H. Spiesberger, and W. Hollik, Fortsch. Phys. **34**, 687 (1986).

[66] T. Hahn, Comput. Phys. Commun. **140**, 418 (2001), hep-ph/0012260.

[67] T. Hahn and M. Perez-Victoria, Comput. Phys. Commun. **118**, 153 (1999), hep-ph/9807565.

[68] A. Denner, S. Dittmaier, M. Roth, and L. H. Wieders, Nucl. Phys. **B724**, 247 (2005), hep-ph/0505042.

[69] A. Denner, Fortschr. Phys. **41**, 307 (1993).

[70] A. Denner, S. Dittmaier, M. Roth, and M. M. Weber, Nucl. Phys. **B660**, 289 (2003), hep-ph/0302198.

[71] A. Denner, S. Dittmaier, M. Roth, and M. M. Weber, Nucl. Phys. **B680**, 85 (2004), hep-ph/0309274.

[72] A. Denner, S. Dittmaier, M. Roth, and L. H. Wieders, Phys. Lett. **B612**, 223 (2005), hep-ph/0502063.

[73] G. 't Hooft and M. J. G. Veltman, Nucl. Phys. **B153**, 365 (1979).

[74] W. Beenakker and A. Denner, Nucl. Phys. **B338**, 349 (1990).

[75] A. Denner, U. Nierste, and R. Scharf, Nucl. Phys. **B367**, 637 (1991).

[76] A. Denner and S. Dittmaier, Nucl. Phys. **B658**, 175 (2003), hep-ph/0212259.

[77] A. Denner and S. Dittmaier, Nucl. Phys. **B734**, 62 (2006), hep-ph/0509141.

[78] G. Passarino and M. J. G. Veltman, Nucl. Phys. **B160**, 151 (1979).

[79] A. Denner, S. Dittmaier, M. Roth, and D. Wackeroth, Nucl. Phys. **B560**, 33 (1999), hep-ph/9904472.

[80] H. Baer, J. Ohnemus, and J. F. Owens, Z. Phys. **C42**, 657 (1989).

[81] M. Böhm and S. Dittmaier, Nucl. Phys. **B409**, 3 (1993).

[82] S. Dittmaier and M. Böhm, Nucl. Phys. **B412**, 39 (1994).

[83] D. Wackeroth and W. Hollik, Phys. Rev. **D55**, 6788 (1997), hep-ph/9606398.

[84] U. Baur, S. Keller, and D. Wackeroth, Phys. Rev. **D59**, 013002 (1999), hep-ph/9807417.

[85] S. Catani and M. H. Seymour, Nucl. Phys. **B485**, 291 (1997), hep-ph/9605323.

[86] S. Dittmaier, Phys. Rev. **D59**, 016007 (1999), hep-ph/9805445.

[87] A. Denner, S. Dittmaier, M. Roth, and D. Wackeroth, Nucl. Phys. **B587**, 67 (2000), hep-ph/0006307.

[88] D. R. Yennie, S. C. Frautschi, and H. Suura, Ann. Phys. **13**, 379 (1961).

[89] G. 't Hooft and M. J. G. Veltman, Nucl. Phys. **B153**, 365 (1979).

[90] S. Dittmaier, Nucl. Phys. **B565**, 69 (2000), hep-ph/9904440.

[91] S. Dittmaier, A. Kabelschacht, and T. Kasprzik, Nucl. Phys. **B800**, 146 (2008), 0802.1405.

[92] E. W. N. Glover and A. G. Morgan, Z. Phys. **C62**, 311 (1994).

[93] K. Koller, T. F. Walsh, and P. M. Zerwas, Zeit. Phys. **C2**, 197 (1979).

[94] E. Poulsen, Diploma Thesis, University of Zurich (2006).

[95] W. Beenakker et al., in Altarelli, G., T. Sjostrand, and F. Zwirner, p. 79, REPORT-NUM–CERN-96-01.

[96] C. Meier, PhD Thesis, University of Zurich (2005).

[97] S. Weinzierl, (2000), hep-ph/0006269.

[98] F. A. Berends, P. H. Daverveldt, and R. Kleiss, Nucl. Phys. **B253**, 421 (1985).

[99] F. A. Berends, P. H. Daverveldt, and R. Kleiss, Nucl. Phys. **B253**, 441 (1985).

[100] J. Hilgart, R. Kleiss, and F. Le Diberder, Comput. Phys. Commun. **75**, 191 (1993).

[101] F. A. Berends, R. Pittau, and R. Kleiss, Nucl. Phys. **B424**, 308 (1994), hep-ph/9404313.

[102] F. A. Berends, R. Pittau, and R. Kleiss, Comput. Phys. Commun. **85**, 437 (1995), hep-ph/9409326.

[103] M. Roth, PhD Thesis, ETH Zurich (1999), hep-ph/0008033.

[104] A. Sirlin, Phys. Rev. **D22**, 971 (1980).

[105] W. J. Marciano and A. Sirlin, Phys. Rev. **D22**, 2695 (1980).

[106] A. Sirlin and W. J. Marciano, Nucl. Phys. **B189**, 442 (1981).

[107] Ciccolini, M. L. and Dittmaier, S. and Krämer, M., Phys. Rev. **D68**, 073003 (2003), hep-ph/0306234.

[108] Particle Data Group, C. Amsler *et al.*, Phys. Lett. **B667**, 1 (2008).

[109] D. Y. Bardin, A. Leike, T. Riemann, and M. Sachwitz, Phys. Lett. **B206**, 539 (1988).

[110] D. Y. Bardin et al., in Altarelli, G., R. Kleiss, and C. Verzegnassi, p. 89, REPORT-NUM–CERN-89-08.

[111] A. Gehrmann-De Ridder, T. Gehrmann, E. W. N. Glover, and G. Heinrich, JHEP **11**, 058 (2007), 0710.0346.

[112] S. Weinzierl, Phys. Rev. Lett. **101**, 162001 (2008), 0807.3241.

[113] S. Weinzierl, (2009), 0904.1145.

[114] Z. Nagy and Z. Trocsanyi, Phys. Rev. **D59**, 014020 (1999), hep-ph/9806317.

[115] G. Dissertori, I. G. Knowles, and M. Schmelling, Oxford, UK: Clarendon (2003) 538 p.

[116] G. Luisoni, Diploma Thesis, ETH Zurich (2006).

Acknowledgements

First of all I want to thank Ansgar Denner and Thomas Gehrmann for assigning the topic of this thesis. They always made time for my questions, came up with sensible answers, and continuously supported me throughout the project. I also want to thank Stefan Dittmaier for the productive collaboration and for bearing with me on the rocky path to finding agreement of the virtual corrections.
Special thanks go to Ben Moore for providing billiards, ping-pong, fooseball, and most importantly the annual 'cheese fondue and kegeln'.
I also would like to express my gratitude to Doug Potter and Roland Bernet for the excellent computing infrastructure they provided.
I am grateful to all my colleagues at the Institute for Theoretical Physics and the Theory Group at PSI for creating a very pleasant working environment. I especially want to thank my office mates David, Lucia, and Tobias (in order of appearance) for providing much appreciated distraction and for keeping me company on the long train rides to and from PSI. I am much obliged to Cedric, Nurhana, and Tobias for proof-reading the manuscript. I also want to express my gratitude to Joachim Stadel for motivating me to engage in Long Jogs which most of the time ended with me only being barely able to make it back to Irchel.
I would like to thank Katrin Völter, who must have wondered what I was doing at 3 am in the living room hunched over my laptop, for sharing a flat with me.
I am indebted to my parents Maritta and Klaus Kurz, my sister Anette, my brother-in-law Andreas, and my niece Charlotte, for, sometimes hesitantly, backing me up during all my university adventures.
Finally, I want to thank Nurhana for encouraging me, for being patient with me, and for loving me back.